Università degli Studi di Trieste

XXIV CICLO DEL DOTTORATO DI RICERCA IN NANOTECNOLOGIE

Self-assembling and charge transfer properties of thin organic films

Settore scientifico-disciplinare: fis03-Fisica della Materia

DOTTORANDA
VALERIA LANZILOTTO

COORDINATORE
PROF. MAURIZIO FERMEGLIA

RELATORE
PROF. ALBERTO MORGANTE

ANNO ACCADEMICO 2010-2011

Abstract

In the present thesis I dealt the issue of molecular ordering and charge transfer at two types of organic-inorganic interfaces that are representative of the basic constituents of an organic electron device. I investigated *i.* the influence of a selected dielectric surface on the ordering of an overlayer of several organic molecules and *ii.* the electronic transport properties of a single molecular junction with a metal electrode.

Both systems have been characterized by a structural and electronic point of view. Among the techniques available for structural investigation, I made extensive use of Helium Atom Scattering (HAS) and Scanning Tunneling Microscopy (STM). The electronic properties, with particular emphasis to the charge transfer, have been addressed by two methods chosen according to the dimensionality of the system under consideration. For the charge transfer at laterally extended interfaces I used synchrotron based techniques, like Resonant Photoemission Spectroscopy (RPES), while for the charge transport through a single molecule I used and developed the STM-based break junction technique (STM-BJ).

For the first type of interface, I focused on the coupling between the TiO_2(110)-1×1 surface and different organic semiconductor molecules: C_{60}, pentacene, perylene-tetracarboxilic-acid-diimide (PTCDI) and perylene. The strong anisotropy of the substrate has been found to drive the adsorption geometry of the molecules leading to the formation of ordered phases (at least for the first layer). In particular pentacene, PTCDI and perylene (polycyclic aromatic hydrocarbons, PAHs) display a common self-assembly mechanism, where the molecules lay on the surface with their long axis oriented parallel to the [001] substrate direction. In the transverse direction $[1\bar{1}0]$ these molecules are observed to match the substrate periodicity by tilting the

molecular plane around the long axis by an angle that depends on the molecular width. Nevertheless the molecule-to-substrate interaction is very weak as indicated by the molecular electronic structure, which is observed by x-ray spectroscopy to remain mostly unperturbed in the first molecular layer. Only PTCDI bears a major interaction with the TiO_2(110)-1×1 surface, but confined to the molecular orbitals closest to the gap. The main experimental evidence of this interaction is the appearance of a new molecular filled state in the valence band region close to the Fermi level. By a combined RPES and NEXAFS study we have found that this new electronic state is due to the charge transfer occurring from the substrate Ti defect state (i.e. the excess of electrons associated with oxygen vacancies) to the lowest unoccupied molecular orbital (LUMO).

For the second type of hybrid interface, instead, I exploited the nitrogen-link chemistry in order to bridge a phthalocyanine to two gold electrodes and to measure its conductance. In particular, by using the Tetraaza-Cu-Phthalocyanine I investigated the pyridine-gold bond that is relatively weak and insensitive to the local structure, a fundamental requirement for the establishment of well defined and stable transport properties. The weak interaction between the molecule and a representative metal electrode, namely the Au(100) surface, has been confirmed by spectroscopic and STM experiments. At RT the molecules have been found to diffuse on the surface and only at LT (55 K) they can be observed to self-organize into large molecular domains. On these domains, reliable and reproducible single molecule conductance measurements have been performed by using the STM-based break junction method. The conductance value obtained for the Tetraaza-Cu-Phthalocyanine (7×10^{-4} G_0) has been rationalized in terms of the molecular length and degree of conjugation, as well as by correlation to the energy level alignment at the junction.

Contents

1

Introduction

Organic electronics is an emerging technology, which relies on the possibility to adopt organic material composed by polymers or small molecules as the active part of electronic devices. It is well established that in the next years, organic-based technology will play a crucial role in the development of devices in many fields, ranging from biology to electronics, from nanomedicine to coating technology. The global market for the organic devices is supposed to reach the considerable value of 300 billion $ in 2027 (1). The OLEDs (Organic Light Emitting Diodes), the photovoltaic cells and the logic-memory devices will represent the major part of the business. Indeed, some organic-based devices have already been commercialized (displays for cell phones, monitors and photovoltaic cells) and others are going to be available in the very next future (lighting OLEDs). These perspectives are even more intriguing when we consider that the applications we have mentioned, which adopt thin organic films as active part, are just the first step of the organic electronics revolution. In fact, one of the hottest topics of the material science studies in the last years, is the possibility to exploit a single organic molecule as active element of an electronic device (2). The success of the organic-based technology is based on few important aspects characterizing the organic molecules and their exploitation in the designing of the devices:

i. Size. The size scale of molecules is between 1 and 100 nm, a scale that permits functional nanostructures with accompanying advantages in cost, efficiency, and power dissipation.

ii. Self-Assembly and recognition. One can exploit specific intermolecular interactions to form structures by nanoscale self-assembly. Molecular recognition can be used to modify electronic behavior, providing both switching and sensing capabilities on the single-molecule scale.

iii. Dynamical stereochemistry. Many molecules have multiple distinct stable geometric structures or isomers. Such geometric isomers can have distinct optical and electronic properties.

iv. Synthetic tailorability. Choosing the molecular composition and geometry, one can extensively vary the transport, binding, optical, and structural properties, thanks to the highly advanced molecular synthesis tools presently available.

Nevertheless, the current performances and the reliability of the organic thin film technology still do not justify the market projections. Despite the several advantages (low density, flexibility, high tunability of the optical properties) and its low-cost scalability processes (spin-coating, jet-printing), both the efficiency and the durability are considerably lower in the organic devices than in the inorganic-based ones. In most cases the bottleneck for the device performance is the charge transport between the active part (organic semiconductor) and the electrodes (3). The proliferation of defects at the organo-metallic interface, due to the strong interaction between the molecules and the substrate, often prevents the formation of reliable contacts. Moreover, the absorption geometry of the molecules in contact with the substrate differs from that in the molecular crystal, leading to a inhomogeneous morphology of the film. This aspect limits the performance of such architectures, since it has been demonstrated that the structure and the morphology of the films strongly affect their transport properties, being the charge mobility strongly (anti-) correlated with the degree of disorder of the system (4).

Within this framework, the ability to control the electronic properties of the organo-electrode interface plays a fundamental role for the ultimate success of the organic-based technology. It becomes mandatory to define an investigation protocol, which permits to describe all the relevant aspects of the junctions: morphology, chemistry, charge transfer, charge transport.

In this thesis work, we address two fundamental issues of an hybrid device:

i. the influence of a selected dielectric substrate on the ordering of an overlayer of several semiconductor organic molecules: fullerene and polycyclic aromatic hydrocarbons on TiO_2.

ii. the electronic transport properties of a single molecular junction:

the Au-Phthalocyanine-Au junction.

For the first class of systems, the attention has been focused on the study of the morphology and structure of the interfaces, as well as on the charge transfer between molecules and the substrate, in view of a possible dual use (electrode/dielectric) of the supporting TiO_2 material. In the case of the Au-molecule-Au junction instead, the correlation between the electronic transport at the junction and the electronic levels at the organo-metallic interface has been investigated. Both classes of systems have been characterized from a structural and electronic point of view; a multiple experimental techniques approach has been used ranging from synchrotron to tunneling microscopy based methods. Among the techniques available for structural investigation I made extensively use of Helium Atom Scattering (HAS) and Scanning Tunneling Microscopy (STM). The electronic properties, with particular interest for the charge transfer, have been addressed by using two methods. In the case of semiconductor molecules on the TiO_2 surface I used Synchrotron-based techniques like Near Edge X-ray Absorption Spectroscopy (NEXAFS) and Resonant Photoemission Spectroscopy (RPES) whereas for the Au-molecule-Au junction I used and developed the STM-based Break-Junction technique (STM-BJ). The experimental methods and apparatus will be described in chapter 2. Chapter 3 will be dedicated to the results obtained using the $TiO_2(110)$ surface as a template in the thin films growth. After a first illustration of the surface the single systems will be presented in different sections. In Chapter 4 the reader will find the description of the STM-based Break-Junction technique and the study of N-terminated molecules on gold. Finally in chapter 5 I will summarize the findings of the present thesis.

2

Experimental techniques and apparatus

2.1 Scanning Tunneling Microscopy

The development of the scanning tunneling microscope (STM), ascribed to Binnig et al. (5) (6), has provided an atomically resolved microscopic view of clean and adsorbate covered metal and/or semiconductor surfaces. The experimental technique which has been described in numerous publications (7) is conceptually simple: a sharp metal tip is brought into close proximity (typically 1 nm) of a sample surface. If a voltage V is applied between the tip and an electrically conducting sample (the so-called sample bias voltage) a tunneling current I_t is generated which may be used for regulating the sample–to–tip distance to a constant value. In classical physics a particle can never be in a region where its potential energy is greater than its total energy. To do so it would require a negative kinetic energy, which is impossible because of $mv^2/2 \geq 0$. As the scale shrinks to atomic dimensions, classical concepts fail and the correct description is provided by quantum mechanics. Thus, it is possible for a particle to move from one classically allowed region to another through a region where its potential energy is greater than its total energy: this is the phenomenon of tunneling. Under the conditions of a constant tunneling current the sample is scanned and an image may be constructed which contains both information on the structural and local electronic properties of the surface. In order to show the principle and the capability of the STM let's introduce some basic concept.

Tunneling through a potential barrier had already been treated before the development of STM, e.g., to explain field emission (8) or characteristics of electrical current through a metal-insulator-metal (MIM) structure (9). The measured quantity in most cases is the local tunneling current I which, at the chosen sample bias voltage V, is regulated to a constant value by the feed-back circuit. What apparently is needed for the description of phenomenon is an expression for the spatially varying tunneling current between the tip and the sample surface. Following the work of Bardeen (10) on the tunneling current through a MIM structure, Tersoff and Hamann (11) have given an expression for the tunneling current I in the form of

$$I = \frac{2\pi e}{\hbar} \sum_{\mu}^{\nu} f(E_\mu)[1 - f(E_\nu + eV)]|M_{\mu\nu}|^2 \delta(E_\mu - E_\nu) \tag{2.1}$$

where $f(E)$ is the Fermi function, $M_{\mu\nu}$ the tunneling matrix element between states ψ_μ of the metal probe tip and ψ_ν of the sample surface, E_μ and E_ν the unperturbed states in the absence of tunneling and V the sample bias voltage. The contribution of reverse tunneling has been neglected here. The tunneling matrix element $M_{\mu\nu}$ may be computed by using the quantum mechanical expression for the current between states ψ_μ and ψ_ν independent on the height and form of the potential barrier between sample and tip. For modeling the tunneling tip by a point probe, small sample bias voltage and low temperature, the equation for the local tunneling current may be reduced to

$$I \propto \sum_{\nu} |\psi(\vec{r_0})|^2 \delta(E_\nu - E_F) \tag{2.2}$$

This expression corresponds to the charge density of states at the Fermi level E_F at the position $\vec{r_0}$ of the point probe.

To some extent this model can be applied to the electron tunneling between two metal electrodes (in this case the sample and the tip) through a vacuum barrier. As argued before the electrons can tunnel the potential barrier in the vacuum region if on the other side there are empty states to be filled. As long as both the tip and the sample are held at the same electrical potential, their Fermi levels line up exactly. There are no empty states on either side available for tunneling into. If the sample is biased by a negative voltage $-V$ with respect to the tip, this effectively raises the energy level of the sample electrons with respect to the tip electrons by an energy eV. Electrons will tend to tunnel out of the filled states of the sample into the empty states of the

tip. The total tunneling current will be proportional to the number of filled states (on the sample) available for tunneling from, times the number of empty states (on the tip) available for tunneling to. In other words, the tunneling current is proportional to the integral of the density of states of both sample and tip, in the energy range $0 < \varepsilon < -eV$.

By solving the stationary Schrödinger equation for the motion of an electron across an ideal square barrier,

$$\mathscr{H}\Psi = \left(\frac{\hbar^2}{2m_e} - U\right)\Psi = E\Psi \tag{2.3}$$

the expression for the probability of finding the particle of mass m_e and energy E behind the energy barrier U of width d is:

$$|\Psi_{Z>d}|^2 = \left|\Psi_{(Z=0)}\right|^2 e^{-2kd} \tag{2.4}$$

where

$$k = \frac{\sqrt{2m_e(U-E)}}{\hbar} \tag{2.5}$$

In this way we can see that the larger the distance, the lower the probability of tunneling.

The assumption that the vacuum barrier is square is the so called WKB approximation. This approximation is still valid in the case of a real barrier, since the tilt due to the applied voltage ($\sim 100meV$) is small compared to the height of the barrier which is as high as the energy required to remove an electron from a metal, i.e. the work function, typically of several eV. Taking into account the aforementioned considerations, the expression for the tunneling current can be written as an exponential decay of the type:

$$I \propto e^{-2\frac{\sqrt{2m_e\Phi}}{\hbar}d} \tag{2.6}$$

where Φ is the real height of the barrier, which is actually a balance of the work functions of the tip and sample. Since most work function are around 4-5 eV, we find that tipically $2\frac{\sqrt{2m_e\Phi}}{\hbar} \approx 2\text{Å}^{-1}$. Thus the tunneling current drops by nearly an order of magnitude for every 1 Åvacuum between the electrodes. This exponential dependence

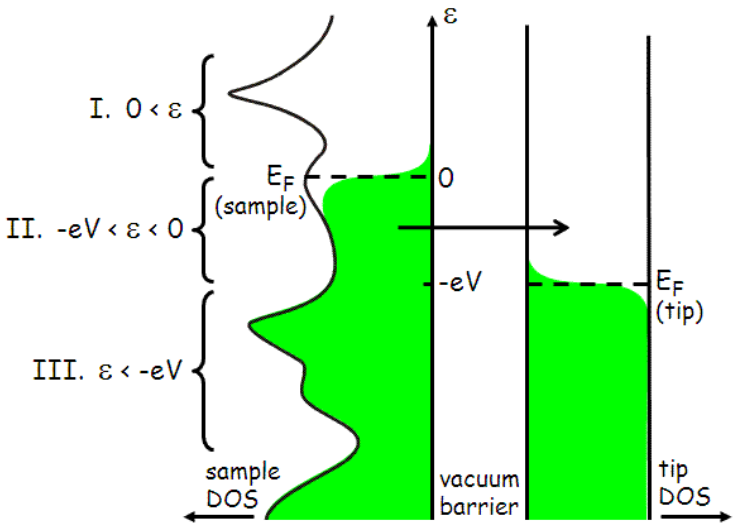

Figure 2.1: Schematic of tip-sample tunneling. Energy is along the vertical axis, and density of states of the sample and tip are shown along the horizontal axes. Filled states are shown in green. In this case, a negative bias voltage $-V$ has been applied to the sample, which effectively raises its Fermi level by eV with respect to the Fermi level of the tip. This allows for filled states on the left (sample) to tunnel into empty states on the right (tip). The tunneling current is measured by an external circuit.

of tunneling current on electrode separation is essential for the STM, and the main reason for its high spatial resolution.

In an STM the tip (or the sample) is mounted on a piezoelectric support and scanned in the two lateral dimensions while a feedback circuit constantly adjusts the tip height, to keep the current constant (constant current mode). This yields a constant tip height, so the surface topography is reproduced by the vertical excursion z of the tip scanning the horizontal plane xy, movements which can be inferred directly from the voltages supplied to the piezoelectric driver. The interpretation of STM images is not so straightforward as not only the topography is influencing the tip height but we have a very important contribution of the local density of states (LDOS) of the sample (see equation 2.2). This means that STM images are always a convolution of the surface topography and the sample LDOS. For simple metals, there is typically no strong variation of the local density of states and the images reflect in good approximation the topography of surface. This is not the case of semiconductors, like TiO_2, where a strong variation of the local density of states can lead to misunderstandings on the topographic features. In this case voltage-dependent imaging is essential for the meaningful interpretation of STM images on the atomic scale.

2.2 Helium Atom Scattering

The technique of helium atom scattering (HAS) provides substantial insight into surface phenomenology. The advantages of helium as a probe particle are its combination of low energy with short wavelength, its inert and neutral character and its relatively large cross-section. Owing to its mass, the de Broglie wavelength is comparable to typical crystallographic dimensions at an energy comparable to typical surface phonon energies. Thus, both surface structure and dynamic surface processes are simultaneously accessible to an atomic helium probe. Furthermore, the probe energy is typically between 10 and 100 meV, so is several orders of magnitude less than the energy of photons or electrons at comparable wavelengths. As a consequence, HAS is uniquely non-destructive and avoids the thermal or electronic excitation in samples that is inherent to study by electrons or x-rays. Finally, thermal helium atoms have a cross-section orders of magnitude larger than that of neutrons, electrons or photons. Penetration of the sample is avoided and HAS is therefore exclusively and unambiguously surface sensitive.

An impinging helium atom scatters almost entirely elastically from a sample's surface, without multiple scattering. Consequently, HAS is ideal for in-situ, non-invasive studies of delicate adsorbate structures and dynamic surface processes such as thin film growth. In this section, a brief overview of HAS as an experimental technique is given. More detailed descriptions can be found in several review articles (12) (13).

Nature of the helium scattering centers. The use of neutral-particle diffraction (elastic scattering) for surface structural investigations requires an understanding of the basic physical principles governing the interaction of the incoming particles with the solid surfaces. We restrict our discussion to cases in which the particles and the solid do not interact chemically. Typical interaction energies are therefore in the physisorption energies, i.e. several tens of meV. Consider a particle with coordinate $\mathbf{r} = (\mathbf{R}, z)$ outside a single crystal. The surface normal is chosen in the direction of z, so that $\mathbf{R}$ lies in the plane of the surface. At distances not too far from the surface, the He atoms feel an attraction due to the Van der Waals' forces. Closer to the surface, the particles are repelled owing to the overlap of their electronic densities with that of the surface. This causes a steeply rising repulsive part of the potential. A sketch of the one-dimensional interaction potential between an impinging helium atom and a sample's surface is given at the bottom right of Fig. 2.2 . In general, the classical turning points are farther away for particles impinging on top of the surface atoms than for particles impinging between them; this gives rise to a periodic modulation of the repulsive part of the potential. The locus of the classical turning points follows a surface of constant total electron density where every point constitutes a scattering centre; the resulting scattering surface is called the corrugation function $\zeta(\mathbf{R})$. As shown by Esbjerg and Nrskov (14), $\zeta(\mathbf{R})$ corresponds in first order to a contour of constant surface electronic charge density $\rho(\mathbf{r})$ related linearly to the particle energy $E(\mathbf{r})$. It implies that the He atoms are unable to penetrate into the crystals and are reflected at relatively large distances, the order of $2-3$ Å, from the surface plane. This is not the case in the electron scattering. Here scattering processes occur from the ion cores of the first 3-5 atomic layers with high probability of multiple scattering. These differences are illustrated in a schematic way in Fig. 2.2. Consequently, HAS information is complementary to that obtained in Low Energy Electron Diffraction (LEED) experiments.

Surface diffraction kinematics. In the experiments presented in the following chapters we are interested only in determining whether the molecules are adsorbed on the

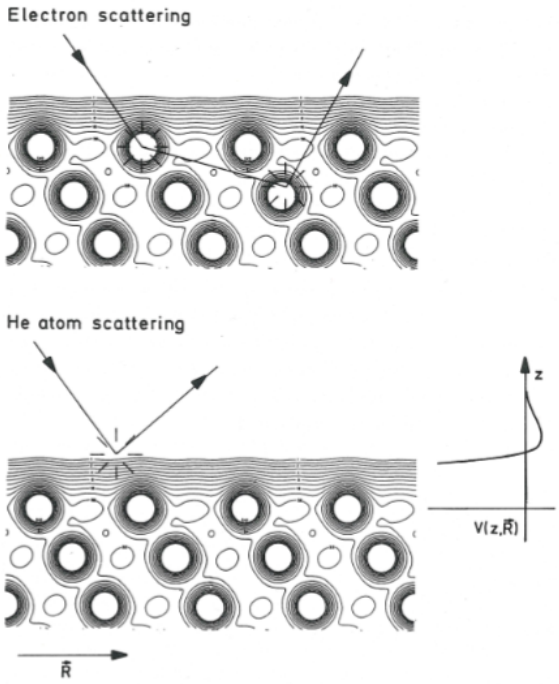

Figure 2.2: Schematic diagram showing the different nature of the interaction of electrons and He atoms with a crystal surface. A schematic form of the He-surface interaction potential is indicated at the bottom right.

surface and whether their assemblies present long range order. This can be done by monitoring the modifications in the diffraction pattern of the clean surface during or after deposition.

By making use of the kinematic theory of diffraction is it possible to determine the dimensions of the unit cell of the periodic structure on the surface as well as its orientation relative to the incoming beam. The well-know Bragg condition for diffraction from a two-dimensional periodic array relates the incoming wavevector $\mathbf{k}_i = (\mathbf{K}_i, \mathbf{K}_{iz})$ with the outgoing $\mathbf{k}_G = (\mathbf{K}_G, \mathbf{K}_{Gz})$ via

$$\mathbf{K}_i - \mathbf{K}_G = \mathbf{G} \tag{2.7}$$

where $\mathbf{G} = j\mathbf{b}_1 + l\mathbf{b}_2$ denotes a reciprocal lattice vector and $\mathbf{b}_1$ and $\mathbf{b}_2$ are related to the unit cell vectors $\mathbf{a}_1$ and $\mathbf{a}_2$ through $\mathbf{a}_p \cdot \mathbf{b}_q = 2\pi\delta_{pq}$, $p, q = 1, 2$. The wavelenght remains unchanged during diffraction, so that $\mathbf{k_i}^2 = \mathbf{k_G}^2$ (elastic scattering). The Bragg condition can be represented graphically by the Ewald construction shown schematically for a one dimensional case in Fig. 2.3. Surface diffraction can occur in all directions, where the Ewald sphere cuts a reciprocal-lattice rod (notice the difference from the three dimensional case, where diffraction does not necessarily occur as the Bragg condition is more stringent in this case: it requires the Ewald sphere to go through a reciprocal-lattice point)

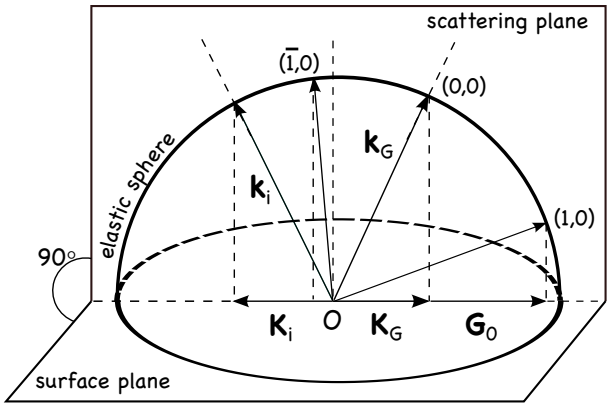

Figure 2.3: The Ewald construction for surface diffraction.

Growth of thin films. A further use of HAS is in the observation of thin film growth. Monitoring the specular reflectivity ($\mathbf{K_i} - \mathbf{K_G} = 0$) during thin-film deposition is often

sufficient to distinguish the growth mode. Schematic HAS deposition curves for the four main growth modes are presented in Fig: 2.4. During perfect layer by layer growth the surface defect density starts at a low value, increases with the number of ad-atoms and then decreases again as the layer is completed and the smooth mirror appearance is regained. Correspondingly, a HAS evaporation curve exhibits oscillations, with one cycle per monolayer, as indicated in Fig. 2.4(b). In contrast, three-dimensional growth results in a gradual surface roughening as the number of crystallites increases, so Volmer-Weber growth is characterized by a monotonic decrease in specular intensity, as illustrated in Fig. 2.4(d). Intermediate to these two regimes is Stranski-Krastanov growth, which proceeds by an initial oscillation after completion of the first monolayer, followed by an exponential decrease due to the onset of three-dimensional growth (Fig. 2.4(c)). A final growth mode, termed "step flow" is also possible and results in a layer by layer growth mechanism where all impinging atoms are incorporated at surface step edges, producing continuous motion of steps across the surface (Fig. 2.4(a)). If the net step length does not change with time, then the specular intensity is constant and no features are observed in the HAS evaporation curve. Thus, the growth mechanism is particularly easy to characterize using HAS.

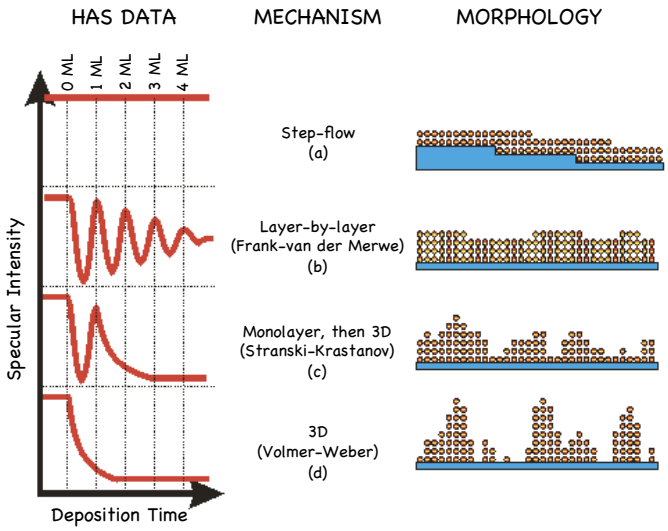

Figure 2.4: Schematic HAS measurements of specular reflectivity during the growth of a thin organic film.

2.3 Spectroscopic techniques

The discovery of the photoelectric effect by Hertz (1887), and later rationalized by Einstein (1905), led over the years to the development of a variety of photoelectron spectroscopic techniques. Today, many of these techniques are used to provide important information on the electronic properties of organic materials, which form the basis of the rapidly growing field of organic electronics. 'Conventional' x-ray (XPS) and ultraviolet (UPS) photoemission spectroscopy (PES) probe occupied electronic states through direct photoionization (15). Near-edge x-ray absorption fine structure (NEXAFS) studies provide information on unoccupied states in the presence of the core hole (16). Core-excited states have a relatively short lifetime (on the fs scale) and decay by either radiative x-ray emission or non-radiative Auger-like electron emission. The non-radiative decay that goes by the general name of Resonant Photoemission (RPES) is also recognized as a useful tool to probing the occupied electronic structure (17). A sketch of these electron spectroscopies will be presented in the next sections with particular attention for RPES and NEXAFS. Another section will be dedicated to Photoelectron Diffraction (PED) a powerful technique for surface structural investigations(18).

2.3.1 Photoemission and Resonant Photoemission Spectroscopy

Fig. 2.5 shows a schematic of different electronic excitation and de-exicitation channels of interest here, with and without resonant excitation. Fig. 2.5(a) depicts excitation of a valence electron in standard valence-band photoelectron spectroscopy (UPS), creating a vacancy and a +1 charge state on a isolated system such as a molecule. Fig. 2.5(b) shows a similar excitation of a core electron to an unbound final state (XPS). After such excitation, a vast majority of the decay processes annihilating the core hole will be as shown in Fig. 2.5(c), Auger transitions leaving the system in a +2 charge state. Via the Coulomb interaction, one electron makes a transition to fill the core hole, and a second electron, which takes up the excess energy, is ejected. This produces a double vacancy in the valence bands, as illustrated. The remaining small percentage of the primary decay processes will consist of radiative transitions or soft-x-ray emission.

On the other hand, if a core electron is photo-excited to a resonant bound state (NEXAFS) the system remains charge neutral until de-excitation Fig. 2.5(d), and again Auger-like transitions will dominate for the core levels under consideration here. As

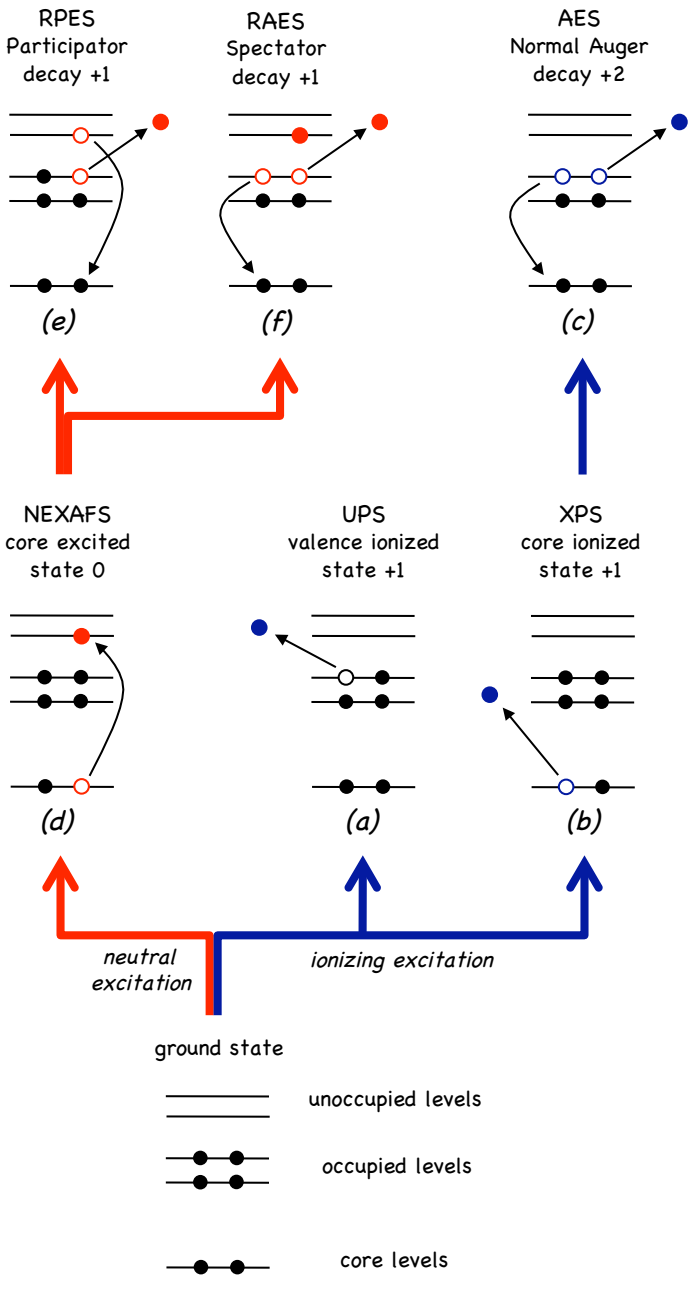

Figure 2.5: Schematic representation of electronic excitations and decay processes. The final states probed in various spectroscopic techniques are denoted by the corresponding acronym.

shown in Figs. 2.5(e) and (f), this leads to two new possibilities for the electron spectra. One channel is characterized by the involvement of the excited electron in the Auger process [Fig. 2.5(e)], thus taking its name as the participant channel, which leaves the system with a single valence vacancy and a charge of +1. This final state is energetically the equivalent of valence PES, but the core-hole-assisted path generally has a much larger cross section for the core levels of interest here. This channel is often given the name resonant PES (RPES) or participant auto-ionization spectroscopy. A second possibility is also shown, Fig. 2.5(f), in which an electron remains in the normally unoccupied levels in the final state, and two valence electrons have been removed in an Auger-like transition. This channel, often called resonant Auger or spectator auto-ionization, also leaves the system in a +1 charge state. The kinetic spectrum of the electrons emitted in this latter process is similar to the Auger spectrum of the same system, but with all lines uniformly shifted to higher kinetic energies. This "spectator shift" is caused by the screening action of the excited electron on the two holes which eases their creation, so that the kinetic energies of the emitted decay electrons shift to higher values (by a constant value for all lines).

A comparison of these process is given in Fig. 2.6 using data of solid C60. This many-atom system shows a great similarity between Auger and spectator auto-ionization except for the shift, which has been discussed above. Also seen is the weak relative cross section for participant compared to spectator auto-ionization. This figure also hints at a fundamental limitation on the usefulness of dividing the spectrum into participant and spectator contributions, since for larger systems these often overlap. For example, in the case of C60, only the band derived from the highest occupied molecular orbital (HOMO) at 282.5 eV has unbeatably pure participant origin, whereas the band below may contain slight contributions from other transitions, and the next band at 279 eV is degenerate with a noticeable background of spectator contributions.

It is worthwhile to note here that in the case of molecules adsorbed on solid substrates the electronic emission from the highest occupied molecular orbitals is often superimposed on the valence band photoemission from the solid substrate which makes the determination of the electronic structure of the adsorbate/substrate system quite a difficult task. Due to the resonant nature of electron emission process near the X-ray absorption edge, RPES may detect spectral features in the valence band spectra

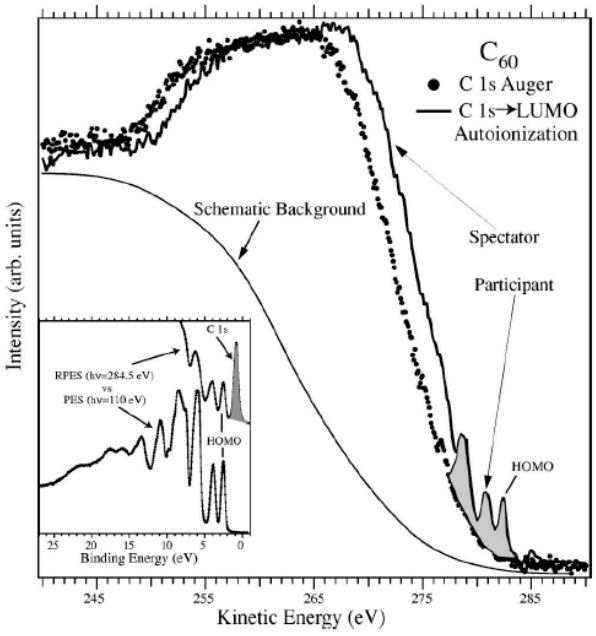

Figure 2.6: Data for solid C60 corresponding to cases of Fig. 2.5: points, case (c); solid lines, cases (e) and (f).

which are otherwise extremely difficult to resolve in a conventional X-ray photoemission experiment.

There is a final point that should be underlined: for a participator decay the spatial overlap among the involved wave-functions (ψ_{core}, ψ_{LUMO}, ψ_{HOMO}) is required, which makes the process intrinsically suitable for probing their spatial distribution. In fact, the occurrence of resonating spectral features in the VB spectrum in correlation with NEXAFS absorption peaks (core-LUMO transitions) proves that the filled state wave-function (ψ_{HOMO}) is spatially located close to the core site and so must be also the ψ_{LUMO}. This way RPES enables a direct chemical identification of the VB emission site. In other words, across the absorption resonance it is possible to assign various valence band peaks to the different chemical species that compose the material and also in certain cases to nonequivalent sites of the same chemical element in the molecule if enough energy resolution is provided by the experimental apparatus.

Another interesting research topic that can be investigated with resonant photoemission is the occurrence of fast charge transfer at the molecule-substrate interface (19) (20). If the transiently occupied molecular orbital is delocalized over many atomic

centers, i.e., strongly coupled to the substrate, a transfer of the excited electron to the substrate competes with the decay process that takes place during the core-hole lifetime. The core-hole then decays via the normal Auger channel (see Fig. 2.7) and the resonant peak intensity results quenched.

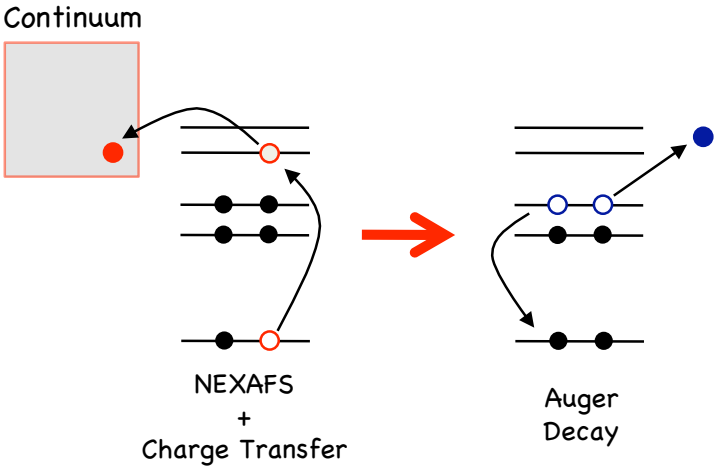

Figure 2.7: Schematic of the pathway for de-excitation of a system that is coupled to a (substrate) continuum. After excitation via NEXAFS the excited electron may tunnel into the continuum, opening an Auger channel.

2.3.2 Near Edge X-ray Absorption Fine Structure Spectroscopy

In NEXAFS, Near-Edge X-ray Absorption Fine Structure, we measure the X-ray absorption near the excitation edge of a certain atomic shell. The electron from a localized inner shell is excited to one of the unfilled molecular states, followed by the de-excitation through emission of a fluorescent photon or an Auger electron. When exciting the atoms core shells, Auger emission is amongst most probable processes. In this two-stage process, an electron from higher orbitals gets ejected by taking over the energy of the electron which relaxes to the core level, as displayed in Fig. 2.5(d, e, f).

By selecting a specific atomic species throught its ionization edge NEXAFS probes its bonds to intra-molecular and, even if less clearly, extra-molecular (i.e. surface atoms) neighbours. In particular by means of this technique it is possible to:

i. Detect the presence of specific bonds in molecules.

ii. Determine the bond lengths.

iii. Determine the molecules orientation with respect to the surface.

iv. Reveal which orbitals are involved in the bond with the substrate.

In general, an electron photo-emitted by an atom or a molecule encounters empty atomic or molecular states before the continuum states above the vacuum level. For a closed shell atom in its ground state Schrödinger equation predicts empty Rydberg states below the vacuum level E_v. The same situation is found for the core exited atom, with just an energy shift of the electronic states.

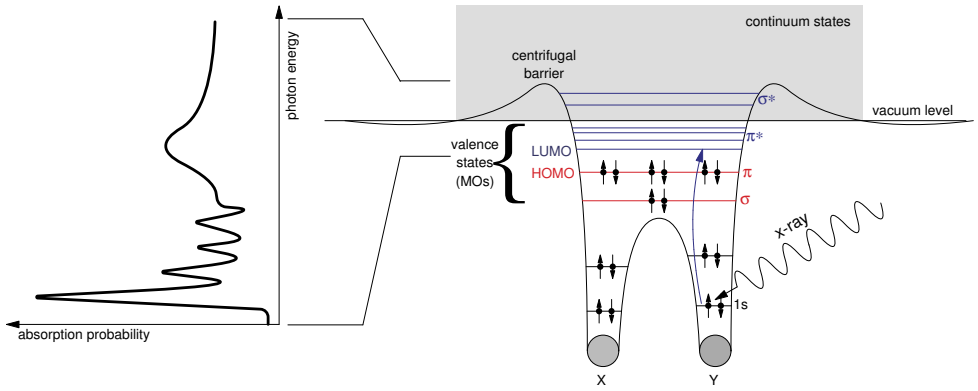

Figure 2.8: Schemes of the potential (right) and expected $K-$shell spectra (left) of diatomic molecules.

For the diatomic molecules there are in addiction unfilled or empty molecular orbitals. Usually MOs are labelled in terms of σ or π symmetry and unfilled MOs are denoted with an asterisk. As illustrated in Fig.2.8 the lowest unoccupied MO (LUMO) is usually a π^* orbital with a σ^* orbital at higher energy. These states are typically above the vacuum level for neutral molecules but the π^* state is pulled below E_v by electron-hole interaction in the ionized molecule. The σ^* remain above the vacuum level and no resonances in the absorption spectra due to this state would be therefore expected. In fact, as depicted in the top part of the figure, a broad σ^* resonance is present. This is indicated in literature as σ^* *shape resonance* and arise from the fact that the potential for the photo-emitted electron include a centrifugal term which depends on the angular momentum of the electron and gives rise to the potential barrier;

in this way the σ^* state becomes a real MO and the probability that an electron emitted from a core level is entrapped in this state is increased. A molecule absorption spectrum is in fact more complicated than that depicted in the figure, which directly reproduces the distribution of MOs. Here the multi-electron excitations are neglected and therefore some possible further features are missing in the spectrum. It has been assumed in this scheme that all the transitions from the core $1s$ level to unoccupied states are allowed. This is not true in general since some symmetry considerations have to be taken in account.
The intensity in an absorption spectrum is proportional to the probability that an electron that is in its initial state $< i|$ occupies an higher energy final state $|f >$ when a photon beam illuminates the material. This transition probability is described by the Fermi's Golden Rule and can be written as:

$$P \propto < i|\vec{e} \cdot \vec{p}|f > \tag{2.8}$$

where $\vec{e}$ is the electric field direction and $\vec{p}$ is the momentum operator. It can be easily shown that for a linearly polarized field and a $1s$ initial state the 2.8 gives a maximum when $\vec{e}$ is aligned along a direction of maximum electron density for the final state $|f >$. Strictly speaking, if we have a molecule with a certain orientation, we fix the photon energy in correspondence of one of the resonances of the absorption spectrum and rotate the polarization vector of the incident beam, we have a maximum in intensity when the polarization is in the direction or in the plane of spatial elongation of the MO we are populating. If we know from calculations the shape of the selected MO we are therefore able to understand how the molecule is oriented. This is the typical measurement that can be performed on an ordered molecular film in order to investigate the molecules orientation with respect to the substrate.

2.3.3 Photoelectron Diffraction

X-ray photoelectron diffraction is a very powerful technique for the determination of surface structures at the atomic scale. This technique is based on the fact that photoelectrons may suffer elastic scattering processes during their way out of the crystal, being possible to observe diffraction patterns due to the interference between the direct and scattered waves. It presents two major advantages with respect to other diffraction

techniques such as LEED or x-ray diffraction (XRD): it is element specific since it is usually possible to find a kinetic energy specific of the element under investigation, and it is local, i.e. it probes the short-range order around the selected emitter giving us information about its neighboring atoms.

The physical process behind XPD is the elastic electron scattering. When we irradiate an atom with photons of enough energy to extract one electron from it, this electron can be ejected through two ways: it can propagate directly into vacuum or it can undergo a number of elastic scatterings with the neighboring atoms of the emitter. Electrons coming from these two paths can interfere giving rise to a diffraction pattern which is very sensitive to the relative atomic positions. If we measure the variation of this photoelectron intensity either with the photon energy or the emission angle we will be able to determine the atomic structure around the emitter atoms.

There are two fundamentally different ways in which photoelectron diffraction can provide structural information. These two distinct modes arise from the form of the angular dependence of the electron scattering cross-section by atoms as a function of scattering angle and electron energy. Fig. 2.9 shows this quantity, the modulus of the atomic scattering factor, for a Cu atom at a few different energies. All curves are normalized to the scattering factor at zero angle. Notice that at the higher electron energies the scattering factor is completely dominated by the peak near the zero angle forward scattering condition. On the other hand, at the lower energies, comparable scattering cross-sections occur over the full range of scattering angles, with a tendency to peak at the 180° backscattering condition as well as in the forward direction.

Of the two modes of photoelectron diffraction, the simplest situation arises through the exploitation of forward scattering at relatively high kinetic energies. Fig. 2.10 (a) shows one situation in which this can be exploited rather simply; a diatomic molecule is adsorbed on a surface in a well-defined orientation (in this case with the molecular axis perpendicular to the surface) and the atom closest to the underlying surface acts as the photoelectron emitter. For zero-angle forward scattering of these photoelectrons by the outer atom of the molecule there is no pathlenght difference between the directly-emitted and forward-scattered components of the wave-field, so in the absence of any phase shift introduced by the scattering, the two components of the wave-field interfere constructively along the intramolecular axis. As the scattering angle increases from zero, a pathlength difference is introduced between the scattered and directly-emitted

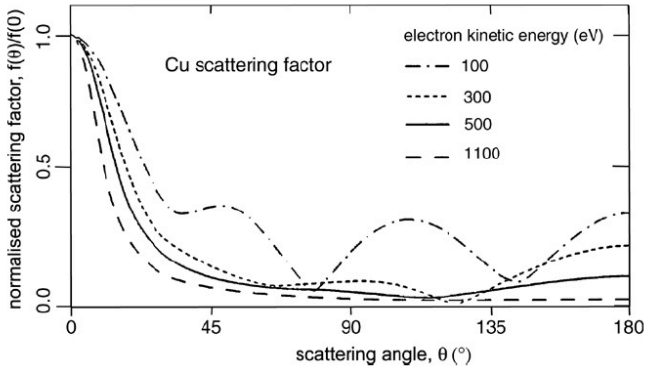

Figure 2.9: Angular dependence of the modulus of the atomic scattering factor for electrons by a copper atom at several different electron energies.

components of the photoelectron wave-field, so the two waves develop a relative phase difference which increases with scattering angle and eventually leads to destructive interference and a minimum in the measured intensity. This effect thus leads to a peak in the angular dependence of the photoemission intensity which is aligned along the intermolecular axis. This peak corresponds to a zero-order diffraction process and its location is independent of photoelectron energy. In practice this simple picture is complicated by the existence of a phase shift with the forward scattering, but providing this is small ($<\pi/2$), the forward scattering diffraction peak is retained. Moreover, the elastic scattering cross-section of the atom is also generally peaked in the forward scattering peak (even if there was no coherent interference). Typically, for electron energies greater than about 500 eV the forward phase shift is small and the scattering cross-section is strongly peaked in the forward direction, so one can determine interatomic directions in adsorbed molecules by searching for these forward scattering, zero-order diffraction, peaks in the photoelectron angular distribution. Of course, a key requirement for exploiting this idea is that the emitter atom lies below the scatter atoms relative to the detector. This means it can be used to determine certain interatomic directions in adsorbed molecules and in crystals and thin films. However, these forward scattering peaks alone cannot provide information on the location of atoms behind the emitter relative to the detector. As such they cannot provide information on the location of adsorbates relative to the underlying solid.

By contrast, the photoelectron diffraction situation in Fig. 2.10 (b), in which the

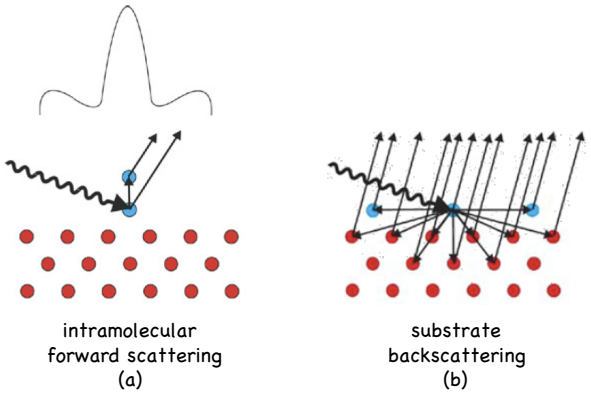

Figure 2.10: On the left is shown the case of intramolecular forward scattering at high photoelectron energy. The resulting form of the photoelectron intensity as a function of the polar emission angle is sketched above. On the right is shown the case in which the adsorbate photoelectrons are backscattered by substrate atoms.

adsorbate photoelectrons are backscattered by the substrate atoms, can provide this information on adsorbate-substrate registry and bond lengths. In this scattering geometry, all the scattering paths involve path length differences relative to the directly-emitted component of the photoelectron wave-field, so the detected photoemission in any particular direction is modulated as the photoelectron energy is changed. For backscattering photoelectron diffraction one thus has the option of extracting the structural information from either angle-scan or energy-scan measurements. Typically these backscattering measurements are undertaken at lower photoelectron energies (below about 500 eV) for which the elastic backscattering cross-sections are largest.

2.4 ALOISA/HASPES beamline

ALOISA *(Advanced Line for Over-layer, Interface and Surface Analysis)* is a multi-purpose beamline for surface science experiments. It was designed to work in a wide spectral range of 100-8000 eV and hosts two experimental chambers: the first one, (original) Aloisa, is dedicated to X-ray diffraction and X-ray spectroscopy experiments, while the second one, HASPES, additionally offers ultraviolet spectroscopy and scattering of the thermal helium atoms. The outline of the complete beamline is displayed in Fig. 2.11. Close to the exit of the synchrotron beam from the storage ring, there

is a switching mirror which lets the beam passing directly into the Aloisa chamber or deflects it (when inserted) to the HASPES chamber.

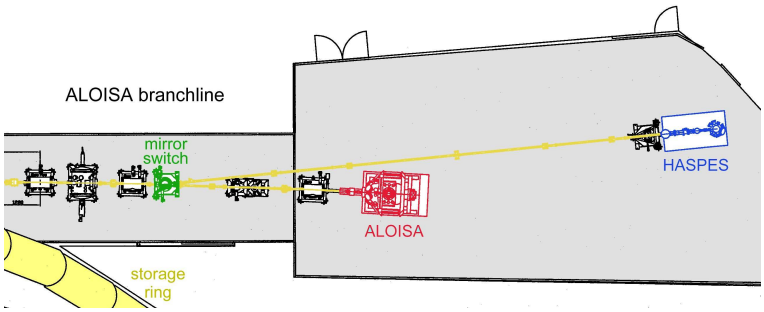

Figure 2.11: The outline of the ALOISA/HASPES beamline.

The ALOISA photon beam is produced by the U7.2 wiggler/undulator insertion device (ID) of the Elettra synchrotron. It consists of a spatially periodic magnetic field, produced by two series of alternately oriented magnets, separated by a user-tunable gap. As the electrons pass through the ID the magnetic field deflects the particles in their orbit in a series of wiggles. The light produced in each wiggle sums along the direction of the ID axis and becomes the X-ray source of the beamline at the pinhole separating the beamline optics from the storage ring. By varying the gap size of the ALOISA ID, it can operate as an undulator in the region of high gap values (∼40-80 mm) with low critical beam energy (100-2000 eV) or as a wiggler in the region of low gap values (∼20 mm) with high critical beam energy. Fig. 2.12 shows the intensity of the photon beam as a function of the photon energy, obtained for different values of the ID gap. For small gap values the oscillations in the spectrum become very dense resulting in the intensity spectrum similar to the one of the bending magnet.

The light is linearly polarized (polarization degree ∼ 95 %) in the plane in which the electrons are wiggled in their trajectory when passing the ID, i.e., in the (horizontal) plane of the synchrotron ring. The monochromator of Aloisa covers the full 140-8000 eV range of photon energy (21). The main characteristic is the possibility to switch between two types of dispersing systems: a plane mirror plus a grating monochromator (PMGM) for the 100-2000 eV range and a Si(111) channel-cut crystal for 3 - 8 keV range (22). The two systems lay side by side and they can be inserted onto the optical path by means of a slide mechanism. The complete optical layout of the beamline is

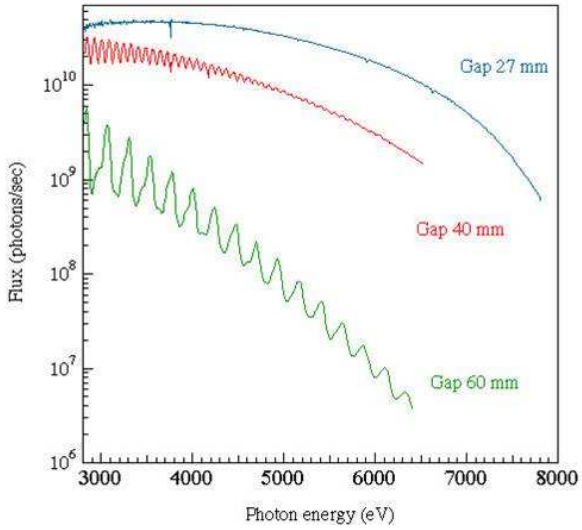

Figure 2.12: The intensity of the photon beam at the exit of the the Aloisa wiggler/undulator ID as a function of the gap value.

sketched in Fig. 2.13.

The light is collected from the pinhole by a paraboloidal mirror (P1) and is collimated towards the dispersing system. The monochromatic beam is focused at the exit slits (ES) by a second paraboloidal mirror (P2). The diverging beam is re-focused on the sample (placed at the center of the experimental chamber ALOISA) by a toroidal mirror (RT), producing a spot of approx. 20 μm $\times$ 150 μm. Another paraboloidal mirror (P3) is used to deviate the beam to the HASPES chamber. No additional refocusing mirror is used in this case due to the very long distance of the HASPES chamber from the beamline optics (14m). This way a low angular divergence of < 0.3 mrad is obtained. The system is characterized by the absence of an entrance slit. Moreover the optics are used in the sagittal focusing configuration (i.e., perpendicular to the scattering plane) to minimize the aberrations in the dispersive plane induced by the slope errors. All the optics are designed to work at grazing incidence with a deflection angle of 1° for P1, P2 and RT. Due to the high power density generated by the insertion device, the first paraboloidal mirror and the PMGM and the channel cut crystal are water cooled. All the optical surfaces have a gold coating to minimize chemical contamination and losses in the photon flux. The photon flux through the exit slits at 400 mA of ring current is approximately 2×10^{12}photons/s/0.1%bw.

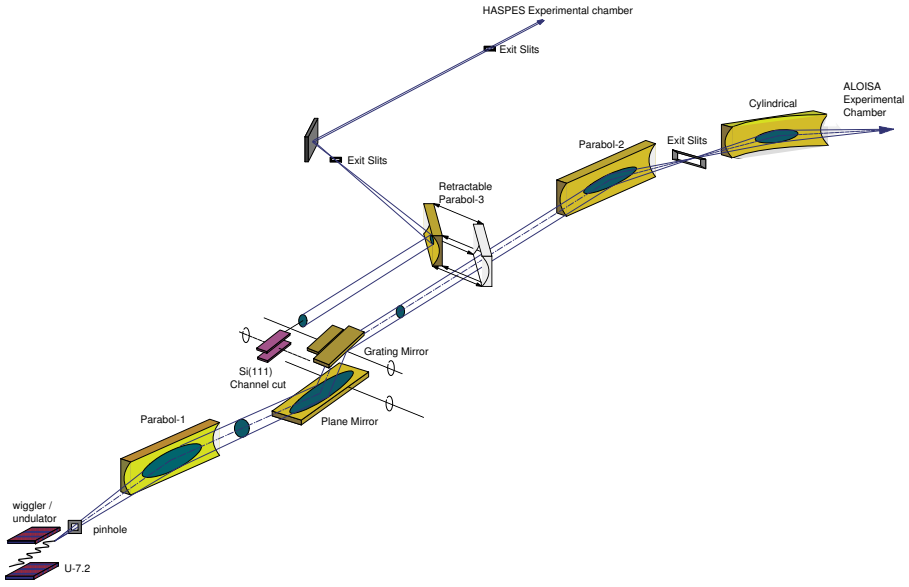

Figure 2.13: Optical layout of the ALOISA/HASPES beamline.

2.4.1 The ALOISA experimental chamber

The Aloisa experimental chamber is composed of two parts: a hemispherical void, dedicated to the sample preparation (preparation chamber), and a cylindrical void hosting electron analyzers and photon detectors for sample investigations (main chamber). A sketch of the entire chamber is shown in Fig. 2.14.

The preparation and main chamber are coupled via large bronze ball bearing and a system of sliding O-rings. This configuration allows the complete rotation of the main chamber (with all detectors) around the SR beam axis, while the preparation chamber stands still. Two differential pumping stages allow the rotation of the main chamber and the frames, maintaining at the same time a constant base pressure of 10^{-11} mbar inside the main chamber.

The preparation chamber is equipped with a MBE (Molecular Beam Epitaxy) cryopanel which can host up to four evaporation cells. The cryopanel also holds two quartz microbalances for deposition flux calibration. A gas line allows high purity gases to be bled into the chamber. The ion gun for the Ar^+ bombardment enables sample sputter-

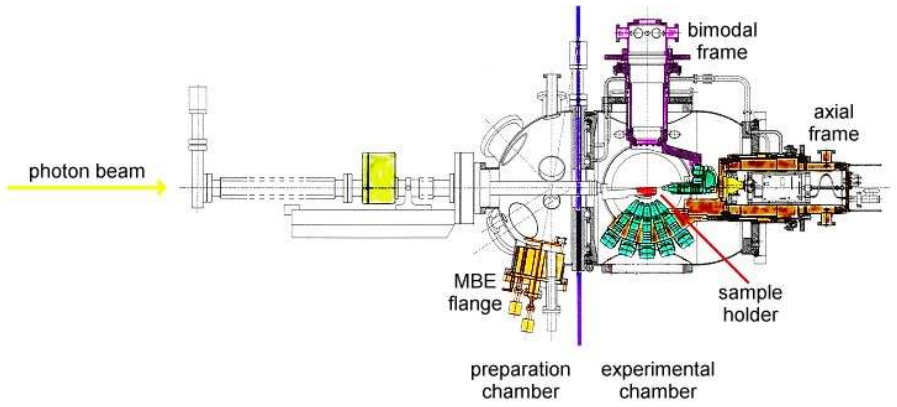

Figure 2.14: Schematic of the ALOISA chamber.

ing with ion energy of up to 3 keV. A RHEED system (Reflection High Energy Electron Diffraction) with electron energy of 15 keV and the beam impinging to the surface at a grazing angle is available for checking the surface symmetry in-situ during deposition. The preparation chamber is additionally equipped with the sample transfer system and fast entry-lock allowing quick sample exchange.

In the main chamber, the detectors are hosted on two frames which are mounted inside the rotating element. The axial frame is mounted at the end of the cylindrical element and can rotate around the SR beam axis independently from the chamber. Five 33 mm electron analyzers are mounted on this frame. They are primarily dedicated for the APECS (Auger Photoelectron Coincidence Spectroscopy). There is also a phosphorous plate with the CCD camera mounted on the axial frame for the beam alignment with respect to the sample. The bimodal frame is mounted on the side of the cylindrical main chamber and can rotate around an axis, perpendicular to the SR beam. This axis also rotates around the SR beam together with the main chamber. The bimodal frame hosts a 66mm hemispherical electron analyzer for angle resolved photoemission (ARXPS) and photoelectron diffraction (PED). There is one Si-diode behind 1 mm collimators for measuring the total current for X-ray diffraction (XRD) and reflectivity (XRR). The bimodal frame additionally hosts two energy resolved (Peltier-cooled) photodiodes (by Eurisis) operating in single-photon counting mode for X-ray diffraction. A wide-angle-acceptance channeltron is mounted on the axis of the bimodal frame, which is used for measuring the partial electron yield in near edge X-ray absorption

fine structure (NEXAFS) experiments. The channeltron is equipped in front if its apex with an additional grid, held at adjustable negative potential to repel the low-energy multiple-scattered electrons. This way only high-energy Auger electrons contribute to the partial-yield signal.

The sample is placed onto a six-degree of freedom manipulator which is mounted into the preparation chamber and can be inserted into the main chamber. The SR beam passes through the whole manipulator and impinges at grazing incidence on the sample. Three rotations of the sample holder allow the sample to be rotated around the synchrotron beam (R_1) in order to select the desired surface orientation with respect to the photon polarization, the required grazing angle (R_3) and the azimuthal orientation of the surface symmetry axis with respect to the scattering plane (R_2). All possible rotations of the manipulator are shown in Fig. 2.15.

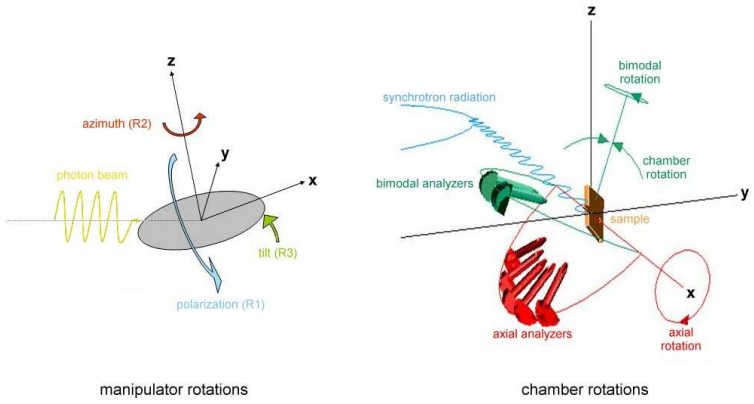

Figure 2.15: Sketch of the angular movements available by the manipulator and the experimental chamber.

Together with the experimental chamber rotation this allows completely arbitrary configuration between the SR beam, the sample and detectors. All rotations of the manipulator and the main chamber as well as the translational movement of the manipulator are motorized and computer navigated. The sample holder is equipped with two tungsten filaments for sample heating through electron bombardment up to 1100 K. Additional gas pipeline enables the liquid nitrogen cooling of the sample down to $\sim$ 150 K. A custom-made Labview program has been developed for the data acquisition, detectors control and movements of the experimental chamber and the manipulator.

2.4.2 The HASPES experimental chamber

The HASPES (*Helium Atom Scattering and Photoelectron Spectroscopy*) vacuum chamber consists of a main upright standing cylindrical void, a pre-chamber with helium atom source and a chamber for the helium detection with a quadrupole mass spectrometer. A top view scheme is reported in Fig. 2.16 a).

HASPES uses the low-energy monochromatic SR beam in the 120-1000 eV energy range. The SR beam enters the HASPES chamber through the He detection part so the beam path coincides with the He scattered beam, but has the opposite direction. The main chamber hosts a vertically mounted VG CTPO manipulator with six degrees of freedom and high-precision positioning. The chamber has a fixed source-sample-detector angle of 110° for HAS and 55° for XPS, as can be seen in Fig. 2.16 b). The three possible manipulator rotations are presented in the right-hand side of the same figure. By rotating the sample around R_1 one changes the incidence angle of helium atoms and SR beam. Rotation around R_2 varies the angle of the surface symmetry axis with respect to the scattering plane. Tilt rotation (R_3) allows the sample to incline around a chosen surface axis. All the manipulator rotations are motorized and controlled via a home-made Labview program, which also manages the data acquisition. The manipulator is provided with a thermal link to a small cryostat filled by circulating liquid nitrogen or liquid helium. Together with the tungsten filaments or resistive (ohmic) heating (in case of semiconducting sample) it allows the sample temperature to be maintained in the 100-1100 K range.

The pumping system ensures that the ratio of the stagnation pressure, p_0, inside the nozzle to the background pressure in the beam chamber, p_1, is as high as $p_0/p_1 \approx 10^7$, so that no shock structures occur in the expansion region and a smooth transition from continuum to free-molecular flow takes place a few mm region downstream from the nozzle. The pressure of He in the stagnation chamber can be set in the 10-100 bar range, defining the flux and the monochromaticity of the He beam.

A skimmer with the shape of truncated cone with aperture diameter of 0.5 mm follows the nozzle at a distance of about 25 mm and defines the angular divergence of the beam, which equals 8×10^{-6} sr. Just downstream from the skimmer, the chopper selects He beam pulses for inelastic scattering measurements. The chopper is followed by another collimator, through which the He beam enters the experimental chamber

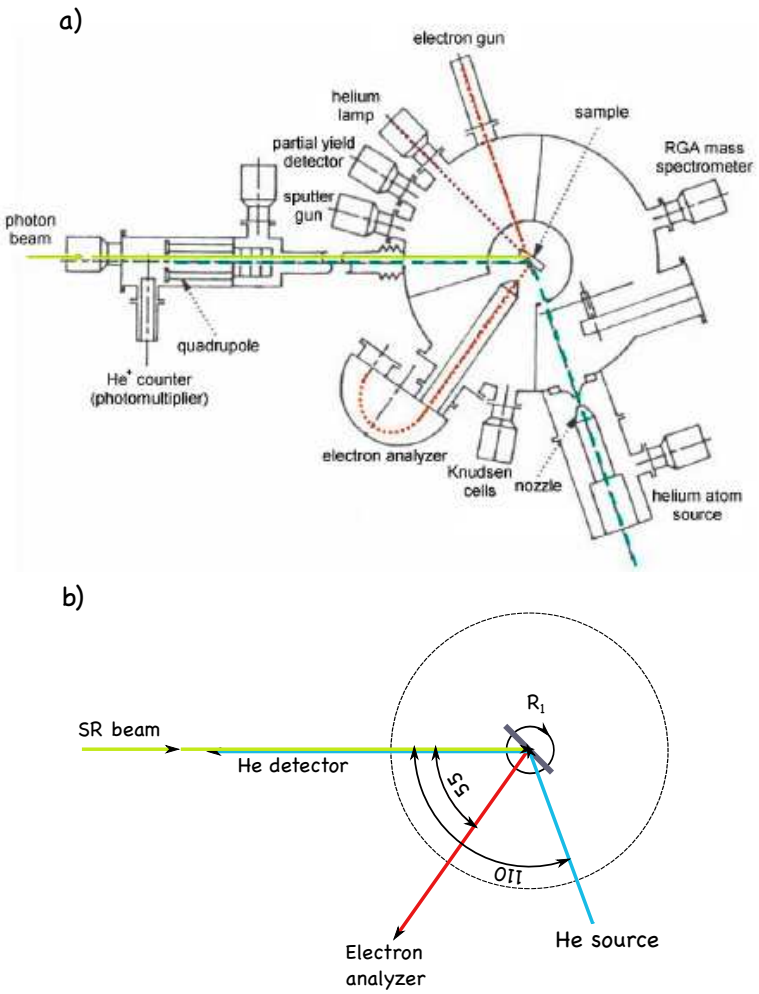

Figure 2.16: a) The HASPES chamber and the belonging equipment. b) The HASPES chamber geometry.

and presents a cross section of about 0.7 mm at the scattering center. The beam energy is selectable between 18.6 and 100 meV by controlling the temperature of the stagnation chamber.

Scattered He atoms enter the detection chamber through another set of collimators. Neutral atoms are first ionized by the transverse electronic beam and then filtered through the quadrupole mass spectrometer assembly. Electrons in transverse beam have kinetic energy of about 100 eV, corresponding to the maximum cross section for the ionization of He atoms, where the ionization efficiency reaches about 10^{-5}. The ions entering the quadrupole region are then selected according to the desired charge to mass ratio, e/m, with an accuracy of 0.05 e.m.u.. Finally, the He^+ ions followed by knocked-out electrons are multiplied through a series of 17 dynodes and counted by a computer.

On the main chamber are also attached a differentially pumped helium lamp to provide ultraviolet radiation and a 150 mm high resolution hemispherical electron analyzer. The latter hosts a 48-segment anode behind two serially coupled multichannel plates (MCP) and offers an energy resolution of 0.5 % of the pass energy, reaching the maximum resolution of 17 meV. There is also an electron gun mounted in the scattering plane and emitting the electrons with 10-1000 eV kinetic energy that offers the angularly well resolved electron detection - LEED technique. A channeltron is also mounted at an angle of 50° from above the horizontal scattering plane for the partial electron yield detection in the near edge X-ray absorption fine structure (NEXAFS) experiments. The main chamber is furthermore equipped with an ion gun for Ar^+ sputtering and a liquid-nitrogen cooled cryopanel, hosting three Knudsen evaporation cells. There is also a fast entry lock allowing quick sample exchange.

2.5 APE beamline

The APE *(Advanced Photoemission Experiments)* beamline consists of two branches; the High-Energy (HE) and Low-Energy (LE) branch, each one using the radiation from different undulators. The HE branch works with photon energy ranging from 200 to 1600 eV used for absorption and core-level photoemission experiments. The LE branch has been built for ARPES experiments and works with photon energies ranging from 10 eV to 150 eV. There are two extra chambers: Keer and the STM chambers. The Kerr

chamber is used for sample preparation and measurement of Magneto-Optical Kerr Effect (MOKE). Scanning Tunnel Microscopy (STM) at room temperature is available in the STM-chamber.

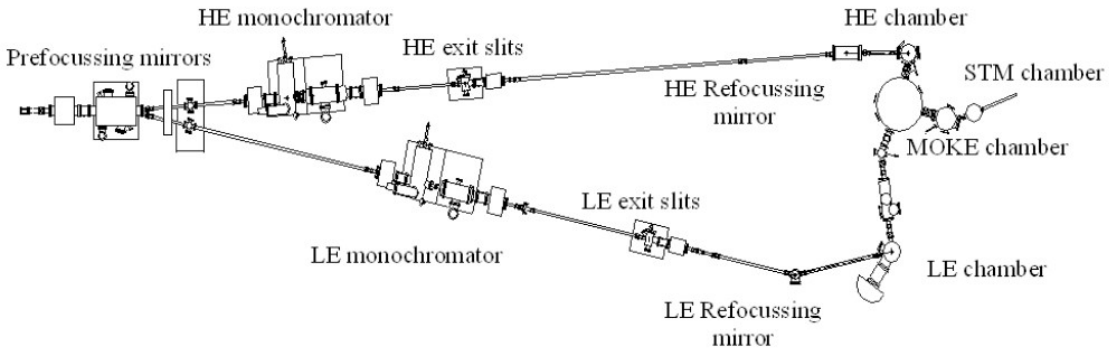

Figure 2.17: Layout of APE beamline.

All the chambers are interconnected through UHV transfer chambers. The Fig. 2.17 shows the layout of the APE beamline. Two photon beams coming from their respective undulators (not show in the picture) arrive in the pre-focus mirrors forming an angle of 2 mrad to each other. The beams are deviated to the HE and LE branch, where they are monochromatized and refocused onto a 150×75 micrometer spot on the sample surface in the HE and LE chambers. The HE branch monochromator operates in the 200-1600 eV energy range by means of three different grating of 900, 1400 and 1800 lines/mm, each on dedicated at a different energy range. The LE branch monochromator operates 10-140 eV also using three different variable spacing grating; 700, 1200 and 1600 lines/mm.

In the following sections I will describe only the apparatus used during the X-ray spectroscopy experiments on the Tetraaza-CuPc/Au(100) system.

2.5.1 The High Energy Chamber

The HE chamber is dedicated to absorption core level photoemission experiments. The chamber is kept in Ultra High Vacuum (UHV) by an ionic pump and a Ti gathering pump. The usual pressure is around 3×10^{-10} mbar, but when the system is cooled, the pressure can reach values lower than 5×10^{-11} mbar.

The chamber is equipped with a position controlled manipulator with 0.01 mm of spatial resolution that allows the automation of the sample mapping. The spot size on the sample, after the refocusing of the toroidal mirror, was about 200x100 μm (horizontal$\times$vertical) in our experiments. The manipulator can change only the polar angle, the azimuthal angle is fixed. A small coil, which fixed position in reference to sample, is used to magnetize the sample in the XMCD measurement.

The photoemission intensities in the XPS are measured with a hemispherical electron energy analyzer (Omicron EA 125). The analyzer inlet is centered at 45° from the photon beam line. The best achievable instrumental resolution is about 10 meV. For absorption experiments we can measure in total electron yield mode by monitoring the sample current extracted from the ground and read by a Kethley picoampermeter, or in partial electron yield mode by means of an in situ channel electron multiplier operated alternatively in current or pulse counting mode. A photodiode detector or in alternative a semitransparent molybdenum mesh is used to measure the intensity of the beam entering the HE end station which is used to normalize the recorded spectra.

2.5.2 The Kerr Prepration Chamber

The sample preparation is carried out in the KEER chamber. The chamber is equipped with an ion-gun, used for back-sputtering; and a copper heating stage, used for annealing when a precise temperature control is required. The heating is done by electron-bombardment from a tungsten filament placed behind of the stage, and the temperature is measured by mean of tungsten-rhenium thermocouple; the maximum temperature is 650°C. For higher temperatures the annealing can be done directly at the molybdenum manipulator by electron bombardment; the maximum temperature is about 1000°C. The temperature measurement, however, done by thermocouple, is not precise in this manipulator. In any case, for temperatures above 400°C, it is possible to use an electronic pyrometer for temperature calibration. For the surface characterization, it is available LEED/Auger instrumentation: LEED apparatus is a rear-view 4-grid SPECTALEED optics by Omicron, with the EG&G lock-in amplifier for Auger spectroscopy; the size of the electron beam on the sample is less than 300 μm. This chamber also has a set of flanges that allow the installation of up to three different evaporators. There is a retractable water cooled quartz microbalance for the evaporation flux calibration and a molybdenum mask, used for the growth of wedge films.

The KEER chamber has a manipulator that allows the positioning of the sample for the different procedures available in the chamber. The manipulator arm has an 'L' shape, with a liquid nitrogen cryostat on the top end. Improvements have been designed to allow the freedom at polar angle, which is important for grazing sputtering; and the increasing of thermal contact between the sample holder and the colder finger.

3

Organic semiconductor molecules on TiO_2(110)-1×1

3.1 Introduction

TiO_2 and organic semiconductors are well suited to be integrated into hybrid architectures for the development of novel devices in molecular electronics. They have already been successfully combined for the construction of high efficiency solar cells (23) (24), transistor (25), rectifiers (26) etc. Nevertheless little attention was payed to the microscopic details of the growth and interaction of organic moelcules on TiO_2 surfaces. In fact, dielectrics have been hitherto regarded as inert substrate where molecules are simply physisorbed without modification of the molecular electronic structure nor of the molecular self-assembly mechanism. Only very recently, the strong anisotropy of the rutile TiO_2(110) surface has been tentatively exploited as a template to drive the oriented growth of planar organic molecules, such as phthalocyanines (27), porphyrins (28) and perylene-derivatives (29) (30). In particular, the TiO_2(110) surface attracts much attention thanks to the possibility of changing its catalytic and charge transport properties by controlling the concentration of defects (oxygen vacancies) in the surface layers (either by thermal annealing or by ion bombardment). The desorption of oxygen atoms leads to the appearance of a new electronic state in the band gap, which is associated with a redistribution of the local excess of charge among multiple Ti sites around the oxygen vacancy (31). The peculiarity of its conductive properties makes this substrate very attractive for the study of the interaction with molecules able to act

as donor or acceptor of charge. In view of this, we have chosen four different molecular species that are of relevant interest in electronic applications: C_{60}, pentacene, perylene and perylene-tetracarboxilic-aciid-diimide (PTCDI). From an electronic point of view they can be regarded as electron donors (pentacene and perylene) or electron acceptors (C_{60} and PTCDI). A schematic illustration of the investigated molecules is shown in Figure 3.1. Apart from the highly symmetric C_{60} molecule, the choice of anisotropic planar molecules better matching the substrate lattice is very promising for the improvement of the coherence of the growing film. This route has been attempted by deposition of uniaxial molecules like anthracene (32), α-sexithiophene (6T) (33), and para-sexiphenyl (6P) (34). The substrate anysotropy was effectively found to drive the azimuthal orientation of 6T and 6P multilayer films. However, the natural direction of growth of the bulk molecular crystal was still found to dominate the molecular aggregation from the very first layer, that is, standing up orientation for sexiphenyl and lying down orientation for sexithiophene. On the contrary, anthracene was reported to form ordered planar phases in the monolayer range.

Here we show how the chosen molecules (pentacene, PTCDI and perylene) grow on the TiO_2(110)-1×1 surface keeping the long axis parallel to the surface along the [001] direction. In the case of pentacene, the monolayer phase mimics the structural arrangement of the molecular bulk crystal in the (010) plane, allowing to keep a lying down orientation in the next few layers.

The STM measurements presented in this chapter have been performed in collaboration with the ESISNA group (CSIC-ICMM Instituto de Ciencia de Materiales de Madrid) whereas the HAS and spectroscopic measurements have been performed on the ALOISA-HASPES beamline. The TiO_2 sample was prepared in ultrahigh vacuum by repeated Ar^+ sputtering cycles, followed by annealing at temperatures at about 1100 K. All the molecules were vapor-deposited onto the substrate from borum nitride crucible or home-made tantalum crucibles. The evaporation temperature for the different molecules are shown in table 3.1.

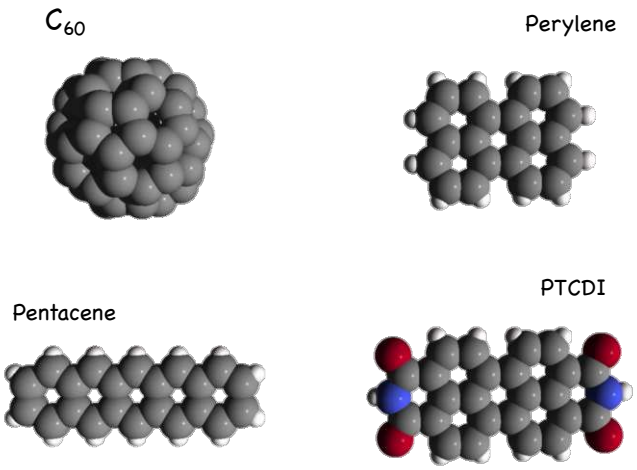

Figure 3.1: Schematic representation of the different organic molecules sublimated on the TiO_2(110) surface.

Table 3.1: Evaporation temperatures for the deposited organic molecules.

Molecule	C_{60}	**Pentacene**	**PTCDI**	**Perylene**
purity [%]	98 (Sigma Aldrich)	99.5 (Sigma Aldrich)	98 (Alfa Aesar)	98 (Alfa Aesar)
Temperature[K]	700-750	450-470	670-690	390-410

3.2 The rutile TiO_2(110)-1×1 surface

Bulk rutile TiO_2 has a tetragonal unit cell with two TiO_2 units per cell, as shown in Fig. 3.2. The Ti atoms occupy the corners and body-center positions in each unit cell. Each Ti atom is coordinated to six neighboring O atoms situated at the vertices of a distorted octahedron. Each O atom is coordinated to three Ti atoms, with all three O-Ti bonds lying in one plane.

The structure may best be pictured as chains of TiO_2 octahedra, lying parallel to the [001] direction, with adjacent octahedra along a chain sharing an edge (Fig. 3.3a). In adjacent chains the octahedra share vertices, and are rotated by 90° about the [001] axis. The apical Ti-O bonds lie along the [110] or [1$\bar{1}$0] directions.

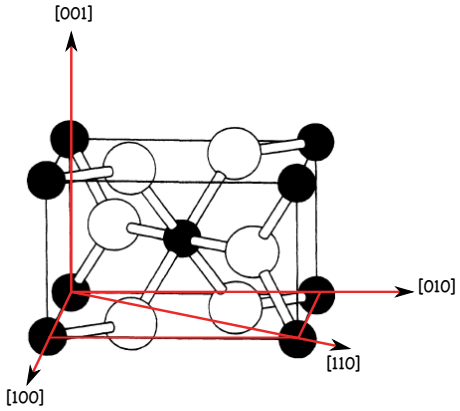

Figure 3.2: The tetragonal bulk unit cell of rutile TiO_2

On the unreconstructed (110) surfaces of TiO_2 these octahedra are truncated giving rise to different atomic coordinations (see Fig. 3.3b). Along the $[1\bar{1}0]$ direction, rows of six-fold coordinated Ti atoms (as in the bulk) alternate with fivefold coordinated Ti atoms with one dangling bond perpendicular to the surface. Two kind of oxygen atoms are created as well. The equatorial planes of the octahedra of O atoms around the six-fold coordinated Ti atoms are perpendicular to the surface. This gives rise to chains of two-fold coordinated O atoms, parallel to the [001] direction, protruding out of the surface by approximately 1.5 Å. These O atoms are called "bridging O atoms". Rows of three-fold coordinated O atoms lie in the plane of the Ti atoms, connecting the chains of six-fold and five-fold coordinated Ti atoms. The surface relaxations occur mainly perpendicular to the surface. The bridging oxygen atoms are measured to relax downwards considerably, and the six-fold coordinated Ti atoms upwards. The five-fold coordinated Ti atoms move downwards and the neighboring threefold coordinated oxygen atoms upwards, determining a large corrugation of the surface along the $[1\bar{1}0]$ direction. The surface unit cell is characterized by a centered rectangular arrangement with the shorter unit cell vector (2.959 Å) along the [001] direction and the longer one (6.495 Å) along the $[1\bar{1}0]$

Fig. 3.4(a) reveals the rectangular surface net for the (110) surface, which is shown more explicitly in the direct lattice points of Fig. 3.4(b). Fig. 3.4(c) presents the corresponding surface reciprocal lattice with the first Surface Brillouin Zone (SBZ) and its special points $\bar{\Gamma}$, $\bar{X}$, $\bar{Y}$ and $\bar{S}$. The corresponding 2D He diffraction pattern is reported in Fig. 3.5.

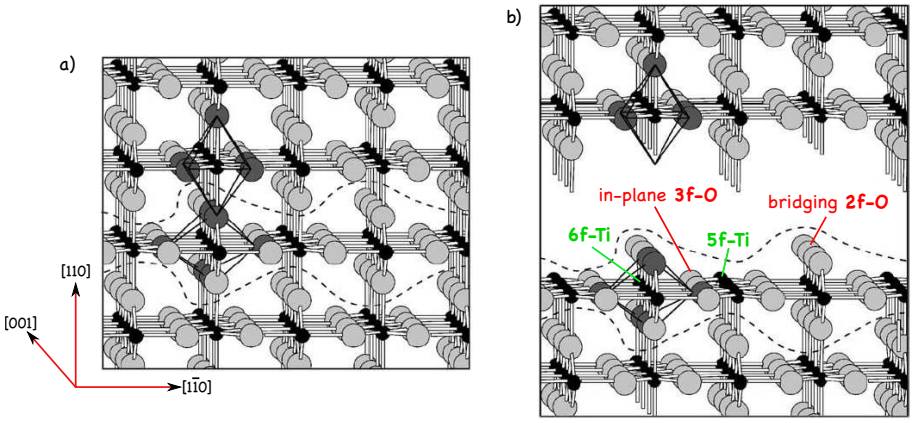

Figure 3.3: a) Ball and stick model of the rutile crystal structure in which it is possible to see the 90° alternating arrangement of the octahedra along the [110] and [1$\bar{1}$0] directions. The crystal cutting along the dashed lines produces the characteristic termination of the unreconstructed TiO_2(110) surface b).

There is wide agreement on the fact that the surface electronic structure is not too different from that of the bulk (35, 36). The occupied states are mostly O 2p derived. The left side of Fig. 3.6 shows the molecular orbital energy-level diagram for $(TiO_6)^{8-}$ cluster representing the environment around Ti in TiO_2 (37). We see that the 48 valence electrons completely fill the bonding and non-bonding orbitals having mostly O 2p character, leaving unfilled the anti-bonding orbitals $2t_{2g}$ and $3e_g$ having mostly Ti 3d character. Fig. 3.6 (right side) shows the shape of the valence band respectively at 21.2 eV (He I) and 140 eV.

The octahedral coordination causes a crystal field splitting of the d orbitals in the two sub-bands: $2t_{2g}$ and $3e_g$ (see left side of Fig. 3.7). The $3e_g$ orbitals (d_{z^2} and $d_{x^2-y^2}$) point directly toward the oxygen ligands forming s-type orbitals. The $2t_{2g}$ (d_{xy}, d_{xz}, d_{yz}) point in between the oxygen neighbors and form π-type bonds. The crystal-field splitting is clearly seen in X-ray Absorption, see Fig. 3.7 (right side).

When point defects (predominantly O vacancies) are created on TiO_2 surfaces, they cause a dramatic change in electronic structure. Usually, surface defects are created by ion or electron bombardment or by heating to high temperature and quenching. Because of their coordinative undersaturation, O atoms from the rows are thought to be removed more easily than that in the main surface plain. Removal of a neutral oxygen leaves behind two electrons which previously occupied O 2p levels in the valence band.

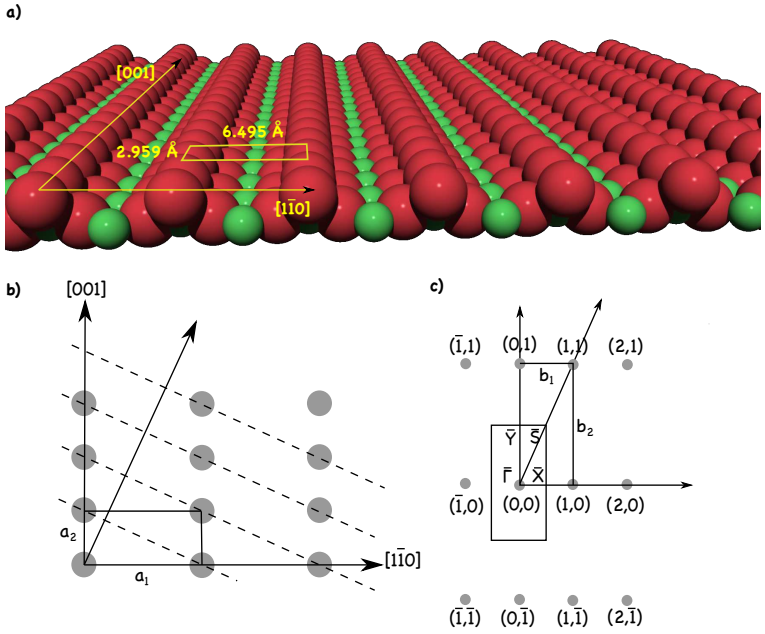

Figure 3.4: a) Model of the ideal (110) surface of rutile TiO2. The surface unit cell is shown by the yellow rectangle. In b) and c) it is reported the corresponding direct and reciprocal lattice.

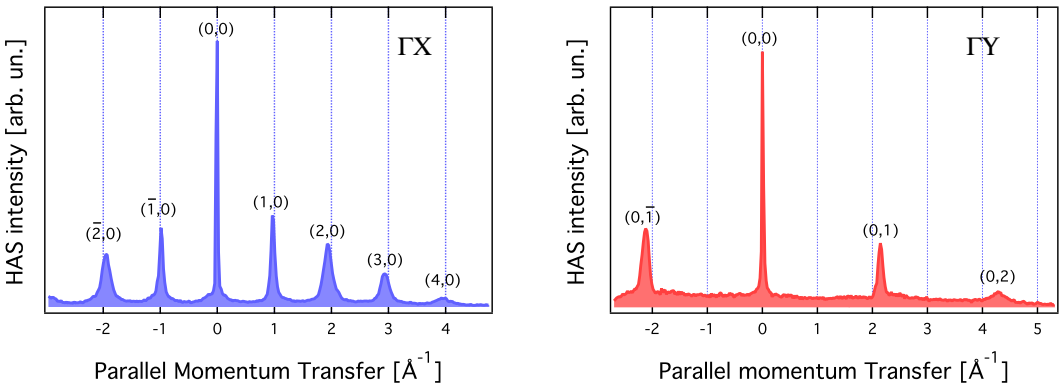

Figure 3.5: The 2D He diffraction pattern for rutile TiO_2 (110) in the ΓX (left) and ΓY (right) directions.

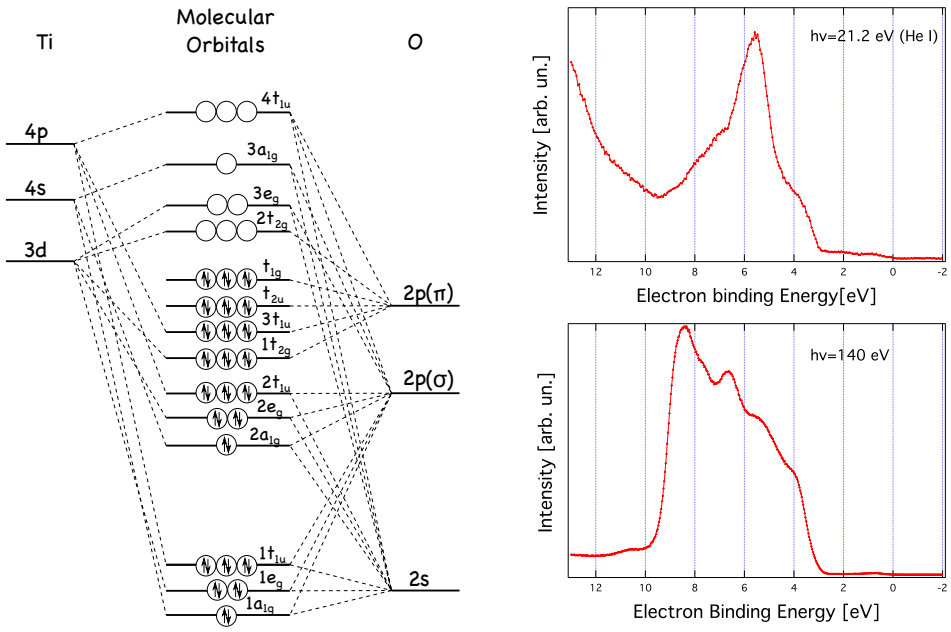

Figure 3.6: (Left) Molecular orbital energy-level for $(TiO_6)^{8-}$, representing the environment of Ti in TiO_2. (Right) Valence band of TiO_2 probed by photoemission spectroscopy using two different photon energy: 21.2 eV (top) and 140 eV (bottom)

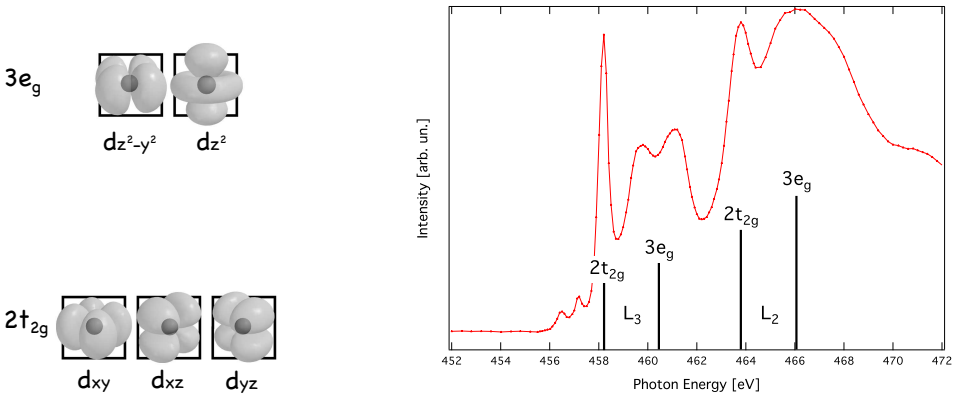

Figure 3.7: (Left) Sketch of the crystal field effect of the oxygen ligands on the Ti 3d orbitals. (Right) X-ray Absorption Spectra on the Ti 2p edge of the rutile TiO_2(110) surface.

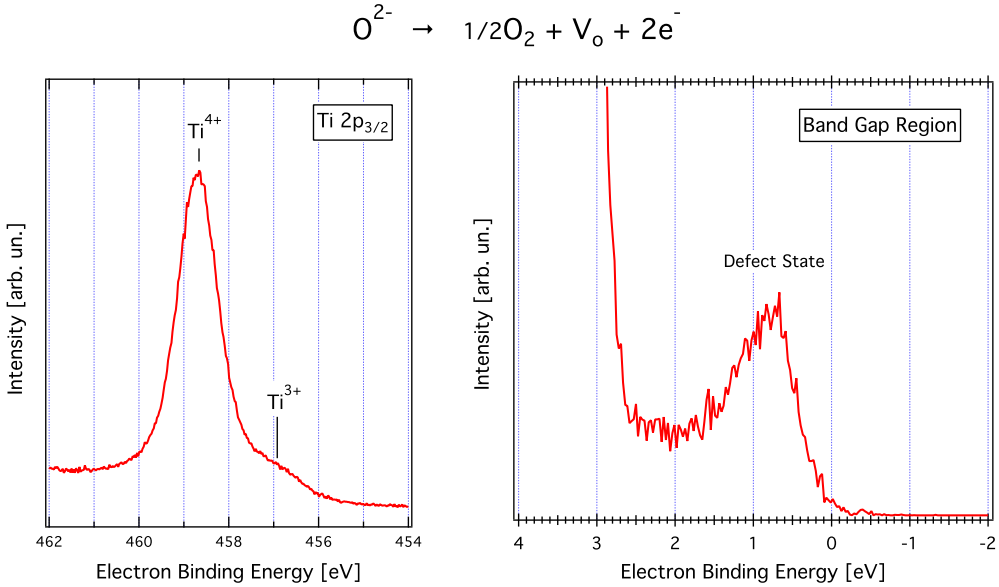

Figure 3.8: Experimental evidences of the change in oxidation state of TiO_2 upon removal of O atoms. On the right, the Ti $2p_{\frac{3}{2}}$ core level photoemission spectra shows a clear shoulder a lower binding energies which corresponds to Ti atoms with oxidation state 3+. On the left is reported the band gap region probed at 140 eV in which it is possible to see the new electronic state at 0.8 eV below the Fermi level.

These states are no longer available, and the electrons must go into the conduction band, the bottom of which is formed by Ti 3d states. Since the 3d states are rather localized, this corresponds to a change of the formal oxidation state, from Ti^{+4} to Ti^{+3}. This change in oxidation state results in two observable consequences: a shift in the 2p core level binding energy of the reduced Ti atoms (Fig. 3.8, left side), and the presence of an new electronic state in the band gap region at approximately 0.8 eV below the Fermi level (Fig. 3.8, right side).

The fact that the new electronic state is primarily Ti 3d-derived is corroborated by its resonant behavior across the photon energy range that encompasses the Ti 2p → Ti 3d excitation threshold (Fig. 3.9). The position and amplitude of the defect surface state depend on the amount of surface reduction.

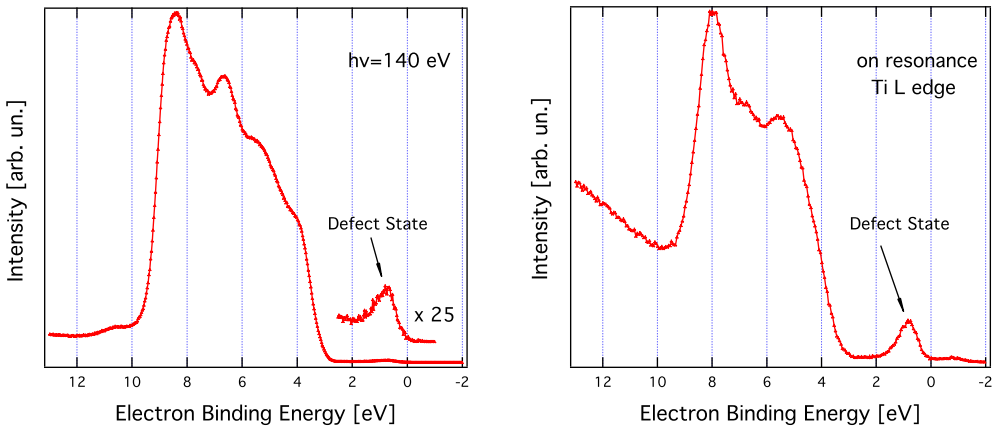

Figure 3.9: Resonant behavior of the Ti 3d state on the Ti 2p ionization threshold. The weak intensity of the defect state probed at 140 eV (right) is clearly enhanced when the photon energy is tuned across the Ti 2p ionization threshold (left).

In this case TiO_2 will no longer behave as an insulating material but as an n-type semiconductor, with a bulk conductivity that allows the use of STM. Fig. 3.10 shows an atomically resolved STM image of the clean TiO_2 (110)-1×1 surface recorded at a sample bias of 1.5 V, where we can see bright rows running along the [001] direction. These bright rows correspond to the in plane five-fold coordinated Ti atoms and not to the protruding oxygen rows as one could expect according to the topography (38)(39). This is a clear case of the not-straightforward interpretation of STM image mentioned in section 2.1. As a positive bias is applied to the sample, electrons are being injected

into the TiO_2 empty states that we know are mainly due to the Ti atoms. For this reason we can attribute the observed bright rows running along the [001] direction to the Ti rows, as it has been determinated by different theoretical calculations for these tunneling conditions. Complementary, the dark rows, also running along the [001] direction, correspond to the protruding oxygen rows. The periodicity along the $[1\bar{1}0]$ direction is approximately 6.5 Å, which is in good agreement with the expected value for the 1×1 surface. The bright spots in between Ti rows can be associated to O vacancies or OH groups. The presence of OH groups is due to the dissociative adsorption of water molecules on the O vacancies (40). O vacancies are known to be particularly reactive and are responsible of the catalytic properties of TiO_2 surface.

For our experiments, we have used several samples of TiO_2(110) from Mateck, with thickness ranging from 0.5 to 1 mm. Once degassed, the surface is prepared by 10-20 min of Ar^+ ion bombardment at 1 keV followed by annealing up to 1100 K, with a maximum pressure in the 10^-8 mbar range. After this treatment the sample, initially transparent, assumes a characteristic black color with a reflective surface, see Fig. 3.11. We have quantitatively verified that this procedure yields the best (1x1) HAS diffraction pattern in term of both peak intensity and peak width, i.e. lowest density of surface defects and largest domain size (mean terrace width of ∼1000 Å). In this condition, most of the oxygen vacancies are confined in the subsurface region. This is also confirmed by the presence of a weak Ti 3d band gap state, which may be better detected at the resonance with the Ti 2p ionization threshold (31). Lower temperature annealing (blue sample) yields a larger density of surface defects that additionally deteriorates the ordering of the molecular phases.

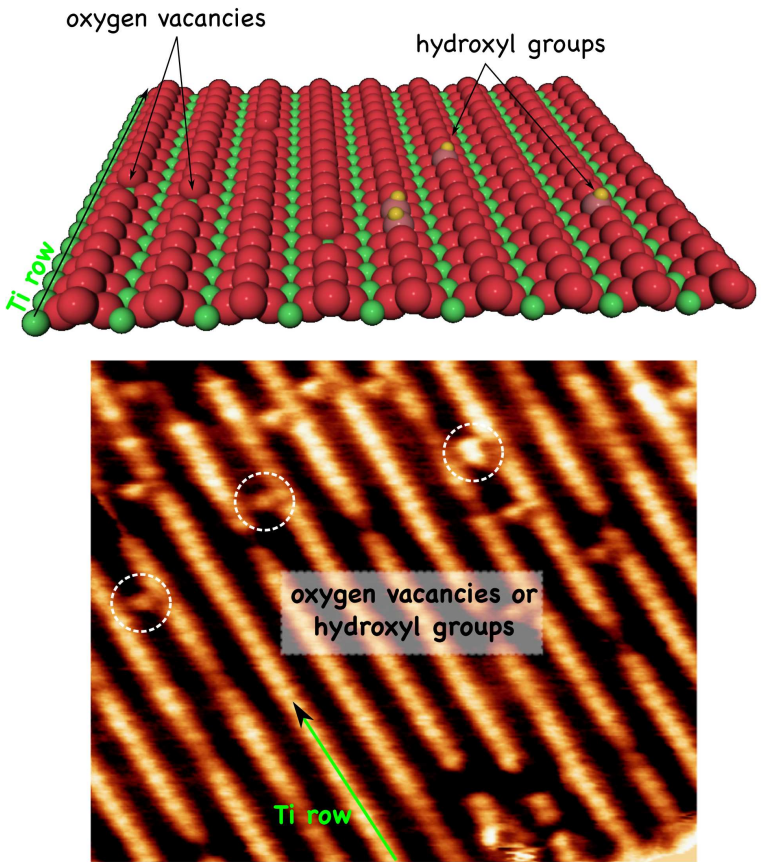

Figure 3.10: (Bottom) Atomically resolved STM image of the clean TiO_2 (110)-(1×1) surface. Bright rows correspond to Ti-5f rows, which extend along the [001] direction (green arrow). Point-defects are also visible as bright spots, which can be associated with oxygen vacancies or hydroxyl groups (dashed circles). STM parameters: (80Å×67Å), I=0.17 nA, V=1.5 V. (Top) Sketch of the TiO_2(100)-1×1 surface corresponding to the STM image.

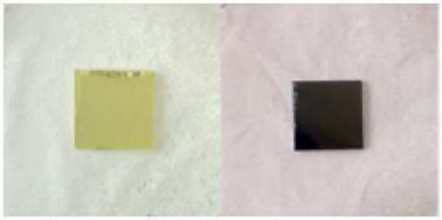

Figure 3.11: Two different reduction levels of the TiO_2 sample. After several cycles of sputtering and annealing the sample changes from a transparent yellow (stoichiometric) to a black color (reduced).

3.3 C_{60}

C_{60} is possibly the most studied representative of fullerenes. It is composed by 60 carbon atoms arranged in a spherical shape formed by 20 hexagon and 12 pentagons with a van der Waals diameter of approximately 11 Å (see Fig. 3.1). C_{60} molecules have been successfully tested in the fabrication of field effect transistor (41) or solar cells(42), either by themselves or in combination with other organic molecules. Besides, it is being tested in many other application as catalysis, superconductivity, non-linear optics etc. (43, 44).

As a consequence of the huge number of possible applications, it has been extensively studied by surface science. When deposited on metals, C_{60} molecules form well ordered close-packed structures, where molecules are usually physisorbed on the surface with distance close to the van der Waals diameter (45, 46). This means a small interaction with the substrate which, however, is able to lock the orientation of the cage. In the cases where this interaction is larger, a modification of the molecular orbitals takes place, together with the alteration of the intrinsic C_{60} properties.

In this section we study the interaction of C_{60} molecules with the TiO_2(110)-1×1 surface by means of STM, LEED, HAS, NEXFAS, XPD and DFT calculations.

3.3.1 Film structure determination by STM and HAS

The structure and order of the C_{60} sub-monolayer phase has been addressed simultaneously by STM and LEED and indipendently by HAS diffraction experiments.

After sub-monolayer deposition on the substrate held at room temperature, we see the formation of compact islands always attached to a substrate step edge (see Fig. 3.12). Only very few islands grow directly on terraces suggesting that a nucleation site with a considerable cohesive energy, such as step edges or pinned molecules, is required. After nucleation, molecules can condense into islands, on the lower terraces, via the van der Waals intermolecular interactions.

A closer inspection of the islands reveals bright spherical features corresponding to single C_{60} molecules, see Fig. 3.13 a). The same STM image is replotted in Fig. 3.13 b) with a different color scale in order to enhance the contrast among single C_{60} molecules and that among the oxygen rows, which correspond to the dark troughs (see the previous section). In this way, it is possible to understand the adsorption site of

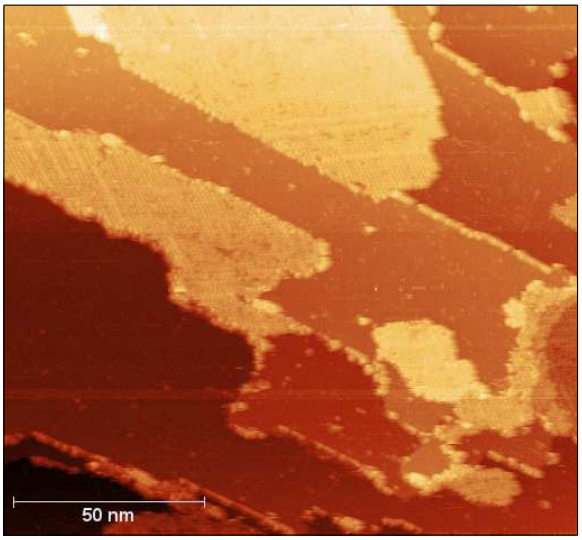

Figure 3.12: STM image of the surface after evaporation of $\sim$ 0.5 ML of C_{60} at RT. We observe the formation of C_{60} islands which start growing from the step edges into the lower terraces.

the C_{60} molecules with respect to the substrate. Although the image suffers a bit of deformation due to the piezo drift, it is possible to see that the Ti rows (white lines) are aligned with the center of the molecules. This means that molecules are adsorbed on top of the 5f-Ti rows of the surface.

The regular order of C_{60} islands is responsible for the diffraction pattern revealed either by LEED and HAS experiments. In the LEED pattern the new spots present a p(5×2) superlattice, compatible with the five-fold periodicity detected by HAS along the ΓY reciprocal direction, see Fig. 3.14 a) and b). A schematic model of the C_{60} island structure on TiO_2(110)-1×1 surface is reported in Fig. 3.14 c). The (5×2) unit cell contains two C_{60} molecules. Because of steric repulsion, C_{60} in adjacent rows adsorbs either on top a 5f-Ti or on-bridge between two 5f-Ti. The nearest-neighbor distance between the molecules is measured to 9.85 Å, which is compatible with the Van der Waals diameter (47). This model together with the interpretation of STM images are in good agreement with the AFM results previously obtained by Loske et al. (48) even if the monolayer phase was erroneously interpreted in terms of a c(5×2) symmetry.

It is important to note that we could not resolve any structure within the molecules,

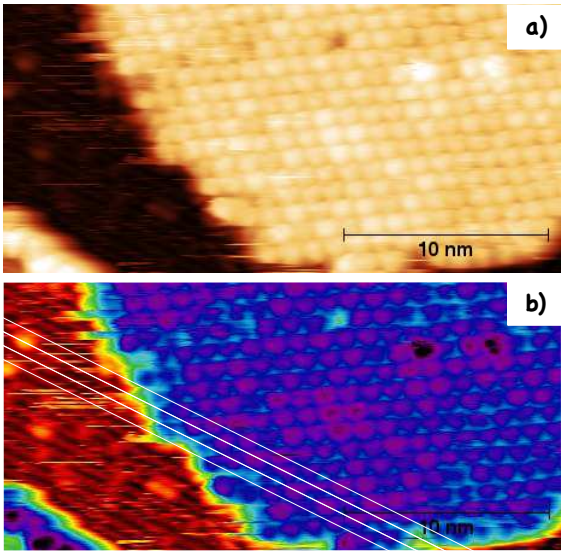

Figure 3.13: a) High resolution STM image of a closed-packed island where single C_{60} molecules appear as spherical features. b) For the same image a different color scale has been used to enhance the z contrast. White lines indicate the position of the 5f-Ti rows. As we can see C_{60} molecules are sitting on top of the 5f-Ti rows.

i.e. molecular orbitals, appearing as perfect spheres. This might be due to the fact that the molecules possess sufficient kinetic energy for rotating around their center or a fixed axis. Moreover, C_{60} molecules seem to diffuse quite fast on the surface since it is possible to observe them only on step edges or into islands. This findings suggest a very weak interaction with the substrate just templating the molecules in between the bridging oxygen rows.

This conclusion is supported by He diffraction measurements of the specular reflectivity during deposition and thermal desorption.

The left side of Fig. 3.15 shows the evolution of the specular intensity during C_{60} deposition at different substrate temperatures, ranging from 380 to 570 K. A small intensity decrease is recorded at 470 K and 570 K, due to the temporary accommodation of a few molecules on the surface in equilibrium with the molecular beam. The initial intensity is quickly recovered (C_{60} desorption) after stopping the evaporation. At lower temperatures, the specular intensity linearly drops to a minimum steady value without recovering by further deposition, indicating an increase of the disorder (either static or dynamic), as the surface is covered by C_{60}. In absence of a well defined oscillation

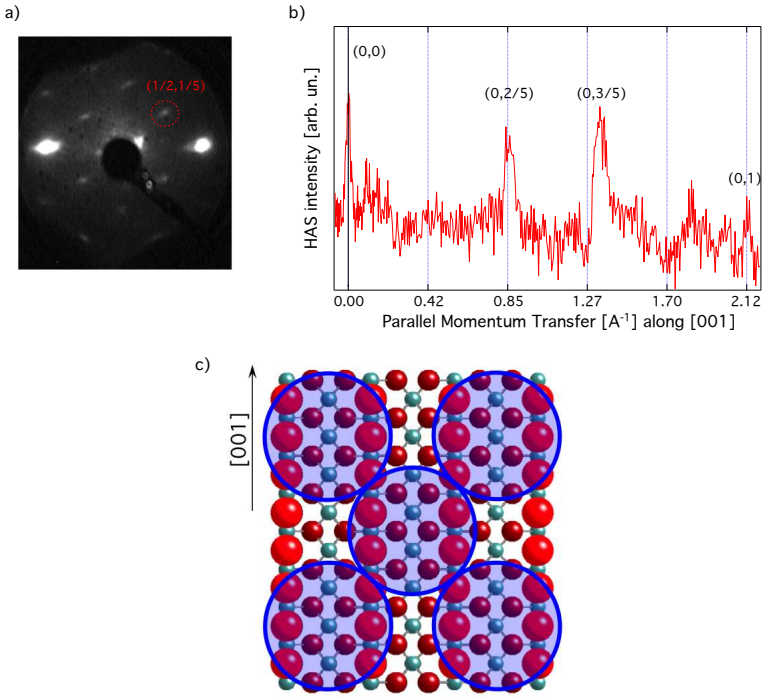

Figure 3.14: a) LEED pattern associated with 0.5 ML of C_{60} on the TiO_2(110)-1×1. The two big bright spots correspond to the substrate (1,0) and ($\bar{1}$0) beams while the bright small spots correspond to the super-periodicity associated with the molecules. This new periodicity is compatible with a p(5×2) structure. b) He atom diffraction scan of a C_{60} monolayer measured along the substrate [001] direction. After deposition at 420 K, two residual peaks of a quasi-five-fold periodicity are observed by cooling the sample down to RT. c) Model of the C_{60} island structure. Red and green balls correspond respectively to O and Ti atoms while C_{60} molecules are sketched with their van der Waals radii (blue circles). Molecules arrange in a p(5×2) superstructure with two nonequivalent C_{60} molecules in the cell.

of the reflectivity, we can assume that the completion of the first layer is achieved at the minimum of the reflectivity, where we have consistently detected the appearance of a few residual fractional peaks of the five-fold periodicity upon cooling the surface down to room temperature, see Fig. 3.14 b). This temperature-dependent behavior is indicative of a large molecular mobility, associated with both the surface migration and the molecular vibrations.

The study of the He specular reflectivity during the thermal desorption of two layers reveals that C_{60} desorbs completely above 600 K (50-60% of the intensity from a freshly clean substrate is recovered upon desorption), as it can be seen in Fig. 3.15 (right). By varying the heating rate from 0.25 to 1 K/sec, we have never detected any intermediate desorption feature (neither maxima or plateau), which might eventually allow us to discriminate between first and next layers desorption. Most importantly, the desorption temperature is more than 100 K higher than the maximum temperature of sticking. We may conclude that the C_{60} intermolecular attractive strength is significantly larger than the C_{60} to TiO_2 adhesion.

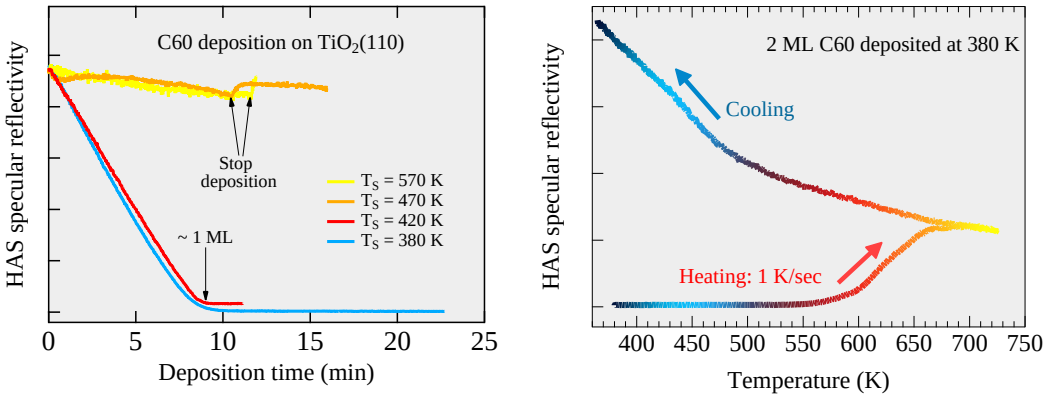

Figure 3.15: (Left) He atom specular intensity during C_{60} deposition at different substrate temperatures (T_S). (Right) He specular intensity taken during the thermal desorption (red arrow) and subsequent cooling (blue arrow) of a C_{60} film of about 2 ML, as obtained by C_{60} deposition T_S = 380 K (corresponding to the end of the deposition curve in the left figure).

3.3.2 Spectroscopic characterization: NEXAFS and XPD

For a better understanding of the molecular-surface interaction we have performed different spectroscopic experiments. The left side of Fig. 3.16 shows the C 1s NEXAFS spectra taken for a coverage of 0.8 ML, measured in two different geometries: one with the electric field of the incoming beam parallel to the surface (s-polarization) and the other perpendicular to it (p-polarization). The good match between the two spectra (no dichroism) suggests a negligible deformation of the molecules which preserve their spherical symmetry. Moreover both the shape and the energy position of the peaks are coincident with those obtained for a multilayer of C_{60} grown on Au (47)(right side of Fig. 3.16), confirming further that the unoccupied molecular orbitals have not been significantly altered upon surface deposition. These results indicate a very weak molecule-substrate interaction as anticipated by STM and HAS measurements.

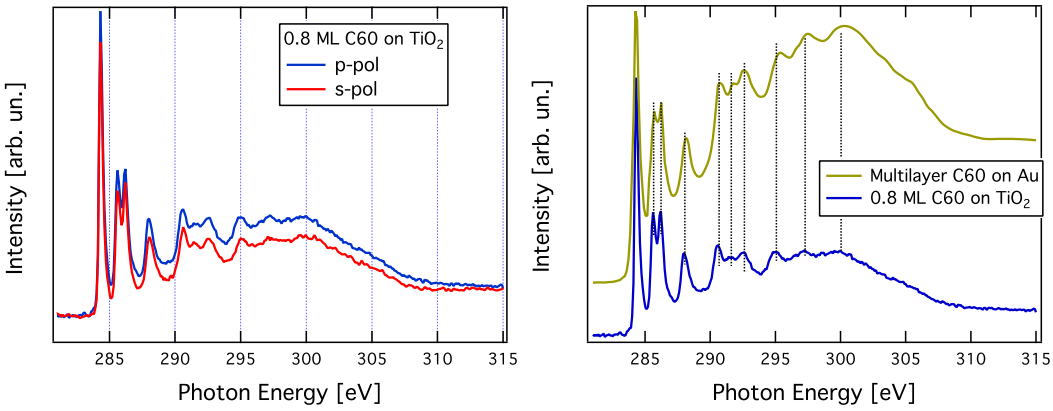

Figure 3.16: (Right) C K-edge NEXAFS spectra of 0.8 ML of C_{60} molecules, for two different polarizations. (Left) Comparision with the spectra of a C_{60} multilayer grown on Au.

As mentioned before we did not succeed in resolving atomic molecular orbitals in C_{60} island by STM. Each C_{60} displays a smooth hemispherical protrusion, suggesting that the C_{60} molecules are rotating freely at room temperature. This is very common for weakly interacting substrate, where the interaction with the molecules is not sufficiently strong to establish an orientational order. By cooling down the sample, it is possible to freeze, partially o completely, these molecular rotations. An example of this is reported for C_{60} molecules adsorbed on a self assembled monolayer of alkythiol (49). While a

RT C_{60} molecules do not show intramolecular contrast, already a 77 K they appear as a tilted doughnut, or an asymmetric dumb-bell, each being consistent with a rotating pattern around a fixed axis. At 5K, this molecular rotation is frozen and domains with two different orientations were observed.

Because of the non-conclusive interpretation of the STM images (i.e. tip artifacts, required resolution) we have performed X-ray Photoelectron Diffraction measurements, in order to extract information on the C_{60} cage orientation (50). When the surface is illuminated by X-rays, photoelectrons are emitted from each of the C_{60} carbon atoms and scattered from the surrounding ion cores 3.17 a). At electron energies above 500 eV, the strongly anisotropic scattering of photoelectrons leads to a forward focusing of electron flux along the emitter-scatterer directions, see Fig. 3.17 b). Fig. 3.17 c) shows the X-ray photoelectron diffraction pattern calculated for a C_{60} molecule facing the surface with a hexagon, as sketched in a) of the same figure. The photoelectron angular distribution is shown in stereographic projection and in a linear gray scale with the maximum intensity in white. The center of the plot corresponds to the surface normal and the outer circle represents grazing emission along the surface. As expected, the particular molecular orientation considered gives rise to a well-defined diffraction pattern characterized by a three-fold symmetry.

Fig. 3.18 shows the experimental XPD pattern for C_{60} on TiO_2(110)-1×1. It covers a polar angle going from 90° to 22° (θ=90° means normal emission) and an azimuthal range extending from 0° to 130°, including both the high symmetry surface direction, [001] and [1$\bar{1}$0]. Features in yellow correspond to more intense signal while those in black are associated to low intensity. The experimental XPD pattern is characterized by a small anisotropy with just one bright belt ranging from a polar angle of θ=52° to 72°. This result is quite far from that obtained in the example of Fig. 3.17, yet the occurrence of an anisotropy is indicative of the fact that the adsorption is not completely uncorrelated. Indeed the experimental diffraction pattern is consistent with two possible scenarios. The first possibility implies that all molecules are fixed on the surface with the same polar orientation but each one with a different azimuthal orientation. In this condition each molecule would contribute with a well defined pattern to the final one, having at the end the sum of thousands of different patterns each one rotated with respect to the others by a different amount around the surface normal, The second possibility is to have all molecules adsorbed with a specific polar geometry but rotating

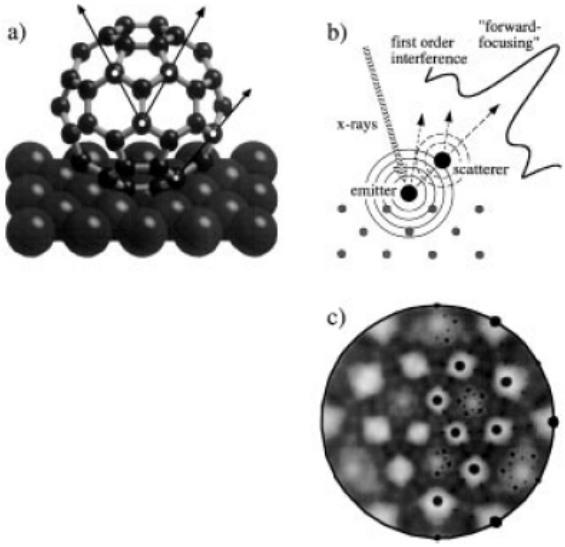

Figure 3.17: (a) Sketch of the scattering situation for a C_{60} molecule adsorbed on a single crystal surface. All the 60 carbon atoms of the molecule act as photoemitters, and the photoelectrons are scattered from the surrounding ion cores. (b) Because of the forward-focusing effect, intensity maxima are observed in directions corresponding to C-C interatomic directions. c) Stereographic projection of the XPD pattern calculated for a C_{60} molecule facing with a six-membered ring (6-ring) towards the surface, as sketched in a) (50).

along their surface normal (spinning). By this technique is not possible to discriminate between the two cases but the second one seems to be the more likely confirming the hypothesis inferred from the STM measurements.

According to the XPD measurement, there is a preferential orientation of the molecules on the substrate. In order to extract this information, some simulations of the diffraction pattern are required. By using the MSCD code (51), the diffraction pattern has been simulated for the 5 simplest high-symmetry orientations of C_{60}: fullerens adsorbed on one single atom (named atom 566), on a hexagon, on a pentagon, on an hexagon-hexagon dimer (named dimer66) or on a pentagon-hexagon dimer (named dimer56).

Fig. 3.19 shows the simulated XPD diffraction patterns for the different adsorption geometries with the experimental data. In this case, the patterns are represented in their matrix format, which simplifies the comparison process. In this format, the diffraction anisotropy is presented versus the polar (vertical axis) and the azimuthal

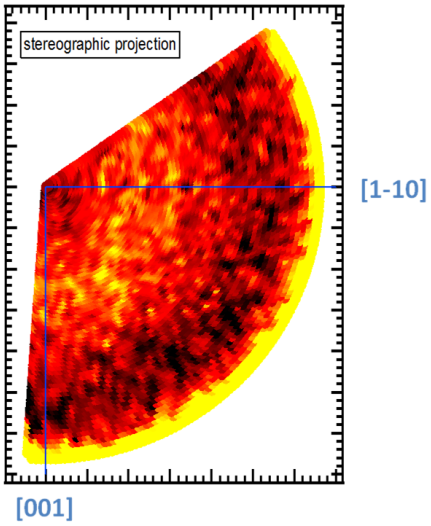

Figure 3.18: Experimental XPD pattern of the C 1s core level. We can distinguish a bright belt going from 52° to 72°. The center corresponds to normal emission. The kinetic energy of the emitted photoelectrons is 850 eV

angles (horizontal axis). The upper part of the patterns corresponds to normal emission (θ=90° for the experiment and θ=0° for the simulations). Among the five orientations, dimer66 and pentagon can be automatically rejected as they present maxima at polar angles where the experiment presents minima. Among the three remaining ones, we can also discard the atom566 as, although the main maxima are located within the belt, it presents another maximum at normal emission. On the other hand, both hexagon and dimer56 configurations present their maxima almost completely within the belt. Furthermore, their maxima appear at nearly complementary polar angles so that a combination of both orientations almost covers the entire belt. In this way, a different orientation for the ground state of the two molecules composing the superstructure unit cell is observed. This result is not surprising if it is taken into account that the adsorption site relative to the substrate could be different for the two molecules, as they are adsorbed on different sites of the surface unit cell, see Fig. 3.14 c).

The overall agreement is good, except for the region located around a polar angle of 40° - 50° (considering the experimental scale) where the dimer56 orientation presents a maximum. This wrong prediction can be understood if we take into account that only the five simplest orientations have been considered in the simulations. Probably, the

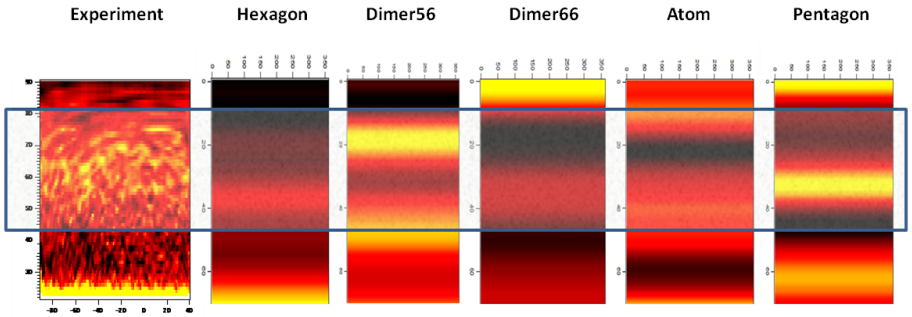

Figure 3.19: Experimental and simulated XPD patterns represented in their matrix format. The main five orientations for C_{60} have been simulated. The bright belt is enclosed in a transparent blue rectangle. The vertical axis corresponds to the polar angle while the horizontal one is the azimuthal angle. Only two orientations, properly combined, fit the experimental data: hexagon and pentagon-hexagon dimer (dimer56)

real orientation of the molecules is more complex. It is quite possible that C_{60} molecules are slightly tilted with respect to the ones considered here. For example, a better fit is obtained for an orientation where one of the molecules is slightly rotated with respect to a dimer56 towards a pentagon orientation. This small rotation improves the agreement between the experiment and our model. The number of possible parameters and the weak experimental anisotropy makes a more quantitative study of the XPD curves unrealistic and other complementary techniques have to be used for a final elucidation of the structure.

3.3.3 Theoretical investigations

In order to have a quantitative evaluation of the possible orientations considered in XPD simulations, an exhaustive DFT study including van der Waals interactions has been performed. The best-result of such a study is given in Fig.3.20.

As we can see from Fig. 3.20 a) the molecule on top of a 5f-Ti atom presents a quasi pentagon-hexagon dimer orientation (C_{60} molecules at the corner of the lattice unit cell), slightly rotated (5 deg.) towards a pentagon orientation. On the other hand, the molecule in between two 5f-Ti atoms presents a hexagon orientation with two Ti atoms in the center of the hexagon borders. We can also notice that both molecules are located in between the bridging oxygen rows, in good agreement with the STM observations.

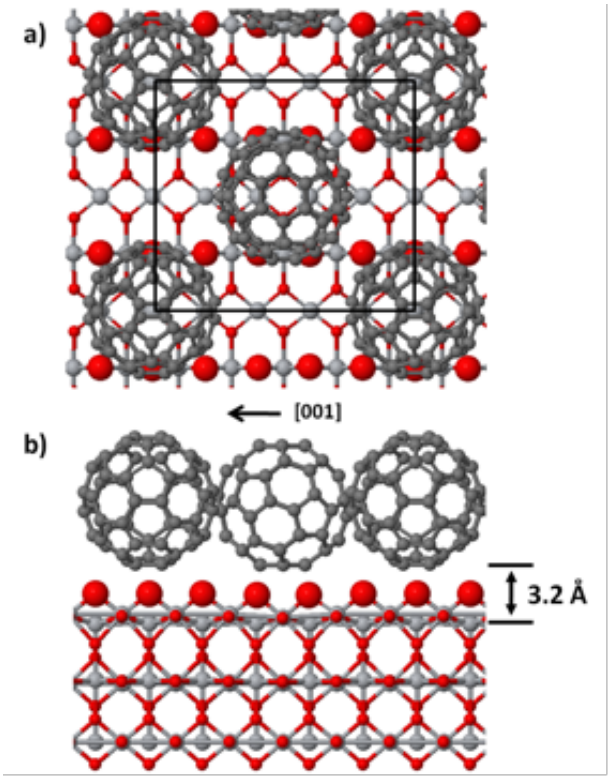

Figure 3.20: a) Top and b) side view of the C_{60}/TiO_2 model obtained by DFT optimizations.

Fig. 3.20 b) shows a side view of the system, along the [001] direction. We observe that both molecules are separated from the surface plane determined by the 5f-Ti atoms approximately of the same distance (3.2 Å). The C-O distance between the closest atoms is 2.8 Å, much larger than the typical bond length of approximately 1.1-1.2 Åfor CO and CO_2. All these facts indicate that the C_{60} molecules present a weak interaction with the TiO_2 surface and they suggest a floating organic layer on the TiO2 surface. Interestingly, in STM images, as that shown in fig. 3.13 b), the apparent height of the molecules is not always the same, i.e., each imaged molecule has a specific height. That could be related to the interaction of the STM tip with the floating fullerenes, which are slightly pushed by the scanning tip.

Until now, we have seen that the C_{60} organic overlayer is adsorbed at a relatively large distance, confined in between the bridging O rows and spinning on the surface. However, we have not addressed the possible mechanism accounting for the revolution model. We can rationalize the molecular spinning performing molecular dynamics simulations for two C_{60} molecules adsorbed on TiO2(110)-(5x2). These calculations are very expensive from a computational point of view. Therefore, we abandon here the ab-initio approach and describe the interactions in the system by a classical force field based in condensed phase optimized potentials for atomistic simulation studies (COMPASS) (52)(53).

These simulations show that at low temperatures (between 150 and 300 K) mainly breathing modes in the molecules are populated, while above room temperature molecules start rotating at typical angular frequencies of about 0.1 rad/ps. These rotations can be classified in two types: (i) random rotations of the whole molecule where barriers for rotations are in the same order of magnitude as kT, and (ii) correlated rotations where the total angular momentum of two neighboring molecules is conserved. These are associated to the off-axis interaction between two molecules moving on different troughs in the p(5x2) reconstruction. It operates similarly as in two billiard balls suffering an off-axis collision and getting some angular momentum as a consequence. In a typical simulation (two snapshots are shown in Fig. 3.21) we observe C_{60} molecules rotating around the surface normal, as it has been predicted by considerations based on XPD experiments.

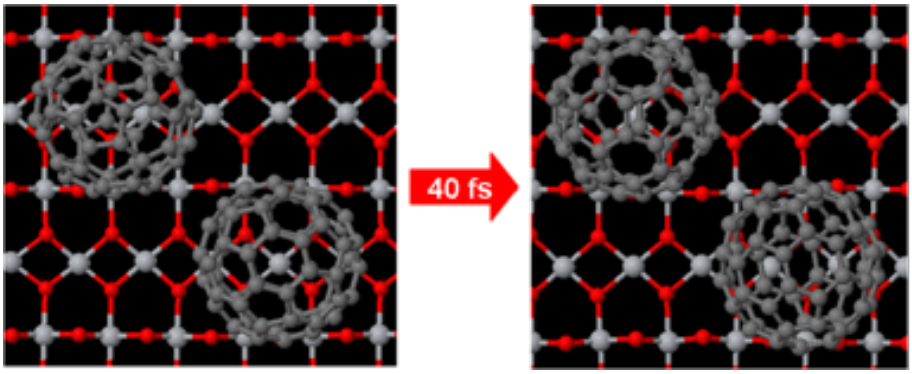

Figure 3.21: Ball-and-stick schematic representations of two snapshots obtained by molecular dynamics simulation. In these two snapshots from a video (www.icmm.csic.es/esisna) we can observe how the azimuthal orientation of the C_{60} molecules is changing, thus indicating a rotation along the surface normal.

3.4 Pentacene

Pentacene belongs to the family of Polycyclic Aromatic Hydrocarbons (PAHs). It is composed by five fused benzene rings for a total of 22 carbon atoms surrounded by 14 hydrogen atoms (see Fig. 3.1). Pentacene crystals and thin films behave as p-type organic semiconductor. They have been successfully tested in the assembly of high charge mobility thin film transistors (OTFT) and organic photovoltaic cells (54, 55, 56, 57). Pentacene single-crystals grow in a triclinic lattice where molecules adopt a herring-bone packing with two molecules per unit cell (58). Usually the growth proceeds along the **c** axis by stacking of layers, where the molecules are oriented almost vertically with respect to the plane of growth. Lying down pentacene structures have been reported for the first layer when deposited on metal surfaces (59), although molecules tend to stand up from the second layer (60). On semiconductors or insulating materials the molecules grow in a standing-up geometry since the initial stage of deposition as the assembling is driven by van der Waals molecular interaction (59).

In this section the interaction of pentacene molecules with the unreconstructed TiO_2(110) surface has been characterized by means of HAS, STM and NEXFAS spectroscopy.

3.4.1 Film structure determination by HAS and STM

The structural characterization of pentacene films was investigated independently by HAS and STM experiments.

In HAS experiments the evolution of the specular intensity is followed during the pentacene deposition performed at different substrate temperatures, ranging from 300 to 410 K, see Fig. 3.22. At 300 K, the intensity of the HAS specular intensity rapidly decreases due to increasing surface roughness. For a coverage of approximately 0.7 ML the surface reflectivity starts to improve, indicating the occurrence of ordering between the uncorrelated molecules. The reflectivity increases until it reaches a maximum, corresponding to the completion of the first layer (1ML). Beyond the monolayer maximum the reflectivity rapidly vanishes without the appearance of any other oscillation. At a substrate temperature of 350 K we have found an improvement of the structural quality of the monolayer (see plateau before maximum), but further deposition simply leads, again, to a gradual vanishing of the reflectivity. Finally the monolayer phase is found to correspond to the saturation coverage at Ts= 410 K. In fact, after a small intensity decrease beyond the monolayer maximum, the reflectivity soon reaches a steady intensity. By stopping of the deposition at constant substrate temperature, the reflectivity quickly recovers the intensity of the monolayer phase. As a consequence, no second-layer molecules can be accommodated at 410 K on the monolayer phase, in full agreement with previous findings for the pentacene phases on the Au(110) surface (61).

The surface morphology was more thoroughly studied by taking consecutive diffraction patterns during deposition. The evolution of the pentacene film structure was monitored at the substrate temperature of 300 K by taking scans along the [001] surface direction, which corresponds to the ΓY direction in reciprocal space. A representative set of diffraction scans is shown in Fig. 3.23. The scans are vertically displaced by a linear offset, according to the increasing coverage. The bottom scan is taken at the nominal coverage of 0.45 ML and the topmost one at 1.5 ML. Each angular scan is recorded in about 1.5 min, corresponding to the deposition of about 0.08 ML. On the right, a vertical dotted line marks the position of the (0,0) reflection; an additional vertical dotted line is traced on the left, marking the nominal position of a fractional peak with sixfold periodicity.

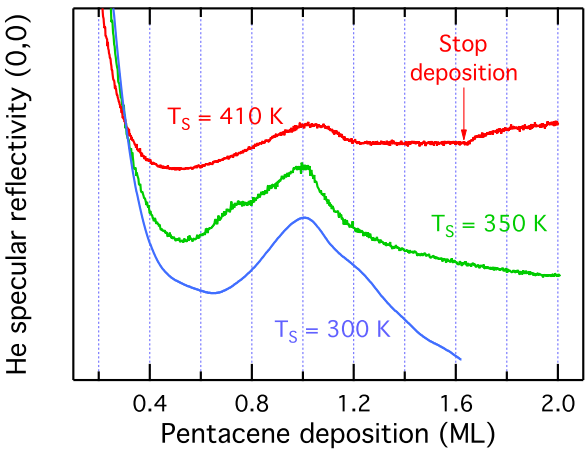

Figure 3.22: Intensity of HAS specular reflectivity (0,0) during deposition at different substrate temperatures.

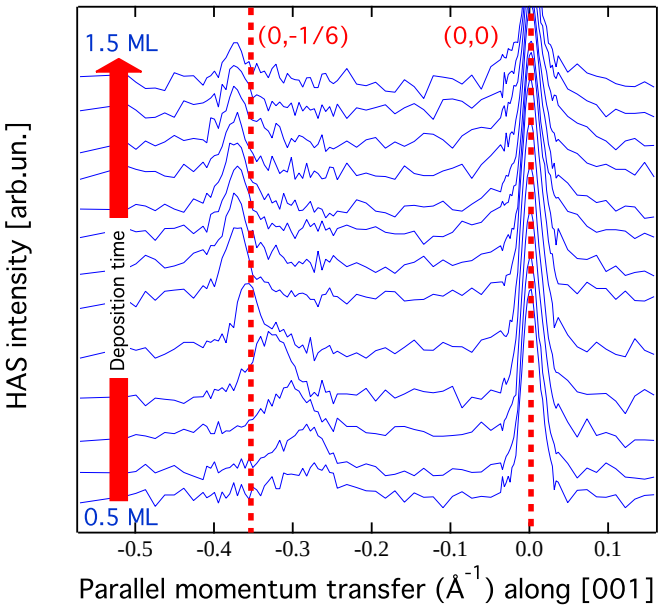

Figure 3.23: Consecutive HAS diffraction scans taken along the [001] direction during pentacene depostion with the substarte at RT.

Initially (not shown) the intensity of the specularly reflected (0,0) peak decreases steeply without broadening, thus indicating the gradual covering of the substrate by uncorrelated molecules. Close to the specular peak, a new incommensurate diffraction feature is formed at about 0.5 ML, which grows in intensity and gradually shifts away from the (0,0) reflection up to a steady angular position. Further deposition simply decreases the overall intensity of the diffraction pattern. Only when the angular position of the new diffraction peak corresponds to the (0, 1/6) fractional peak we have observed the emergence of weak second order peaks of the same six-fold periodicity; at different deposition stages, the new diffraction feature only displays a single diffraction order aside the substrate Bragg peaks (0,0), (0, ±1). This means that single uncorrelated molecular patches start to join with the occurrence of a preferred (most probable) spacing, rather than the establishment of a true periodicity.

A quantitative analysis of the evolution diffraction pattern is shown in Fig. 3.24. The new diffraction feature (filled circles) appears in correspondence of the shallow minimum of the (0,0) reflectivity (open squares), and its intensity displays a maximum corresponding to the maximum of (0,0) reflectivity. The mean spacing associated with the new peak is shown in the upper plot (in red), where the steady value of 16.9 Å is reached at the intensity maximum of the new peak. Since this value matches the long side of the molecule (∼15.5 Å) we can support the hypothesis of a molecular head-to-head alignment along the [001] direction. The continuous variation of the pentacene spacing from 24 to 16.9 Å, beyond the commensurate six-fold periodicity (17.7 Å), leads to the conclusion that the intermolecular interaction along the [001] direction is repulsive. As long as the molecular density is low, pentacene molecules prefer to stay far away from each other. These findings are also confirmed by the STM measurements.

On the left side of Fig. 3.25, STM images are shown for the submonolayer range, where the monolayer has been defined as the coverage corresponding to the most dense first layer. At each coverage we can recognize irregular stripes running along the $[1\bar{1}0]$ direction. Within a single stripe we can distinguish small parallel segments perfectly aligned along the [001] direction. Each of these segments can be assigned to individual lying-down pentacene molecules, because their measured length (∼16 Å) fits the expected value for pentacene molecule. Passing from 0.5 to 0.9 ML we can observe a straightening of the stripes and a decrease of the spacing between them, in perfect agreement with the HAS experiments (pentacene peak shift along the [001] direction).

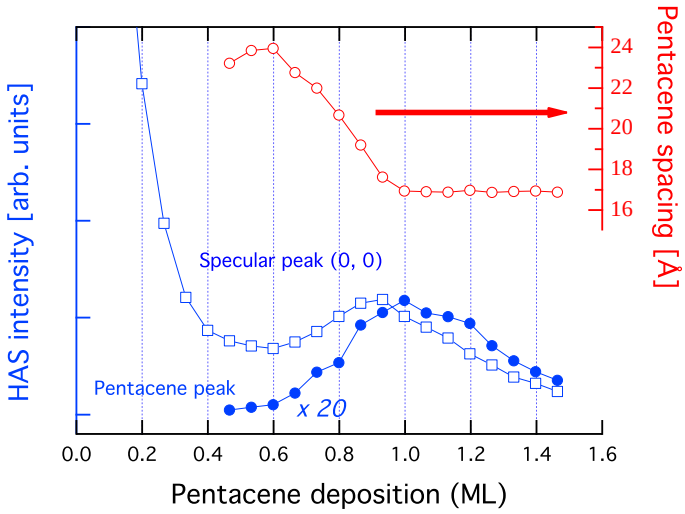

Figure 3.24: On the left axis of the graph the HAS intensity evolution of the specular and pentacene peak is shown as a function of the deposition. The corresponding pentacene spacing is shown in the top right axis.

On the contrary pentacene stripes always display the same side-by-side spacing along the $[1\bar{1}0]$ direction that corresponds to the substrate spacing between the oxygen rows (6.5 Å). At the same time no additional periodicity can be detected along the $[1\bar{1}0]$ direction by He atom diffraction experiments.

Pentacene growth thus proceeds via an interplay of two main interactions: the intermolecular side-by-side attraction that drives the formation of continuous stripes and the intermolecular head-to-head repulsion that tends to maximize the stripe separation. On the other hand the substrate corrugation due to the oxygen rows dictates the azimuthal orientation of pentacene along the [001] direction.

The monolayer phase yields a molecular density of 0.91 ± 0.01 molecule nm^{-1}. This value is larger than the density of the monolayer phase on Cu(110) which is already know to allow the growth of a few additional lying-down layers (62). Although there is no evidence of the formation of a second ordered layer by HAS measurements (maybe due to the enhanced molecular vibrations), STM images show a second layer of pentacene molecules whose structure resembles the one obtained for 1ML (Fig. 3.26, left). It preserves the striped morphology and intermolecular spacing along the $[1\bar{1}0]$ direction. The main difference is the appearance of molecular vacancy islands, which are of one

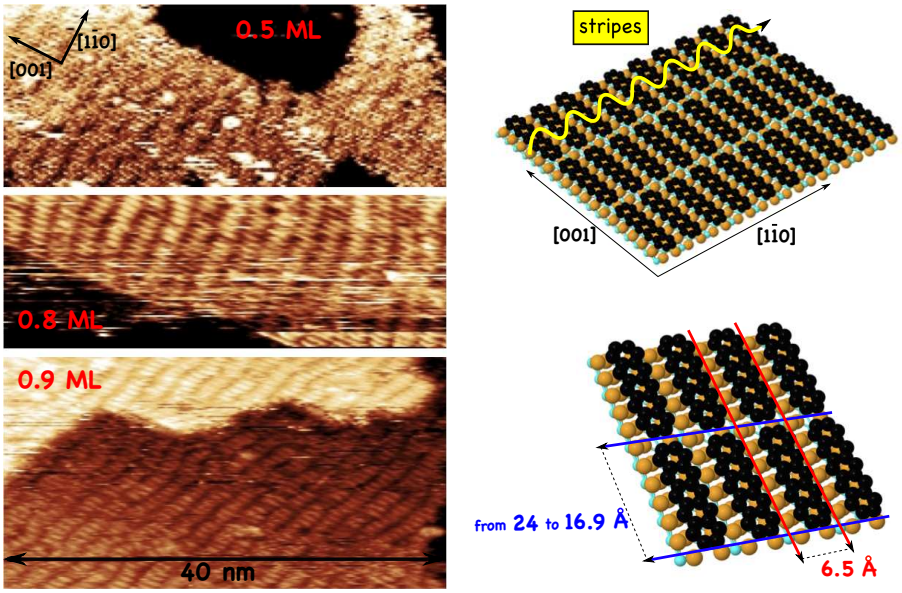

Figure 3.25: (Left) Set of STM images for three different coverages: 0.5 ML, 0.8 ML and 0.9 ML. By increasing of coverage, we observe a straightening of the pentacene stripes oriented along the [1$\bar{1}$0] direction together with a decrease of the inter-stripes spacing. (Right) Schematic representation of the pentacene arrangement on TiO_2 surface.

single molecule width and extend along the molecular stripes. All these results suggest a relatively strong intermolecular attraction both side by side and with the molecules underneath which is able to overcome the repulsive head-to-head interaction. If we increase the coverage up to the third layer, we observe that molecules start losing the striped morphology growing in squared irregular patches, even if molecule preserve a certain degree of vertical coherence with the monolayer phase, (Fig. 3.26, right). A better understanding of the growth mechanism beyond the monolayer phase is coming from the information obtained by NEXAFS.

3.4.2 Molecular orientation study from NEXAFS

As discussed in chapter 2.3.2, NEXAFS measurements are most helpful in determining the molecular orientation with respect to the surface plane. By tuning the photon energy across specific absorption edge, one excites the electrons of a chosen atomic species into the unoccupied molecular orbitals. The NEXAFS measurements of the de-excitation signal effectively maps the unoccupied molecular states. The absorption

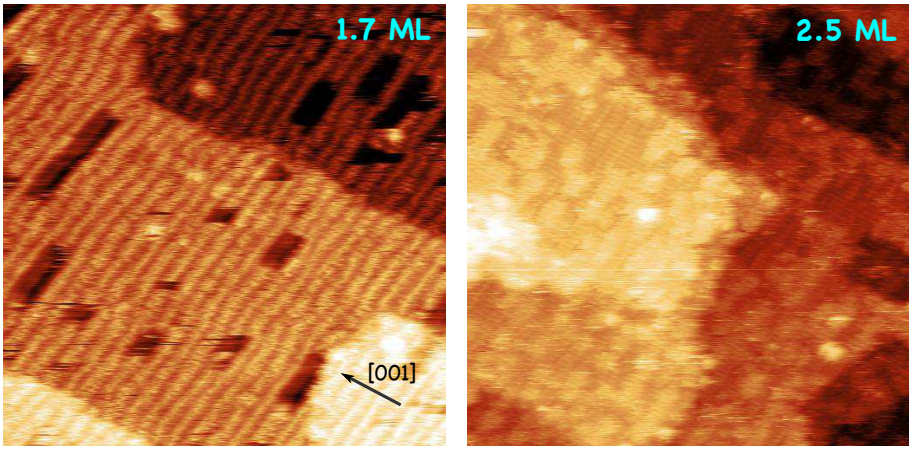

Figure 3.26: STM images for 1.7 ML and 2.5 ML. By comparing the two coverge, we can notice a variation in the growth mode passing from straight stripes to squared irregular patches. Size (for both images): 50×50 Å.

signal is measured as an electron yield, collected by the wide angle channeltron detector, placed above the illuminated sample. The grid in front of the channeltron was polarized at -230 V in order to reject the low energy electrons and collect the Auger decay electrons at most. This way partial yield was measured with a high-pass filter, which is known to increase surface sensitivity of the absorption measurements. The acquired NEXAFS spectra were appropriately normalized to exclude all possible artifacts. The normalization process corrects for both the beam current variations in the storage ring and the photon flux decrease due to contamination of the beamline monochromator. The photon energy is calibrated with a precision of 0.01 eV thanks to the carbon adsorption feature in the I_0 reference (drain) current. The latter has been calibrated by simultaneous acquisition of the C1s $\rightarrow \pi^*$ gas phase transition of CO (22). All NEXAFS spectra presented in this thesis were treated according to the described procedure.

Fig. 3.27 shows the NEXAFS spectrum of the monolayer phase grown at 300 K. It exhibits most of the features that will be met later in this chapter and it was therefore chosen to present them. A good agreement with the pentacene gas-phase NEXAFS spectra can generally be noted, with some variations in the relative intensity of the resonances. At low photon energies two peaks occur at 284 and 285.8 eV, respectively, belonging to the C 1s $\rightarrow$ LUMO and LUMO+1 transition. In the high-energy part of the spectrum, at 294 and 301 eV two broad features are observed. They are both

located above the ionization potential which makes them transitions to quasi-bound σ^* molecular states.

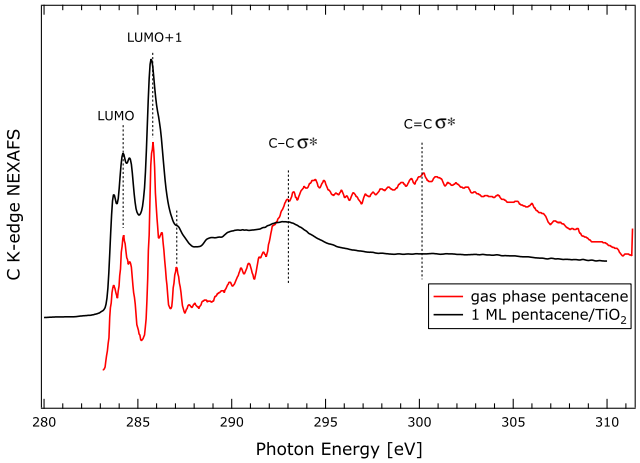

Figure 3.27: Comparison between the C K-edge NEXAFS of the pentacene monolayer phase on TiO_2 and that obtained for the molecule in gas phase. [alagia].

The multicomponent nature of the π^* resonances originates from nonequivalent C 1s initial states due to 6 nonequivalent carbon atoms within the pentacene molecule, see Fig. 3.28 a). The theoretically predicted energy positions of the transitions from the individual C 1s states are denoted by vertical bars on Fig. 3.28 b) (63). Fig. 3.28 c) shows the perfect matching of the LUMOs fine structure between the pentacene monolayer phase and the isolated molecule, indicating that pentacene preserves its molecular character without being perturbed by the interaction with the substrate. This confirms the findings obtained by STM and HAS, where the intermolecular forces seem to dominate on the molecule-to-substrate interactions, which simply drive the azimuthal orientation of the molecules. Being familiar with the typical features of pentacene NEXAFS spectrum, we can now observe how they depend on the surface structure and the orientation of the X-ray electric field vector.

3.4.2.1 NEXAFS angular dependence of the monolayer phase

The principle underlying the dependence of the resonance intensities on the orientation of the X-ray electric field vector (**E**) is quite simple: the resonance intensity associated with a specific molecular orbital final state is largest if **E** points in the direction of that

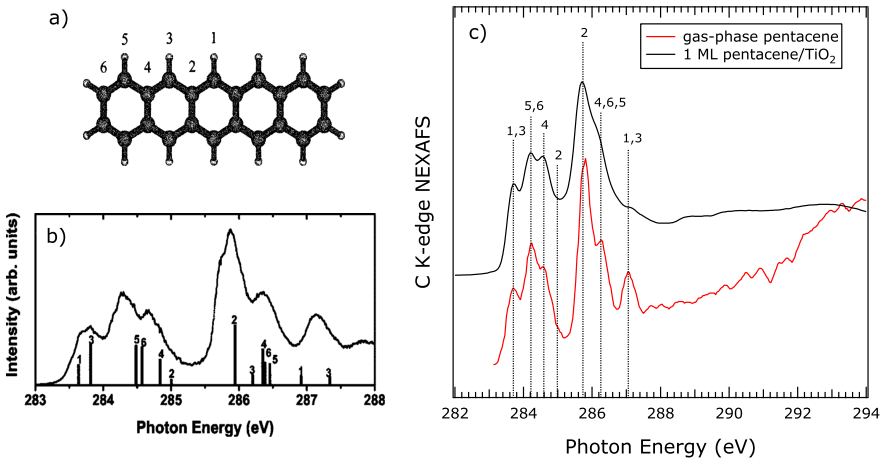

Figure 3.28: b) Calculated and measured positions of the C 1s → LUMO and LUMO+1 resonances from six chemically nonequivalent carbon atoms, shown in a). Above the bars there is the experimental NEXAFS spectrum of pentacene gas-phase (63). (Right) Perfect matching of the LUMOs fine structure between the isolated molecule (gas phase) and 1 ML of Pentacene on TiO_2.

molecular orbital, and the intensity vanishes if **E** is perpendicular to the direction of the orbital, i.e. lies in the nodal plane of the orbital.

In Fig. 3.29 the application of this principle to our case is shown. Both STM and HAS measurements are concurrent in indicating the lying-down adsorption geometry of pentacene on TiO_2 . In the case of a completely flat geometry (as reported in the picture), the intensity associated with a π^* orbital will vanishes, when passing from p-polarization (**E**⊥surface) to s-polarization (**E**∥surface). The opposite situation is expected for σ^* orbitals. If the molecule is slightly tilted a residual intensity will be detected. In this latter case an additional dichroism (s-pol: $\mathbf{E}\|[1\bar{1}0] \rightarrow \mathbf{E}\|[001]$) can be also detected due to the azimuthal ordering of the pentacene phases.

Fig. 3.30 shows the results obtained for the monolayer phase. By comparing the spectra taken with the photon beam along the [001] direction, one notice the strong intensity decrease of the π^* resonances (LUMO and LUMO+1), when passing from p- to s-polarization. However, a residual intensity is still observed indicating that molecules are adsorbed with a small tilt angle with respect to the surface. An opposite dichroism is also detected for the σ^* molecular states.

By fitting the NEXAFS spectra, a quantitative evaluation of the molecular tilt angle

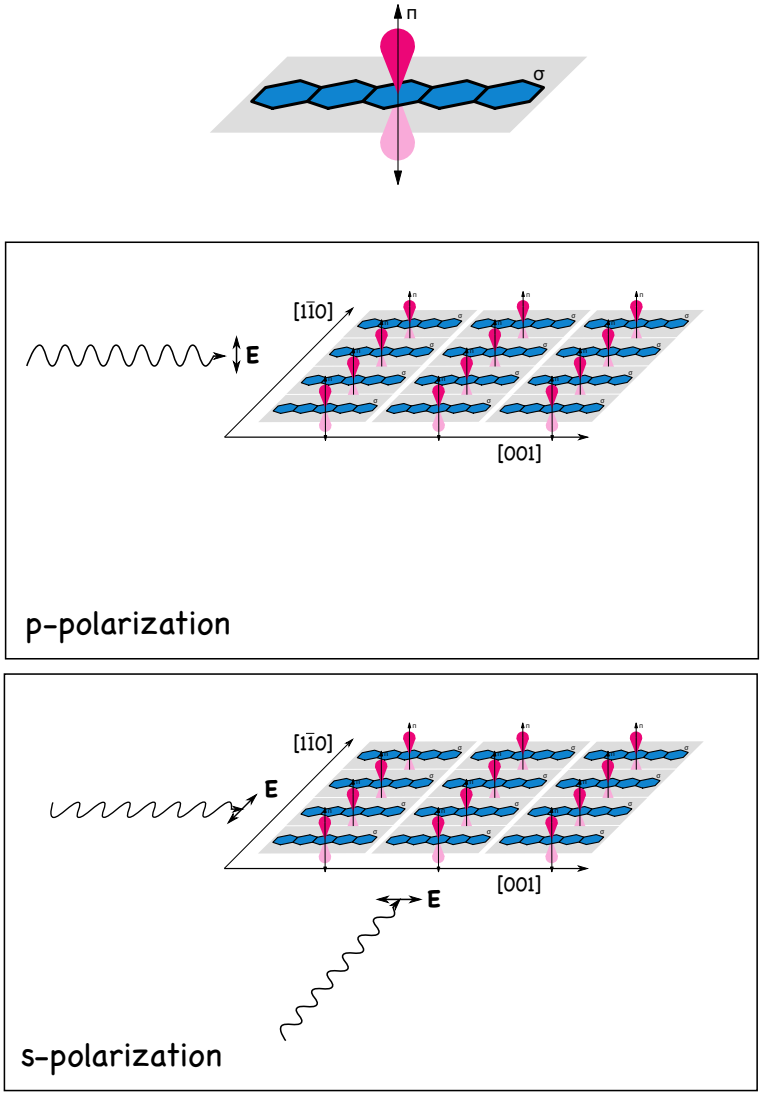

Figure 3.29: Schematic of the different scattering geometries used in the NEXAFS measurements. The electric field vector **E** is perpendicular to the surface in the p-polarization an parallel in the s-polarization. In the latter case it is also possible to change the azimuth in order to align **E** along the chosen symmetry direction.

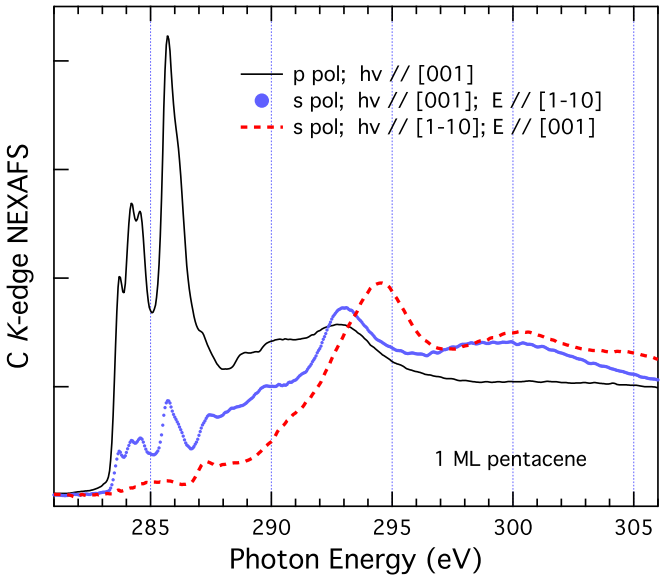

Figure 3.30: NEXAFS taken at the C-kedge in the monolayer phase for two opposite orientations of the surface with respect to the X-ray polarization (p and s polarization), and for two different azimuthal orientations in s-pol. See Fig. 3.29 for the geometry of the measurements.

γ can be obtained from the LUMO intensity dependence on the polarization angle θ (θ=90° p-pol, θ=0° s-pol). For a π-plane transition symmetry and twofold surface symmetry, the ratio between the two opposite polarizations I_s/I_p is proportional to $\tan^2\gamma$ (16); thus we obtain a molecular tilt angle of γ=25° ± 2°. This angle is associated with a rotation of pentacene around its long axis, as quantitatively confirmed by the comparison of the NEXAFS spectra taken in s-polarization for different azimuthal orientations of the surface, where an additional dichroism is detected. As it can be seen, the residual intensity of the π^* resonances observed when the beam is oriented along the [001] direction ($\mathbf{E}\|[1\bar{1}0]$), practically vanishes when the surface azimuth is rotated by 90°, bringing the photon beam along the $[1\bar{1}0]$ direction ($\mathbf{E}\|[001]$). In this case, the absence of π^* resonances implies that the molecular plane is perfectly parallel to the electric field, when the latter is oriented along the [001] direction.

Although the NEXAFS spectrum taken in p-polarization shows a clear correspondence with that in gas phase (see Fig. 3.27), additional spectral features appears at 288.8 and 290 eV. These features are typically observed in thick pentacene films. Thus, the full development of these peaks can be regarded as the resultant of the intermolecular interaction which occour in the typical herringbone packing of pentacene thick films. As a matter of fact, the full bulk-like development of these electronic states may be detected at the monolayer phase only for homeotropic (standing-up) orientation (64)(65), but, so far, it has never been reported for a lying down phase, where molecule-to-substrate interactions typically dominate over intermolecular interaction. On the contrary, the present weak interaction with the substrate together with the strong side by side attraction and molecular tilting yield an attraction between adjacent pentacene molecules that is strong enough to fully develop a bulk-like electronic structure along the stripes, although in a lying-down monolayer phase.

3.4.2.2 NEXAFS angular dependence of the multilayer phase

From the latter structural information (molecular tilt angle) it is possible to appreciate, now, the good match between the structure of the monolayer phase and that of the bulk $a-c$ crystal plane (see Fig. 3.31). In fact, the lateral coupling of the molecules along the substrate $[1\bar{1}0]$ direction mimics well the herringbone structure observed along the a crystal axis, both for the tilt angle and pentacene spacing (58). On the other hand the head-to-head spacing along the substrate [001] direction is ∼8% larger than

the $d_{[001]}$ pentacene crystal periodicity. All this facts are responsible of the growth of a few additional lying-down layers as confirmed by STM (Fig. 3.26) and NEXAFS measurements (Fig. 3.32).

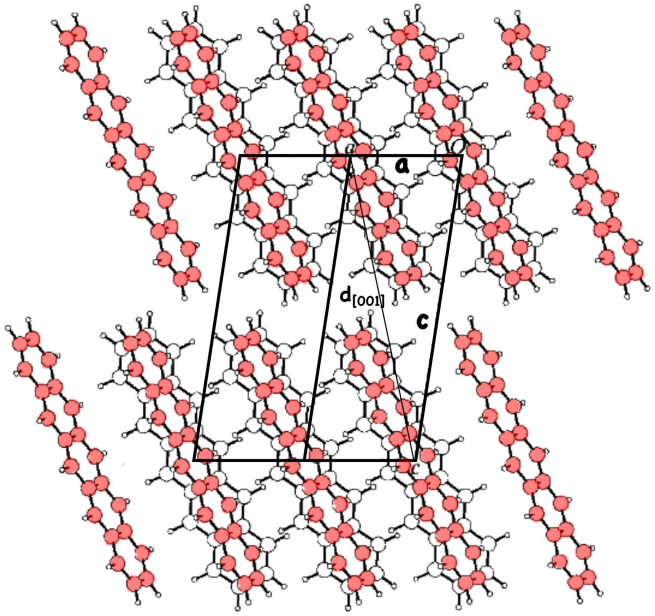

Figure 3.31: Pentacene a-c crystal plane. Lattice paramenters: a= 6.49 Å, c=14.75, β= 85.72° (58).

At 3 ML, the NEXAFS spectra preserve the same dichroic behavior of the monolayer phase. The overall tilt angle increase to 30° that is still compatible with the herringbone bulk packing. Even if we still observe a strong azimuthal dichroism in s-polarization, the NEXAFS spectra display a residual π^*-LUMO intensity when the electric field is oriented along the [001] direction. We attribute this intensity to lying-down molecules that have slightly changed their azimuthal orientation, rather than to uncorrelated clusters of standing-up molecules. In fact even if the lateral coupling of the molecules mimics well the herringbone structure along the a-axis, the molecules stacked along the c-axis are tilted with respect to the a-b plane. Thus, apart from the 8% spacing mismatch, the perfect head-to-head azimuthal orientation along the substrate [001] direction is not compatible with the pentacene bulk packing along the c-axis, and some azimuthal reorientation of the molecules must take place as soon as the herringbone stacking developes. This is also confirmed by the early fragmentation of the third layer

by STM (Fig. 3.26, right).

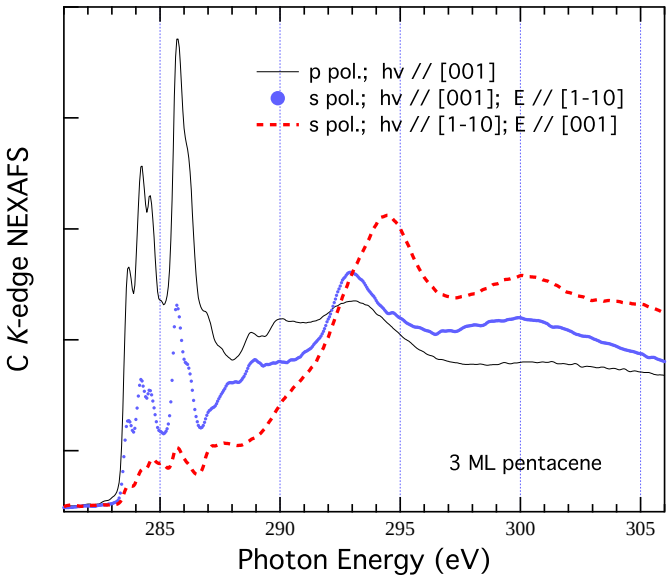

Figure 3.32: NEXAFS taken at the C-kedge for $\sim$ 3 ML film. Same polarization conditions of Fig 3.29.

3.5 PTCDI

PTCDI is obtained by attaching one imide functional group (-CO-NH-CO-) at each side of the perylene molecule (see Fig. 3.1). The effect of derivatization, i.e. adding electron withdrawing groups to the perylene core, results in a charge depletion of the inner aromatic rings making the molecule to behave as an acceptor of electrons. Consequently PTCDI and its functionalized derivatives are largely used in organic donor/acceptor heterojunction photovoltaic devices (66, 67, 68). In spite of the growing effort made to exploit PTCDI in high efficiency devices (69), experimental studies of its interaction with metals (70) and semiconductors (71) are very scarse.

In this section we report on the HAS, UPS, XPS, RESPES and NEXAFS experiments on the PTCDI/TiO_2(110)-1×1 system.

3.5.1 HAS characterization

The ordering of the PTCDI monolayer was also investigated by HAS diffraction.

The evolution of the He atom specular intensity has been monitored during PTCDI deposition by keeping the sample at controlled temperatures (see Fig. 3.33). At 300 K the reflectivity exponentially decays reaching the background value without the occurrence of any oscillation. A slightly different situation is found at 380 and 420 K. In these cases a weak oscillation occurs as soon as the background value is reached (1 ML). This means that higher substrate temperatures promote the ordering of the molecules but their vibrational component becomes so large that the appearance of a well defined maximum is smeared by Debye-Waller attenuation.

In correspondence of 1 ML a new diffraction peak has been detected along the [001] direction (see Fig. 3.34). It belong to a 5-fold periodicity, as it is possible to see by comparing the diffraction pattern of the PTCDI monolayer phase with that of the clean substrate (guidelines of five order peaks are displayed). The spacing associated with this periodicity (14.8 Å) is compatible with the long side of PTCDI (14.2 Å) and suggests that molecules are aligned head-to-head along the [001] direction. Again, like in the pentacene case, the substrate corrugation drives the azimuthal orientation of the molecules.

Although not all the 5-fold diffracted peaks are well developed in the HAS measurements, the commensurate periodicity of the PTCDI film is also observed by RHEED

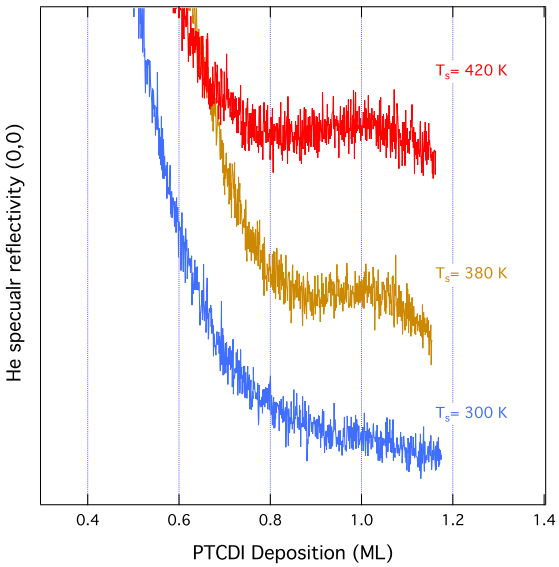

Figure 3.33: Intensity of the HAS specular reflectivity (0,0) during deposition at different substrate temperatures.

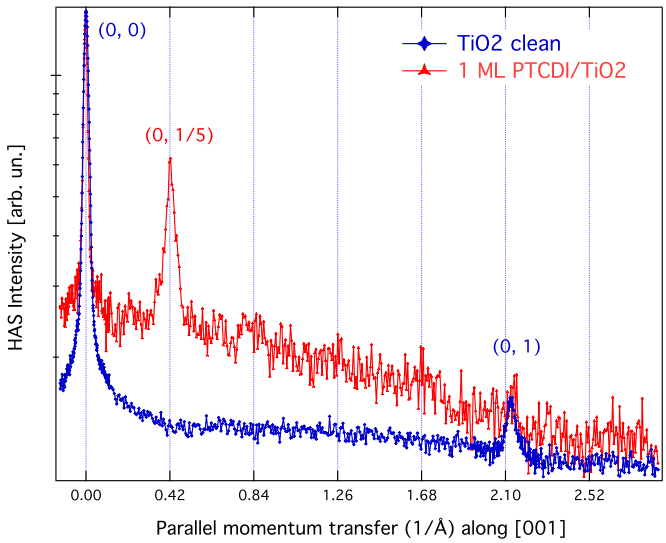

Figure 3.34: HAS diffraction scans taken along the [001] direction for the clean substrate and 1 ML of PTCDI. The PTCDI film shows a peak corresponding to a 5-fold periodicity.

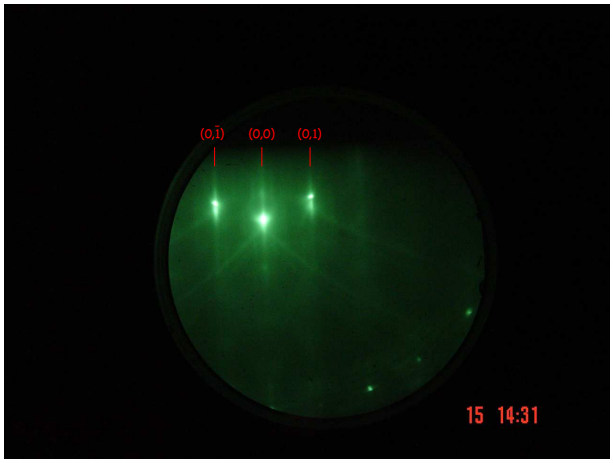

Figure 3.35: RHEED diffraction pattern along the [001] direction for 1 ML of PTCDI on the TiO_2(110) surface. Aside the substrate (0,0) and (0,±1) Bragg peaks some stripes of a 5-fold periodicity can be observed.

experiments. Fig. 3.35 shows the RHEED diffraction pattern associated with 1 ML of PTCDI. Aside the substrate (0,0) and (0,±1) Bragg peaks, more than one streak of a 5-fold periodicity can be observed. Moreover the He diffraction pattern has been repeatedly checked in subsequent deposition steps (within the oscillation) and a five-fold periodicity has always been detected, in opposition with what found in the case of pentacene. This findings suggest the establishment of a different kind of interactions in the two systems. The shift of the pentacene peak, beyond the 6-fold periodicity, reflects a real movement of the molecules along the [001] direction indicating a very weak molecule-to-substrate interaction. On the other hand the interaction between PTCDI molecules and the TiO_2 surface seems to be stronger giving rise to a fixed and commensurate spacing.

3.5.2 Core level photoemission

The hypothesis of a strong interaction between PTCDI and TiO_2 becomes more striking by comparing the core level photoemission spectra (C1s and N1s) for 1 ML and 5 ML of PTCDI. In fact for strongly interacting substrates, the fine structure of high-resolution X-ray photoemission spectra is expected to change dramatically when passing from multilayer to monolayer (72).

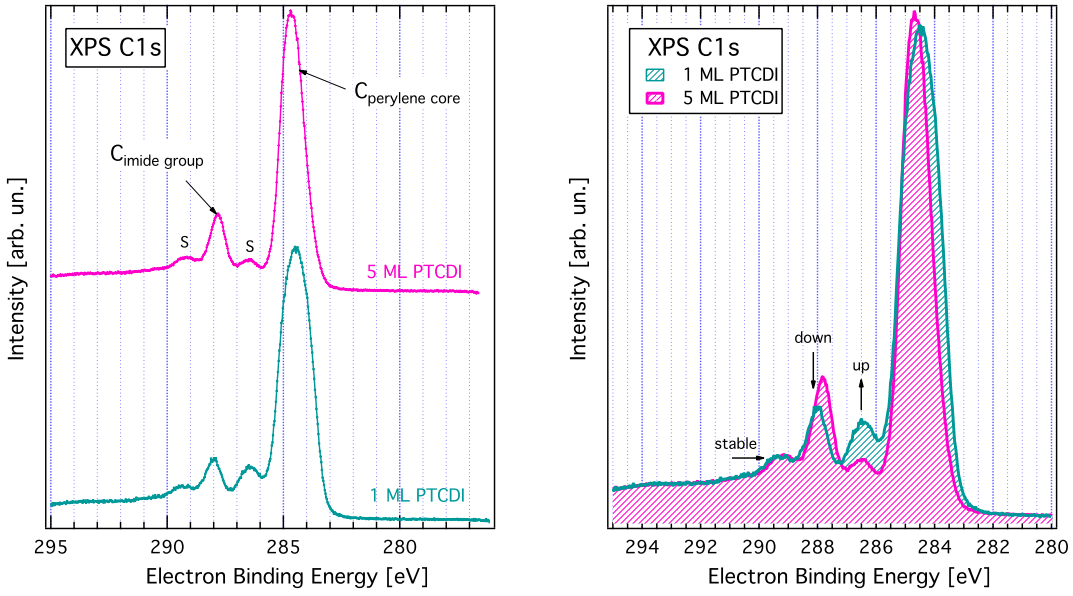

Figure 3.36: (Left) High-resolution C 1s XPS spectra of the PTCDI multilayer (top) and monolayer (bottom). (Right) Close inspection of the C 1s spectral differences between monolayer and multilayer.

Starting with the analysis of the multilayer C 1s we can distinguish a main asymmetric peak at 284.7 eV, a smaller peak at about 287.8 eV and two smaller satellite peaks (see Fig. 3.36, left). The main peak is attributed to the aromatic perylene core and consists of at least three different contributions from the various C atoms (73). The small peak at 287.8 eV belongs to the carbon atom of the imide groups. The other two small peaks are shake-up satellites associated to the main peak (satellite at 286.4 eV) and to the imide group (satellite at 289.2 eV), respectively. In the monolayer C 1s spectrum the main peak is considerably broadened towards lower binding energies, indicating that the various C 1s peaks of the perylene core are strongly shifted with respect to each other. At the same time the intensity ratio between the satellites and the functional group associated peak changes quite drastically (see Fig. 3.36, right). As the intensity of the shake-up belonging to the the perylene core grows that one of the imide group peak decreases.

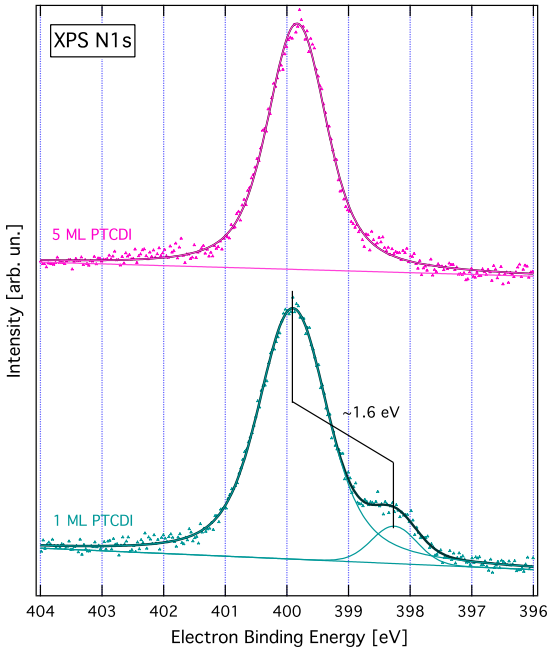

Figure 3.37: High-resolution N 1s XPS spectra of the PTCDI multilayer (top) and monolayer (bottom). The dotted curves are the experimental data, wheres the dark solid lines are the best fit. The peaks obtained from the best fit are also reported.

The multilayer N 1s spectrum consists of a single peak because of the presence of

only one nitrogen type (Fig. 3.37). On the other hand the monolayer N 1s spectrum shows a small shoulder on the lower BE side at approximately 1.6 eV from the main peak. The counterpart of this shoulder in the imide C 1s peak could be shifted of a similar value and being at the same position of the shake-up explaining the unexpected intensity ratio observed between these peaks.

A detailed explanation of the XPS findings will be given later with the support of the NEXAFS results. For the moment we can assert that they confirm the strong interaction between PTCDI and the TiO_2 surface which occurs mainly through the perylene core, i.e. strong broadening of the corresponding C 1s peak.

In Fig. 3.38 the substrate core level spectra are also reported, as a function of the coverage (clean, 1 ML, 5 ML). The O 1s spectra contains also the contribution of the molecule but the prevailing presence of the substrate oxygen makes it difficult to extract useful information. In the Ti 2p spectrum of the clean substrate we can distinguish the contribution of the Ti^{3+} atoms (small shoulder on the right of the main peak). After 1 ML of PTCDI deposition it completely disappears, as we can see in the normalized spectra (Fig. 3.39). This last point is very interesting but for stronger conclusions we must have a closer look in a different spectral region: the valence band.

3.5.3 Valence band photoemission

The valence band has been probed by using photons of energy 21.2 eV (UPS) and on different ionization thresholds (C K-edge and Ti L-edge).

UPS measurements have been performed simultaneously with HAS experiments, studying the valence band spectrum at different stages of the deposition. In Fig. 3.40 we show some selected spectra of a clean TiO_2 substrate (red) as well as of one monolayer (cyano), "bilayer" (1.5 ML, green), and two different multilayers (4 and 10 ML, spectra yellow and gray).

In the clean TiO2 spectrum we can recognize the O 2p density of states, extending from 3 to 9 eV, and a very weak Ti 3d state at 0.8 eV (see the enlarged view of the low BE region, Fig. 3.40 right). For multilayers a rich structure of numerous peaks is observed with the HOMO level positioned at $\sim$ 2.3 eV. After 1 ML deposition two new features are found in the region near to E_F, i.e. a broad peak centered at $\sim$ 1.0 eV and another peak at $\sim$ 2.5 eV. At higher coverages the first peak decreases in intensity until it disappears whereas the second one increases revealing itself as HOMO level.

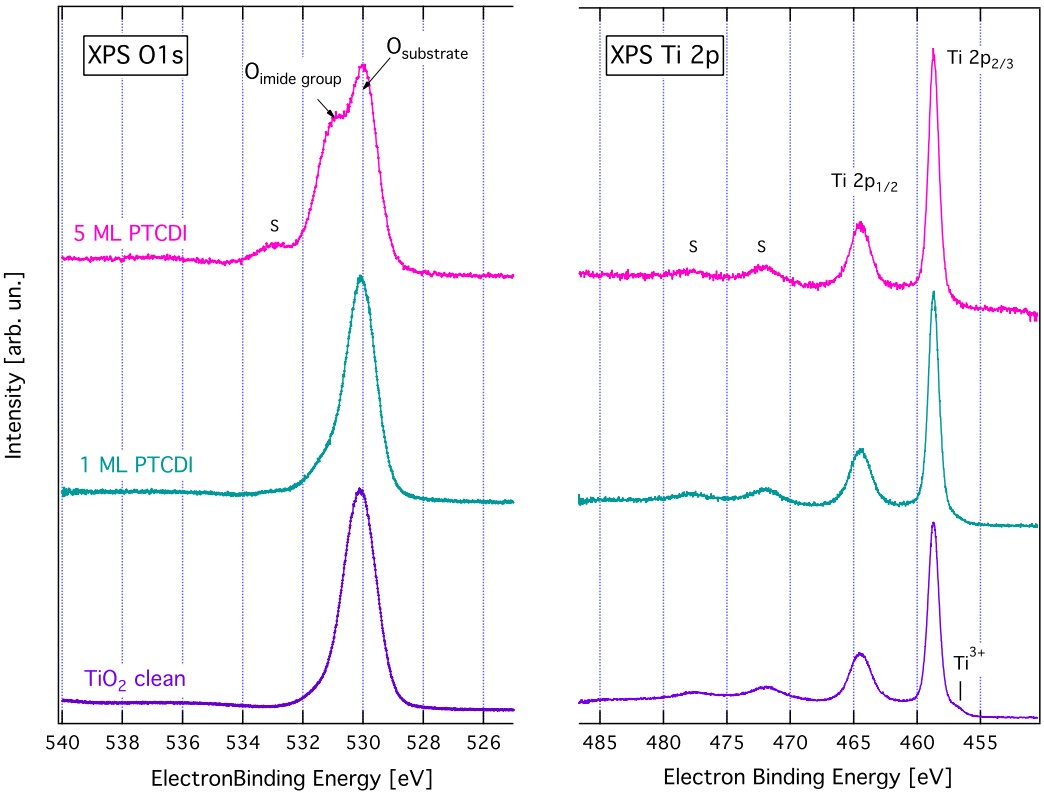

Figure 3.38: High-resolution O 1s (left) and Ti 2p (right) XPS spectra of the PTCDI multilayer, 1ML and clean surface.

The first peak is clearly an interface state since its intensity has a maximum at the monolayer phase and decreases for higher coverages. This finding is highly interesting since it indicates that PTCDI molecules is interacting very strongly with the TiO_2 surface giving rise to a new electronic state. Although the Ti 3d state is not so evident (red spectra), the new monolayer feature is very close to it. This makes difficult to understand the nature of this state: does it belong to the substrate (i.e. an enhanced Ti 3d state) or to the molecule?

The direct photoemission from the valence band (PES) is not able to answer to this question. A way to probe the chemical state of the valence band is to perform Resonant Photoemission Spectroscopy (RPES). In RPES a core electron is promoted into an unoccupied molecular orbital (LUMO). The so-called participator decay process leads to a final state equivalent to that of the direct photoemission from the occupied

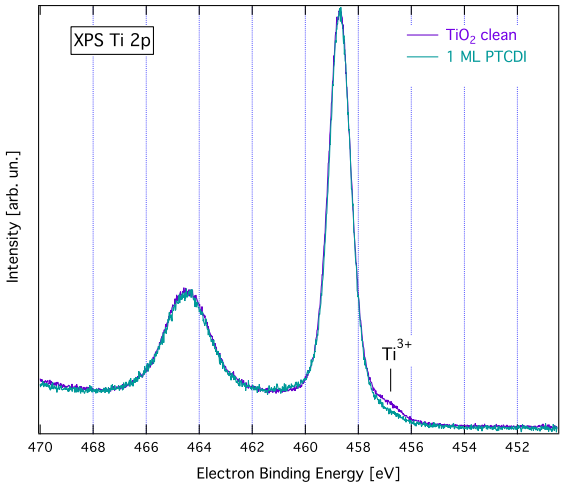

Figure 3.39: Normalized Ti 2p spectra of the clean surface and 1ML of PTCDI. After deposition the Ti^{3+} component results reduced in intensity.

molecular orbitals (HOMOs). In spite of the fact that final states in non-resonant and resonant photoelectron emission are equal, the intermediate state of RPES (core excitation) determines an altered intensity ratio of the spectral features with respect to PES. This different intensity ratio is explained by different selection rules. In particular, for RPES, the occurrence of resonating spectral features in the VB requires the spatial overlap among the involved wave functions (Ψ_{core}, Ψ_{LUMO}, Ψ_{HOMO}) proving that the filled state wave function is spatially located close to the selected core state and so must be to the Ψ_{LUMO}. In this way RPES enables a direct chemical identification of the VB features. In other words the selection of a specific adsorption edge, C1s or Ti 2p, allows one to assign the new electronic state either to the PTCDI molecule or to the TiO_2 substrate.

On the left side of Fig. 3.41 it is shown the region near to the E_F for 1 ML of PTCDI, probed by different photon energies across the C1s ionization threshold (see right panel of the same figure). As it can be seen, both the HOMO level and the new electronic state are detectable on the C1s edge, confirming the molecular nature of the interface state, from now on named HOMO'.

Finally, we focused on the Ti 3d state, checking its intensity before and after deposition. In Fig. 3.42 (top) is reported a bidimensional representation of the Ti L-edge RPES for both the clean surface and the monolayer phase. The abscissa is the binding

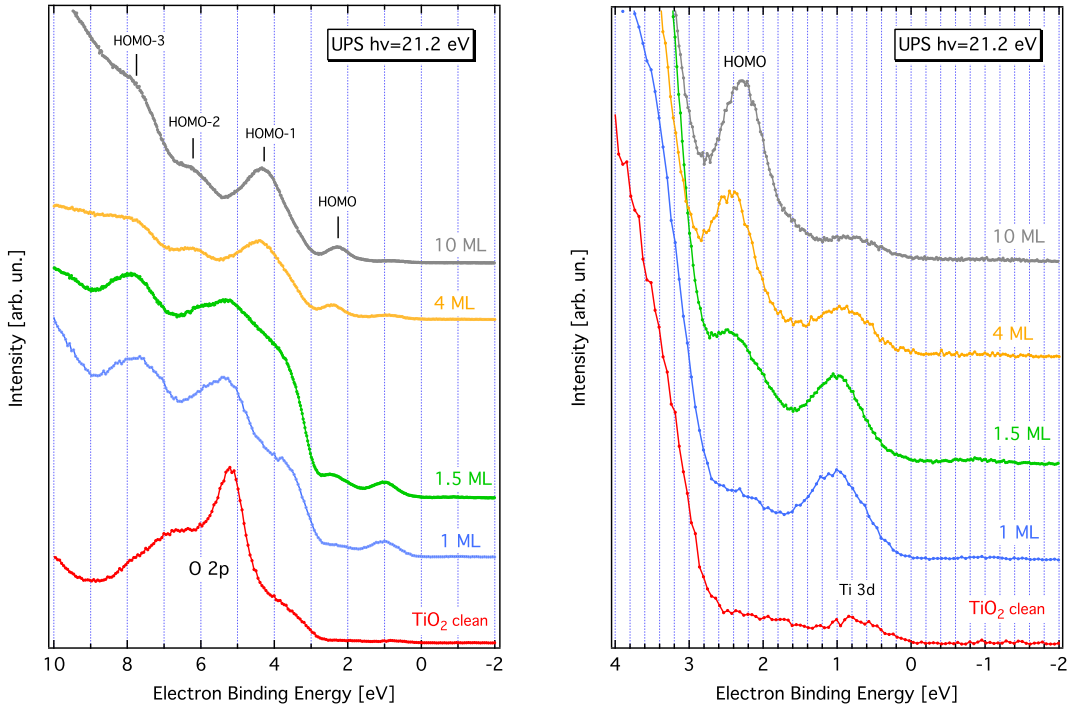

Figure 3.40: (Left) He-I UPS spectra of the clean TiO_2 surface (red), of a monolayer (cyano), an incomplete bilayer (green), and multilayers (yellow-gray) of PTCDI. The predominant peaks of the molecular layer are denominated by HOMO, HOMO-1, HOMO-2 and HOMO-3. The O 2p density of state is also indicated. (Right) Enlarged view of the low binding energy region corresponding to the spectra reported on the right panel. HOMO and Ti 3d state are indicated.

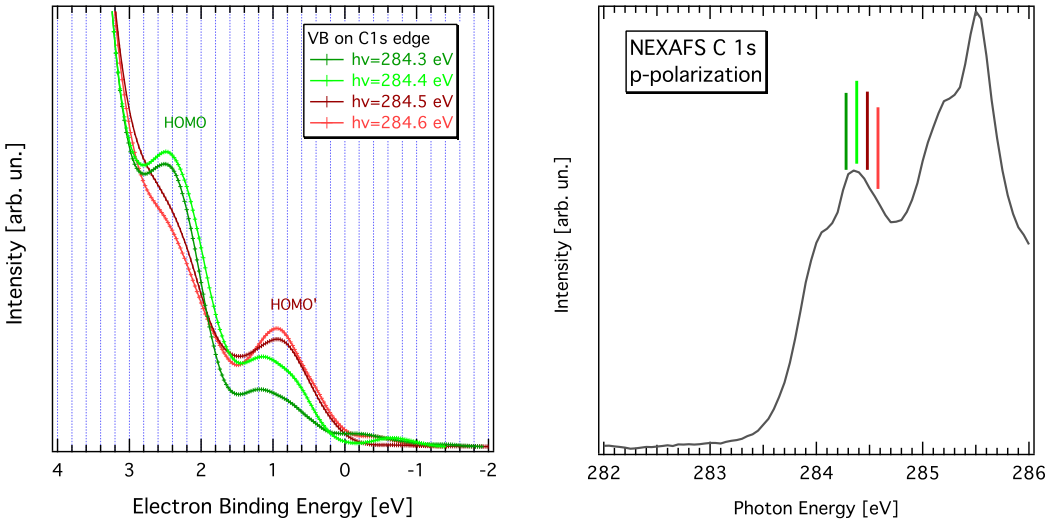

Figure 3.41: (Left) Resonant VB spectra for 1 ML of PTCDI recorded on the C1s edge at different photon energies which are indicated by bars of the same spectra color on the corresponding NEXAFS spectrum (left).

energy, the ordinate is the photon energy and the color scale is the intensity. Each cut at fixed photon energy is a valence band spectrum. The graph in between the two maps shows the titanium L-edge NEXAFS spectrum (red curve) measured simultaneously with the RPES.

Starting with the analysis of the clean surface (left map) it is evident that the Ti 3d state (highlighted in the yellow rectangle) resonates when the photon energy corresponds to some maxima of the NEXFAS spectrum. In particular the maximum of intensity is reached with a photon energy of 459.6 eV. The map corresponding to the monolayer phase shows a strong attenuation of the Ti 3d state. A better estimate of the Ti 3d intensity attenuation is given in the bottom graph of the Fig. 3.42. Here the VB spectra corresponding to the photon energy of 459.6 eV are reported for the clean surface and the molecular film. The O 2p density of states is also included. After intensity normalization to the Ti MVL Auger line (not shown), the two spectra match perfectly (see O 2p band) except to the Ti 3d state. The intensity reduction ($\sim$ 60%) of the Ti 3d state is consistent with what found in the Ti 2p XPS spectra and suggests that the new molecular state (HOMO') is derived from the former unoccupied molecular orbital (LUMO) which is partially filled from the electrons of the defect state,

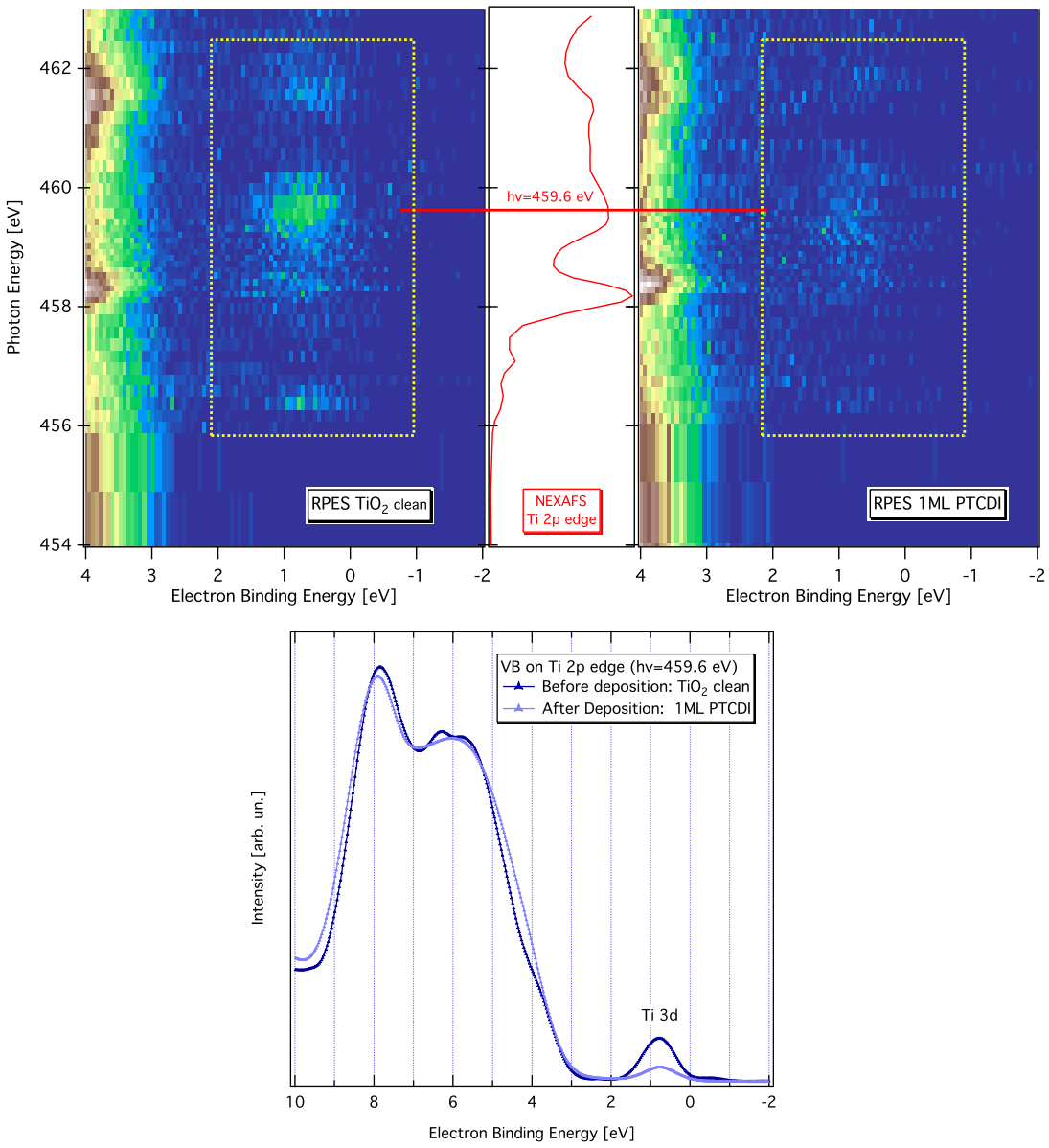

Figure 3.42: (Top) 2D maps of the Ti L-edge RPES for the clean surface (left) and 1 ML of PTCDI (right). Between the two maps it is reported the titanium L-edge NEXAFS spectrum (red curve) acquired simultaneously with the RPES. (Bottom) Normalized resonant VB spectra at the photon energy of 459.6 eV before and after deposition of 1 ML of PTCDI. A strong decrease of the Ti 3d intensity is observed, when passing from the clean surface to the monolayer phase.

i.e charge transfer.

In Fig. 3.43 we can compare VB spectra for 1 ML of PTCDI both on the C K-edge and on the Ti L-edge. Now, at a photon energy of 459.6 eV the Ti 3d state can be definitively discriminated, being at ~ 0.2 eV below the new molecular state (HOMO').

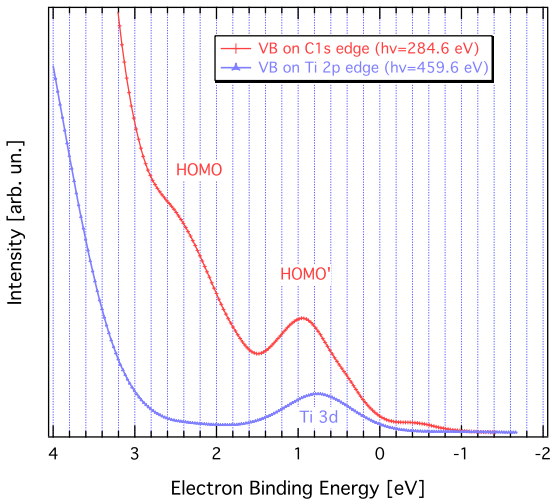

Figure 3.43: (Right) Comparison between the VB spectra recorded on the C 1s edge and on the Ti 2p edge for 1ML of PTCDI.

3.5.4 NEXAFS study

The results from the occupied states are complemented by the near edge adsorption fine structure (NEXAFS) data representing the unoccupied states. With this tecnique we can particularly address the issue, whether the new HOMO' in the monolayer phase is effectively derived from the partially filling of the LUMO state. Fig 3.44 shows NEXAFS spectra near the carbon edge for p-polarization. The top spectrum represents a 5 ML PTCDI film on TiO_2 while the bottom spectrum was recorded for the monolayer. The sharp intense peaks below 290 eV are due to transitions from C 1s levels of the various C atoms into unoccupied π^* orbitals (71, 74). The first peak of the multilayer spectrum at 284.2 eV belongs to transitions from the peripheral perylene C atoms labeled **a-d** (in right side of Fig. 3.44) into the LUMO. The most intense peak at 285.5 eV is also derived from transitions which are mainly located on the perylene core. It can be attributed to transitions from the perylene C atoms to the next three higher

orbitals ($LUMO_1$-$LUMO_3$). The group of peaks at 287-290 eV (enclosed in the square) belongs to π^*-symmetry transition involving the imide group.

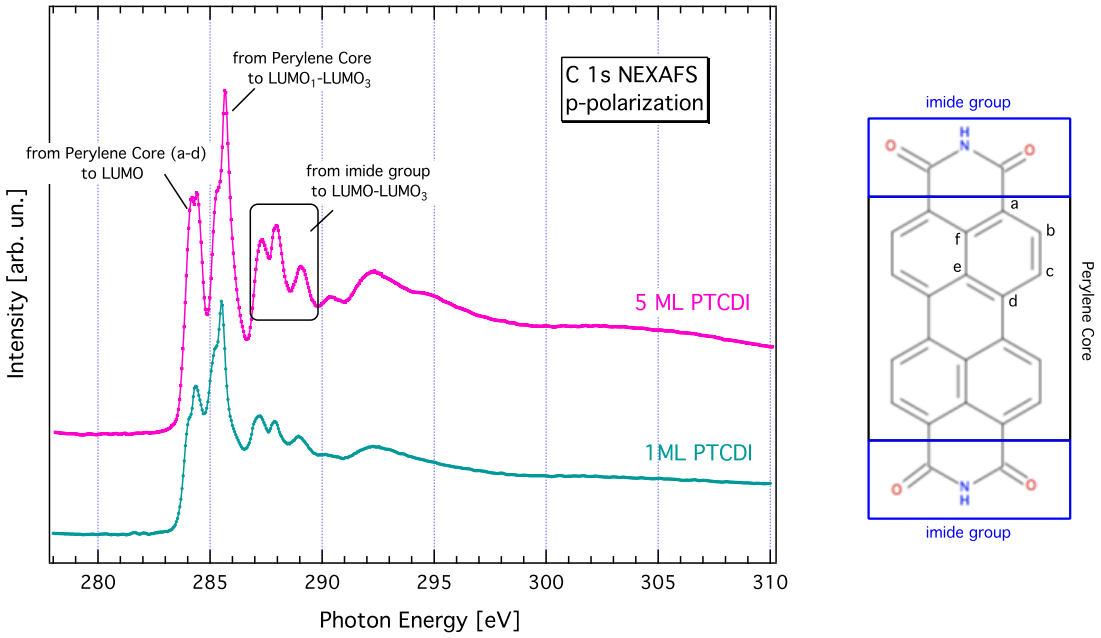

Figure 3.44: (Left) C K-NEXAFS data of the PTCDI multilayer (pink) and monolayer (green), recorded in p-polarization. The π^* resonances which are assigned to the perylene core and the imide group are indicated. (Right) Schematic PTCDI molecule; the different carbon atoms of the perylene core are labeled a-f.

A closer inspection of π^* region is shown in Fig. 3.45 (left). As it can be seen, significant changes occur between multilayer and monolayer. In the monolayer phase the overall spectrum is shifted by an average value of 0.1 eV towards lower energies and the intensity ratio between the peaks is changed. In particular the LUMO level is strongly decreased in intensity and altered in its fine structure. These findings confirm that especially the LUMO level is involved in the interaction with the surface and that it is partially filled by the electrons of the substrate and pulled below the Fermi level giving rise to a new filled electronic state, as it is confirmed by our UPS observations.

The LUMO level is mainly localized on the perylene core since, as mentioned before, the transition C 1s $\rightarrow$ LUMO involves only the C atoms of the perylene core. Therefore a redistribution of the electric charge occurs between them and in particular among the

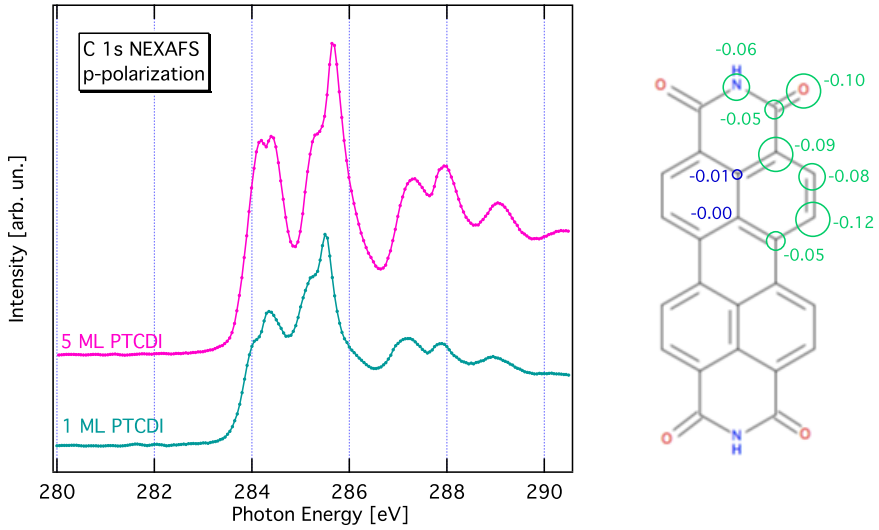

Figure 3.45: (Left) High-resolution C K-NEXFAS data of the π^*-energy region of the PTCDI multilayer (pink) and monolayer (green), recorded in p-polarization. In the monolayer spectrum a strong intensity decrease is observed for the LUMO resonance. (Right) Difference in the gas-phase Löwdin (75) charges between PTCDI and $PTCDI^{2-}$ showing the localization of negative charge on the peripheral carbons of the perylene core.

atoms labelled a-d. This is confirmed by the changes of the C 1s XPS spectrum, when passing from the multilayer to the monolayer phase. Here some of the components underlying the main peak (associated with the perylene core) are shifted towards lower binding energies causing a general broadening of the peak. Finally a recently published computational study on the electronic properties of the PTCDI dianion (75) predicts that the excess of electric charge is localized just on the pherypheral carbons of the perylene core, see Fig. 3.45 (right). Moreover the authors describe that also the imide group receives a fraction of electric charge. This could take in account of the shoulder a lower binding energies of the N 1s XPS peak. If the model is correct the intensity of this shoulder (10% of the overall N1s intensity) could represent an indirect measurement of how many oxygen vacancies (and associated excess of electrons) are present on the surface. Starting from the assumption that each oxygen vacancy interacts with one molecule, we found an oxygen vacancies concentration of a few per cent ($\sim$2%). This value is in good agreement with the expected one according to our sample preparation (76).

The new chemical state observed in the N1s XPS spectrum is responsible of the changes observed N K-edge NEXAFS spectra (Fig. 3.46). In the monolayer a new π^* feature is observed at 1.7 eV before the main π^*C-N resonance (77). This energy shift correspond to that observed in the N 1s XPS spectrum, between the main peak and the shoulder a lower binding energies. Therefore the new π^* resonance is a mere replica of the original feature, due to the presence of an additional initial state. The new feature is still detectable in the multilayer spectrum because of the 3D morphology associated with a Stranski-Krastanov regime of growth. Also the σ^* resonance shows a replica at lower photon energies. In this case the energy shift is greater with respect to the π^* resonances but it is difficult to predict changes above the ionization potential.

To conclude we notice that C 1s nexafs spectra (Fig 3.47) shows the similar dichroism observed in the case of pentacene, both for the monolayer and multilayer. For geometries scattering see section 2.4.2. When the photon beam is along the [001] direction we observe a decrease of the π^* features, when passing from multi to monolayer. An opposite situation is found for σ^* resonances. This means that molecules are tilted $\sim 35^\circ$ off the surface around their molecular axis, as confirmed by the additional dichroism detected when the beam is oriented along the $[1\bar{1}0]$. In the multilayer the polar and azimuthal dichroism is much less strong indicating that some reorientation is occuring.

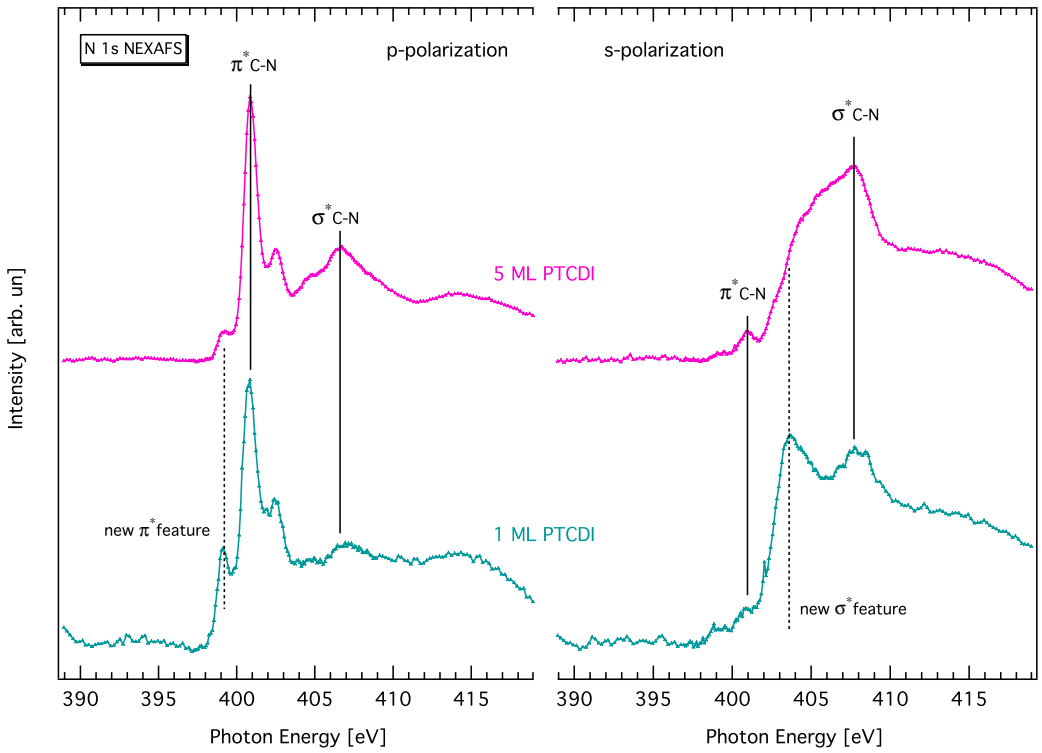

Figure 3.46: N K-NEXAFS spectra of the PTCDI multilayer (pink) and monolayer (green) recorded in p-(left) and s-polatization (right). Original and new features are indicate respectively by solid and dashed lines.

3.5.5 Comparision with perylene

The capability of PTCDI to accept electrons is due to the fact that its perylene core is electronically depleted by the electron-withdrawing action of the imide groups. This is well understood if we compare the C1s XPS spectra of PTCDI with that of perylene (see Fig. 3.48). The PTCDI spectrum is shifted $\sim$ 0.45 eV towards higher binding energies with respect to the perylene one. Therefore in the presence of an excess of electrons PTCDI has the tendency to accept them to recover, regarding the perylene core, an equilibrium condition.

In order to establish the reliability of this hypothesis we have also studied the interaction of the perylene molecule with the TiO_2 surface. UPS measurements reveal the VB of the monolayer phase as a perfect convolution between that of the clean surface and the multilayer phase (Fig. 3.49). In the region close to E_F we recognize

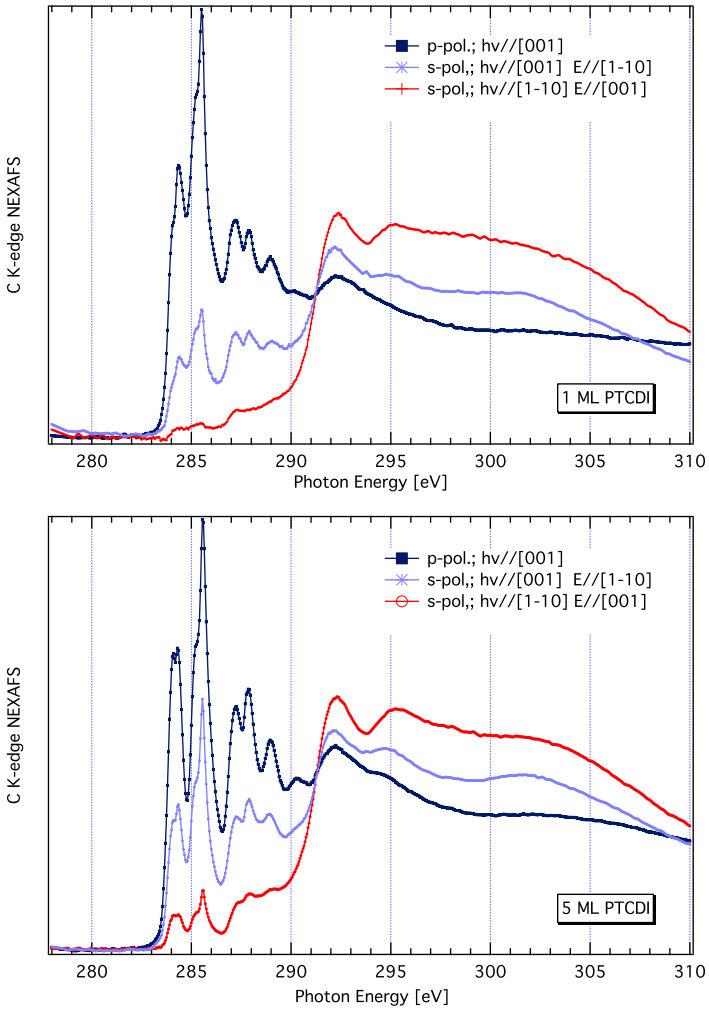

Figure 3.47: C K-edge of the PTCDI monolayer (top) and multilayer (bottom) for two opposite orientations of the surface with respect to the X-ray polarization (p- and s-polarization) and for two different azimuthal orientations in s-polarization.

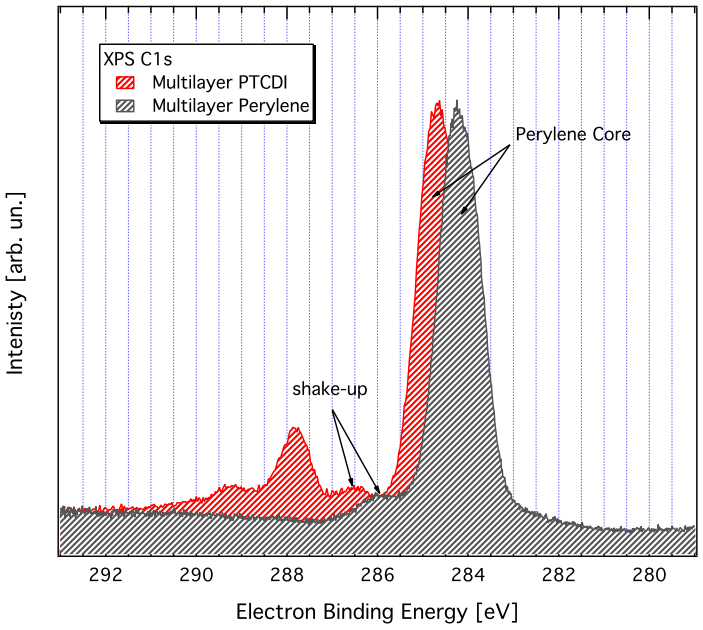

Figure 3.48: Different binding energy position of the C 1s peak for PTCDI and perylene molecule

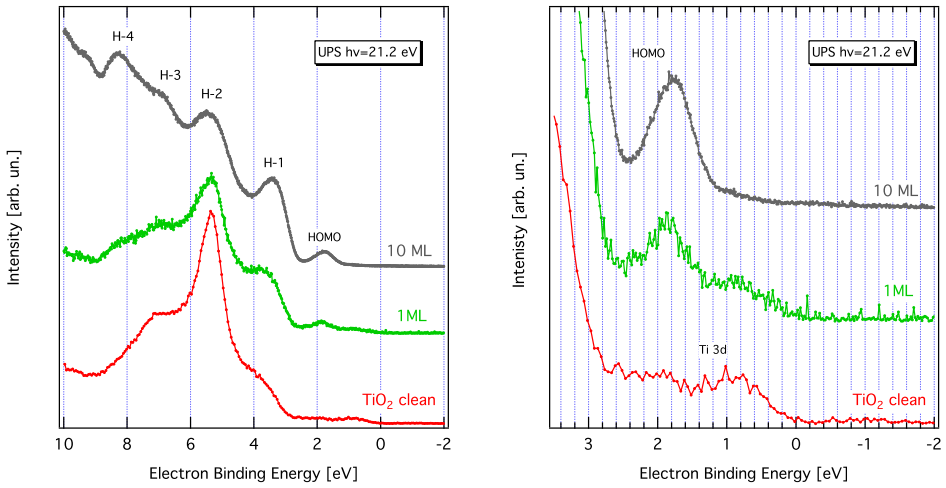

Figure 3.49: (Left) He-I UPS spectra of the clean surface, 1 ML and a multilayer of perylene. (Right) Corresponding enlarged view of the low binding energy region.

the HOMO level ($\sim$ 1.8 eV) and a residual intensity of the Ti 3d state without the occurrence of any additional state. On the left graph of Fig. 3.50 it is also reported the corresponding resonant spectra on the C 1s edge. The spectrum shows only one resonant feature which energy position corresponds to the HOMO level.

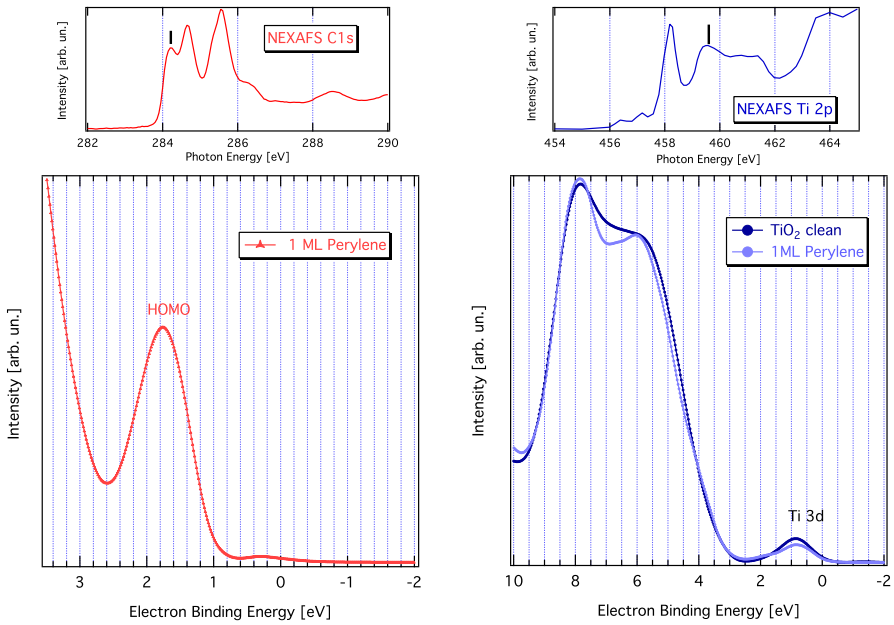

Figure 3.50: (Left) Resonant VB spectra on the C 1s edge for 1 ML of perylene. (Right) Resonant VB spectra on the Ti 2p edge before and after deposition of 1 ML of perylene. The probing photon energies are indicated in the corresponding NEXAFS spectra reported on the top graphs.

These results show clearly that no new electronic states appear at the interface between perylene and TiO_2. Therefore no charge transfer is occurring from substrate to molecule. In fact, by probing the Ti 3d state at resonance before and after deposition on the Ti 2p edge, we see that its intensity remains pratically unchanged (Fig. 3.50, right). Moreover no changes have been detected on the C 1s NEXAFS spectrum when passing from multi to monolayer (Fig. 3.51).

These findings confirm the weak interaction between perylene and TiO2 and the absence of charge transfer which requires the presence of functional groups like imide groups. Nevertheless, at the monolayer regime, perylene molecules are able to form an ordered phase characterized by a 4-fold periodicity along the [001] direction, as it

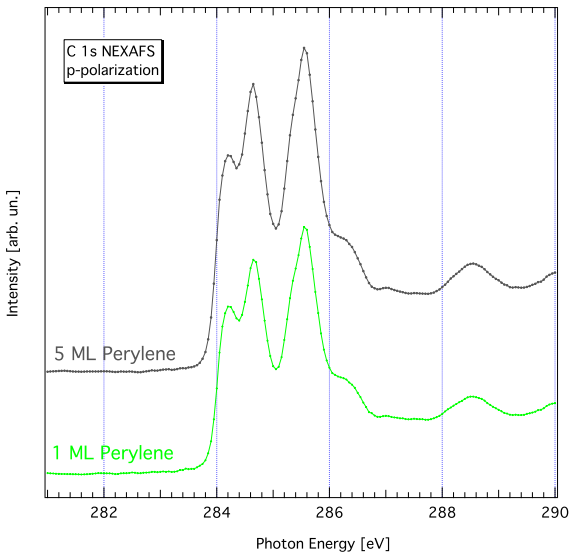

Figure 3.51: C K-edge NEXAFS of the perylene multilayer (gray) and monolayer (green), recorded in p-polarization.

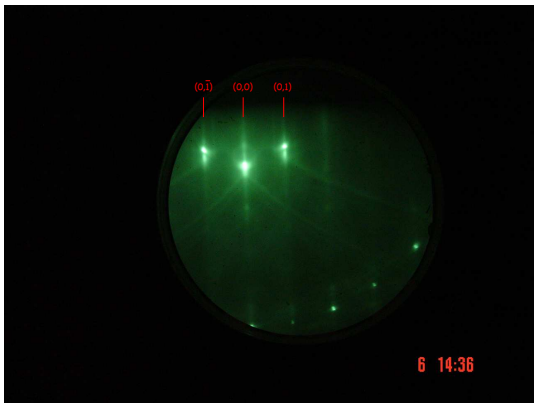

Figure 3.52: RHEED diffraction pattern along the [001] direction for 1 ML of perylene on the TiO_2(110) surface. Aside the substrate (0,±1) Bragg peaks some stripes of a 4-fold periodicity can be observed.

is possible to see from RHEED pattern (Fig. 3.52). In this case only the 3/4 peaks are observed indicating a possible evolution towards incommensurability. As see on the other molecules, the NEXAFS dichroism detected at the C 1s edge indicates that perylene molecules are tilted with respect to the surfaces along their molecular axis (Fig. 3.53).

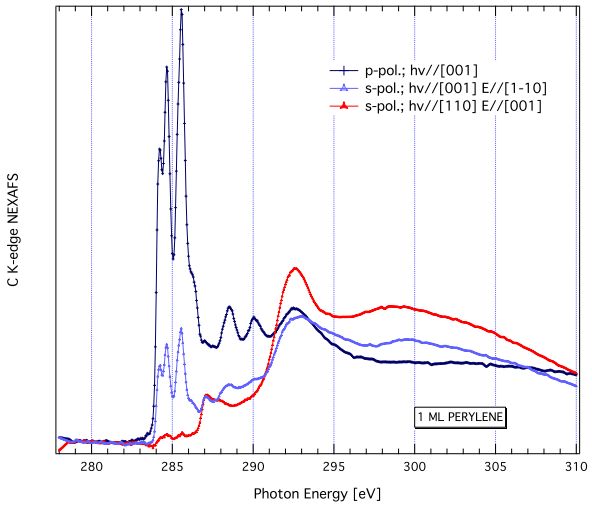

Figure 3.53: C K-edge of the perylene monolayer for two opposite orientations of the surface with respect to the X-ray polarization (p- and s-polarization) and for two different azimuthal orientations in s-polarization.

3.6 Conclusions

We have shown that the unreconstructed $TiO_2(110)$ rutile surface is well suited to drive the ordered growth of different kind of moelcules, at least for the first layer. In all cases the molecules preferentially adsorb in between the oxygen rows with the establishment of molecular superstructures (commensurate or not). In particular, the polycyclic aromatic hydrocarbons (pentacene, PTCDI and perylene) display a common self-assembly mechanism with their long side aligned along the [001] direction. In order to match the substrate periodicity along the $[1\bar{1}0]$ direction they are tilted according to their transverse width.

Apart PTCDI, all the molecules show a very weak interaction with the surface.

By STM we have observed that at RT C_{60} moelcules diffuse over the surface and require nucleation sites for islands growth, such as step edges. Due to the absence of a NEXAFS dichroism as a function of the polarization we have seen that C_{60} keeps its spherical symmetry after adsorption. Moreover there is no modification of the molecular orbitals of the deposited molecules with respect to that obtained for a multilayer. Finally XPD and molecular dynamics studies suggest a model of spinning C_{60} molecules along the surface normal, where the total angular momentum of two neighboring molecules is conserved.

In the case of pentacene, the film growth proceeds via an interplay of two main interactions: the intermolecular side-by-side attraction that drives the formation of continuous stripes along the $[1\bar{1}0]$ direction and the intermolecular head-to-head repulsion that tends to maximize the stripe spacing leading to an incommensurate periodicity. Additionally the perfect matching of the fine structure of the NEXAFS spectrum between the monolayer phase and that of the gas-phase, indicates that pentacene preserves its molecular character without being perturbed by the interaction with the substrate. At the same time the development of bulk-like electronic states confirm the strong side-by-side intermolecular attraction.

Finally we have performed a comparative study between PTCDI and perylene. PTCDI is the only molecule strongly interacting with the $TiO_2(110)$-1×1 surface. By UPS we have seen the appearance of a new electronic state just below 0.1-0.2 eV the Ti 3d peak. A combined RPES and NEXAFS study has shown that this new state is derived from the former LUMO which is partially filled by the electrons of the Ti 3d state. In fact, the strong intensity decrease of the LUMO level indicates that it is partially filled and pulled down below the Fermi level giving rise to the new feature observed by UPS. The molecular nature of the new feature (named HOMO') is also confirmed by the RPES C K-edge measurement. At the same time the RPES Ti L-edge shows a strong intensity decrease of the Ti 3d state after deposition, confirming the occurrence of a charge transfer from the Ti 3d state to the LUMO level with the consequent appearance of a new molecular defect state.

Moreover the N1s XPS peak shows a shoulder at lower binding energies which is directly related to the charge transfer from the Ti 3d state to the LUMO level. It corresponds to the 10% of the overall N1s peak intensity. If we assume one molecule per each oxygen vacancy we found a surface vacancies concentration of a few per cent (2%)

as expected by our sample preparation. The residual intensity of the Ti 3d state can be associated to oxygen vacancies in the deeper layers or to defects of different nature. The capability of PTCDI to accept electrons is due to the fact that its perylene core is electronically depleted by the electron-withdrawing action of the imide groups. This is confirmed by the spectroscopic study that we have performed on the perylene molecule. In this case we didn't observe the appearance of a new electronic state or an intensity decrease of the LUMO level or a strong quenching of the Ti 3d state.

By the exploitation of different molecular features (symmetry, electronic structure) we have given a full picture of the different interactions which can occur between organic molecules and the TiO_2(110)-1×1 surface.

4

Nitrogen-terminated molecules on gold

4.1 Introduction

Understanding and controlling electron transport through single molecules attached to metal electrodes could lead to the further miniaturization of electronic components and devices. In the past decade, significant experimental progress has been made in constructing such 'molecular junctions' and probing their electronic properties (78, 79, 80). Transport characteristics are influenced by intrinsic molecular properties such as molecule length, conformation, gap between the highest occupied (HOMO) and lowest unoccupied (LUMO) molecular orbitals, and the alignment of this gap to the metal Fermi level (81). Also the nature of the chemical linker groups used to bind molecules to metal electrodes plays a fundamental role: in ref. (82) it was shown that the conductance of Au-molecule-Au junctions, where the molecules are alkanes terminated with either amines (-NH_2), dimethyl phosphines (-PMe_2) or methyl sulfides (-SMe), exhibits large differences. The chemisorption of thiol (-SH) terminated molecules on Au surfaces has been widely studied in the past 30 years (83): the strong Au-S bond was therefore employed in the first molecular junctions studies (78). Recently it was shown (84, 85) that nitrogen terminated moelcules (amines or pyridines) anchored to gold electrodes exhibit well defined and experimentally more stable transport properties with respect to thiolated (-SH) molecules. This is surprising since the thiol-Au chemical bond is considerably stronger than the amine/pyridine-Au bond and

therefore one may expect that the stronger molecule-electrode link would reduce the stochastic switching and result into a more stable molecular junction. The reason for the well-defined and stable conductance of the N-termianted molecules has been attributed to the fact that the amine/pyridine-Au bond takes place through the nitrogen lone-pair and it is relatively insensitive to the local structure (86, 87, 88).

However, these studies have been restricted only to small molecules like diamino alkanes, diamino phenyls or bipyridines (84, 85). In this work we tried to exploit the N-Au link chemistry in order to study the electronic properties of a Au-Phthalocyanine-Au junction. In particular, we report the results obtained for the Terataaza-Cu-Phtahlocyanine in which the peripheral benzenes are replaced by pyridines. Phthalocyanines belong to a class of molecules well tested in organic electronic devices (89, 90, 91) and largely studied in surface science (92, 93, 94). Nevertheless a molecular junction that use this kind of molecules has not yet been reported.

In order to investigate the electron transport through molecules, one first needs the appropriate contacts. This chapter will start with a brief introduction on the conductance properties of atomic-sized contact followed by the description of the most commonly used technique for single molecule conductance measurements. After that we will focus on the investigated system.

4.2 Conductance quantization of an atomic-sized contact

In a macroscopic conductor, electrons travel in a diffusive way. This means that electrons get frequently scattered by collisions with obstacles such as impurities and grain boundaries. The average distance which an electron travels between two scattering events is known as the elastic mean free path l. The conductance G is given by the classical Ohms law:

$$G = \sigma \frac{A}{L} \tag{4.1}$$

where A and L are respectively the transverse area and length of the conductor, σ is the conductivity of the sample. However, when the length of the conductor becomes smaller than the elastic mean free path ($L < l$), the electron transport process changes from diffusive to ballistic in which the electron momentum can be assumed to be constant and only limited by scattering with the boundaries of the sample. Therefore the

classical Ohms law is no longer valid. For an atomic-sized contact of a metal, the contact width W is of the order of a few nanometers or even less and thus W is comparable with the Fermi wavelength λ_F. We therefore enter into the full quantum limit. The scattering approach pioneered by Landauer (95) is employed to describe electron transport through such a contact. It relates the transport properties (conductances) with the transmission and reflection probabilities for carriers incident on the constriction.

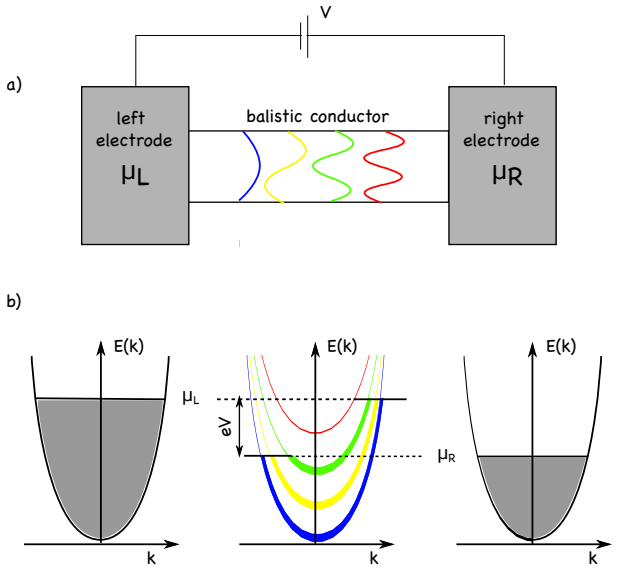

Figure 4.1: a) A ballistic conductor is sandwiched between two electrodes across which an external bias is applied. The electrodes emit electrons to the conductor with the distribution functions corresponding to electrochemical potentials μ_L and μ_R. The wave function of the different transverse modes are represented by colors. b) Illustration of the energy dispersion and occupation of the states. In the leads the transverse modes are filled up to their respective electrochemical potential. In the ballistic quantum wire only few transverse modes are filled up to the electrochemical potential. The +k/-k states are filled differently as denoted by the bold lines (96).

In an ideal ballistic wire with constant transversal confining potential along its axis, the quantum mechanical solution for the wave function of the wire gives electrons states which are plane waves along the wire axis and standing waves in the transverse direction. The energy of the electron states is:

$$E_n(k) = E_n + \hbar^2 k^2 / 2m \tag{4.2}$$

where k is the wave vector in the axis direction, n the index of the nth quantized transverse wave function (see Fig. 4.1 a). Each transverse wave function constitutes a so-called conductance channel. The macroscopic electrodes are introduced as ideal electron reservoirs in contact with the wire and have a well defined electrochemical potential (μ) and temperature. The electrodes inject electrons corresponding to their distribution function and are assumed to absorb the entering electrons without reflection. The applied voltage V shifts the electrochemical potential by $\mu_R - \mu_L = eV$, which leads to the change in the occupation of the electron states, as presented in Fig.4.1 b.

The imbalance between the occupation of the right and left moving states results in a net current in the wire, which is:

$$I = 2e \sum_{k,n} \frac{v_k}{L} [f_L(E_n(k)) - f_R(E_n(k))] = \frac{2e}{h} M \int_{\mu_L}^{\mu_R} [f_L(E) - f_R(E) dE] \tag{4.3}$$

where the $f_{L/R}$ are the Fermi distributions in the left and right electrode, n runs over the channels with occupied states, and L is the length of the wire. The sum over k is replaced by an integral over E using one dimensional density of states $\rho(E) = 1/v_k\hbar$. M is the number of available channels as determined by the diameter of the wire. At zero temperature $f_{L/R}(E)$ are step functions, equal to 1 below $E_F + eV/2$ and $E_F - eV/2$, respectively, and 0 above these energies. This expression leads to the conductance:

$$G = \frac{I}{V} = \frac{2e^2}{h} M = G_0 M \tag{4.4}$$

which is quantized with the unit of the conductance quantum, $G_0 = 2e^2/h$ $(12.9\ k\Omega)^{-1}$. This demonstrates that an ideal (i.e. without scattering) perfect single mode conductor ($M = 1$) between two electrodes has a finite conductance G_0.

In general scattering can take place and the conductance of the conductor is better described by a transmission function T where several conduction channels can contribute to. The expression of conductance becomes:

$$G = G_0 \sum_M T_M \tag{4.5}$$

This is called Landauer formula (95) (97), where $0 < T_M < 1$ is the trasmission probability of each mode.

4.2.1 Breaking a gold contact.

The quantization of the conductance can be observed during the breaking process of a gold contact. The experimental techniques used to study metallic atomic-size contacts are all based on piezoelectric transducers which allow fine positioning of two metal electrodes with respect to each other. One of these techniques employs a mechanically controllable break-junction (MCBJ)(98) (99) in which a nanofabricated gold bridge is mounted on a flexible substrate. The bridge is broken and re-established by the piezoelectric control of substrate bending. The other commonly used technique employs a scanning tunnelling microscope in which the tip is driven into contact with a gold surface and the conductance is measured during subsequent retraction (100) (101).

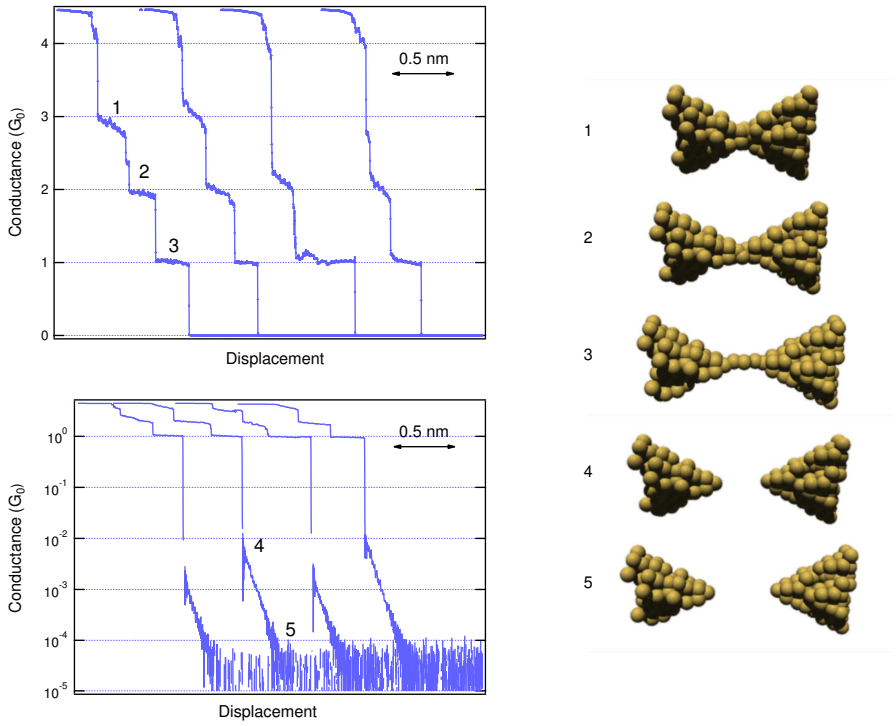

Figure 4.2: Sample conductance traces corresponding to the breaking of a gold contact. Top and bottom graphs show the curves respectively in the high and low conductance regime.

Fig. 4.2 shows some typical conductance traces obtained while streaching a gold contact in a STM-based experiment. The curves are recorded with our experimental

set-up (see section 4.4) in ultra high vacuum (UHV) at RT with a sample bias of 30 mV. First the contact is fully closed showing a conductance value above 4 G_0. Increasing the distance will lead to few atoms in contact, creating plateaus at multiple of G_0 (**1**, **2**, **3**) (top graph) . It has been proven (102) that in atomic gold contacts each gold atom contributes with a conduction channel (transverse mode). Hence, during the breaking process, the plateaus observed at n multiples of G_0 are attributed to n gold atoms in parallel in the narrowest part of the junction. After breaking of the single-atom contact (**1**), the conductance drops to 10^{-2} or 10^{-3} G_0 and an exponential decay is finally observed (from **4** to **5**) (bottom graph). This exponential decay with distance is due to the tunneling current between the contacts.

In order to analyze all the measured single conductance curves one needs to perform a statistical analysis. Due to rearrangements of the atomic contacts none of the single curves is similar to the previous ones. Histograms of a large bunch of single conductance curves are therefore constructed, by binning all the current data points measured in the course of a trace. The histogram built in this way returns the probability to measure a certain conductance value. Fig. 4.3 shows histograms corresponding to the high (top) and low (bottom) conductance regime. The histogram associated with the low conductance regime shows a log-log scale giving an overview over several order of magnitudes.

4.3 Molecular Conductance

It is possible to employ the STM-based break junction technique as a tool to contact molecules and measure their molecular conductance (103) (104). In this case the STM is repeatedly crashed in and moved out of an Au surface in the presence of molecules (previously deposited by drop-casting o UHV sublimation). As soon as the Au point contact is stretched and finally broken, one molecule can be trapped between the STM tip and the substrate and form a metal-molecule-metal junction allowing to measure its conductance.

In order to understand the flow of current through molecules, we need two basic ingredients: i.) the energy level diagram showing the molecular energy levels relative to the Fermi energy in the metallic contacts; ii) an estimate of the broadening of the molecular levels due to the coupling with the contacts.

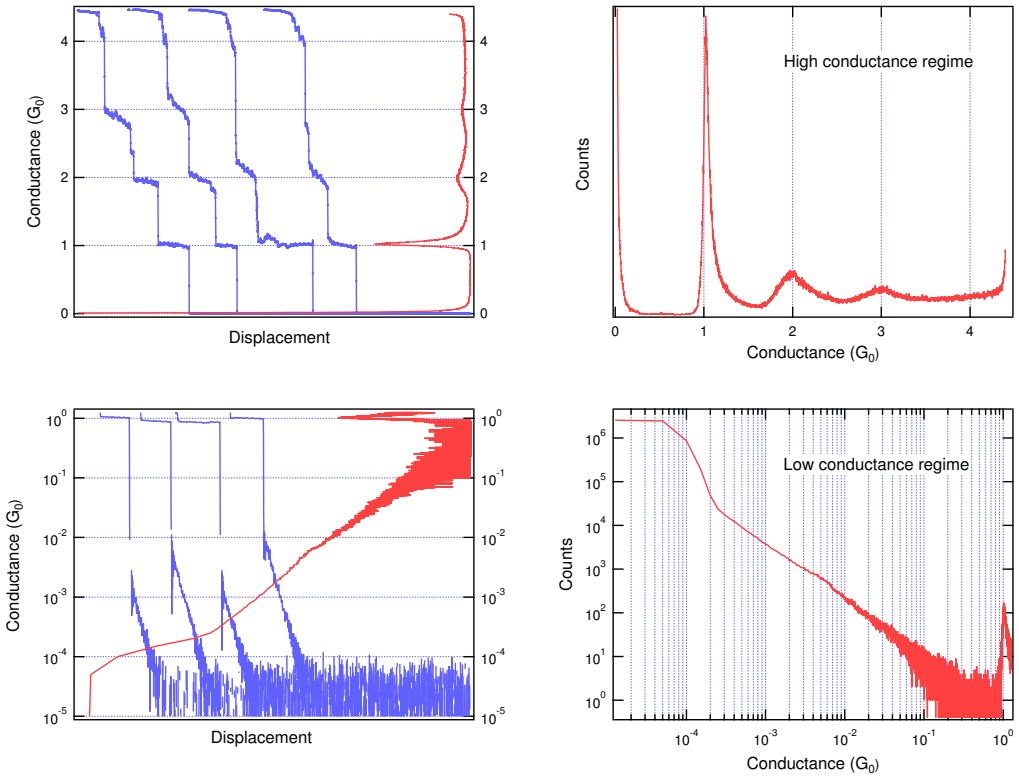

Figure 4.3: Corresponding histograms of the high (top) and low (bottom) conductance regime. The histograms are constructed from 3000 traces by using a bin size of $5 \times 10^{-5} G_0$

Usually the Fermi level lies somewhere inside the HOMO-LUMO gap. To see this, we first note that E_F position is determined by the requirement that the number of states below the Fermi energy must be equal to the number of electrons in the molecule. This number does not need to be equal to the integer number we expect for a neutral molecule. A molecule does not remain exactly neutral when connected to the contacts. It can pick up a fractional charge depending on the work function of the metal. However, the charge transferred δn for most metal-molecule combinations is usually much less than one. If δn were equal to +1, the Fermi energy would lie on the LUMO while if δn were -1, it would lie on the HOMO. Clearly for values in between, it should lie somewhere in the HOMO-LUMO gap (105).

"Common sense" suggests that the strength of coupling of the molecule to the contacts is important in determining the current flow - the stronger the coupling, the larger the current. A useful quantitative measure of the coupling is the resulting broadening Γ of the molecular energy levels. This broadening Γ can also be related to the time τ it takes for an electron placed in that level to escape into the contact: $\Gamma = \hbar/\tau$ (105) (106). Thus, the position of the molecular energy levels relative to Fermi as well as the degree of broadening due to coupling to the metal will dictate the transport properties through single molecules.

The top graph of Fig. 4.4 shows a set of conductance traces recorded during the breaking of a gold contact in the presence of the tetramethyl-benzendiamine (TMBDA). The measurements have been performed with our experimental set-up in UHV and RT. When the last metal contact is completely broken an additional conductance step is observed at approximately 6×10^{-3} G_0, in good agreement with results already published (107). This new step is ascribed to the formation of a stable molecular junction (87). As mentioned before the nature of the nitrogen-gold bond is responsible for a well-defined and reproducible molecular conductance.

The energy level alignment at the TMBDA/Au interface has been extensively studied by L. Venkataraman et al. (107). By measuring the conductance of a series of substituted benzene diamine molecules, they find that electron-donating substituents (like methyl groups), which drive the occupied molecular orbitals up, increase the junction conductance, while electron-withdrawing substituents have the opposite effect. These results provide evidence that the molecular HOMO level is closer to the Au Fermi level and therefore it constitutes the dominant conductance channel. This is

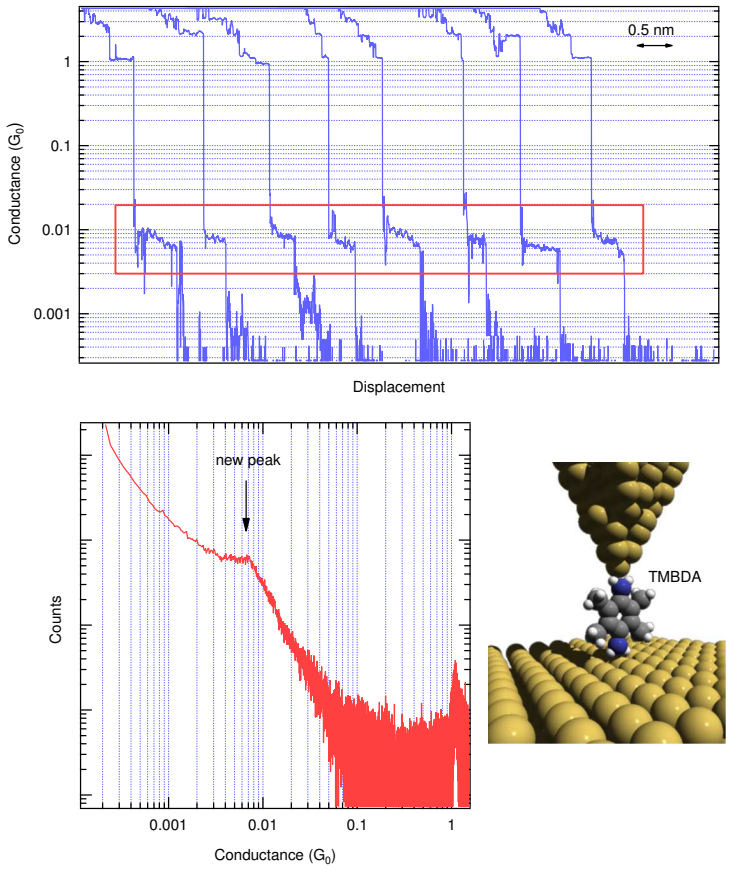

Figure 4.4: (Top) Conductance traces measured in the presence of tetramethylbenzenediamine in UHV and RT (bottom right). Sample bias: 30 mV. (Bottom left) Corresponding histogram constructed from 2000 traces by using a bin size of $5 \times 10^{-5} G_0$.

also confirmed by X-ray photoemission spectroscopy (XPS) and scanning tunneling spectroscopy (STS) measurements (108)(109).

4.4 Set-up development

The break-junction experiments reported in this chapter have been performed using a home-built UHV-LT-STM, located at the TASC National Lab (CNR-IOM). In Fig. 4.5 we report a picture of the UHV chamber (a) and the LN_2/LHe bath cryostat (b) hosting the STM-head (c). Fig. 4.5 (c) shows the major details of the STM-head: the sample holder is fixed in its location by means of a screw and the whole sample stage is moved by a slip-stick mechanism applying a sawtooth voltage to a piezo tube system, not visible in the figure but present below the trapezoidal sample stage of the STM head. The tip holder is also fixed by a screw on the piezo-tube dedicated to scanning.

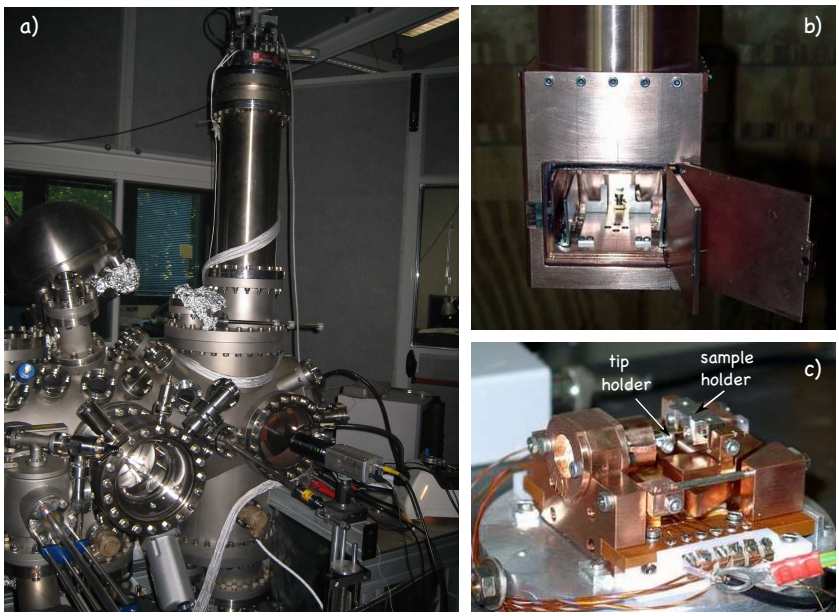

Figure 4.5: (a) The UHV-LT-STM located at the TASC National Lab (CNR-IOM). (b) The LN_2/LHe bath cryostat hosting the STM-head (c).

The STM control system (both hardware and software) is supplied by Nanotec Electronics. As seen in section 4.2.1 the main feature required for a break junction experiment is the possibility to measure thousands of traces needed to get a good statistics. Standard STM softwares are not able to perform automatically this kind

of experiment and in the case of the Nanotec software (WsXM) we can perform a maximum of 1000 consecutive traces (by using "IZ dialog" or "Lithography session"). Moreover there are two hardware limitations: 16.67 Ks/s as sampling frequency and 16-bit as resolution. A sampling frequency of 16.67 Ks/s can be critical in detecting events which can last approximately 1 ms (in the case of 1 G_0, less in the case of molecules). On the other hand a resolution of 16-bit is very limiting if we want to explore a wide range of conductance values, from 1 G_0 to several order of magnitude below.

In order to overcome these limitations we decided to operate the STM-based break-junction experiment with another set-up, still under development. The basic idea is to use the STM electronics to bring the tip very close to the surface. After that an additional alternating voltage (Z modualtion) is applied to the electrode controlling the tip-sample distance while the feedback circuit is off. In this condition the tip can be driven into and out of contact with the sample more than 1000 times. The associated current is recorded with an additional acquisition board installed on another PC. The board (NI-4662) is characterized by a sampling frequency of 200 Ks/s and a resolution of 24-bit. It is also used to generate the Z modulation. A schematic of the resulting system is reported in Fig. 4.6.

The board is driven by a software that has been developed by using the Labview programming environment (National Instruments). A computer screen snapshot while software is running is reported in Fig. 4.7. The top left graph shows the Z modulation characterized by the frequency and amplitude specified in boxes 1 and 2. The curve of interest (when the tip is going out from the sample) is highlighted in red. The corresponding current data points are used for a real-time histogram building, as reported in the top right graph. In the bottom graph the current trace associated with the overall Z modulation is displayed. The number of traces to acquire is specified in box 3.

When the break-junction set-up is operated, we notice that approaching-retracting the tip always on the same point may give useless results since an increasingly high protrusion depleted by molecules is formed. In order to avoid this we added the option to move the tip in the xy plane (box 4 and 5) after a specified number of traces. The possibility to move the tip and repeat a set of measurements in a fresh zone is fundamental specially if molecular diffusion is prevented (i.e. LT). The command

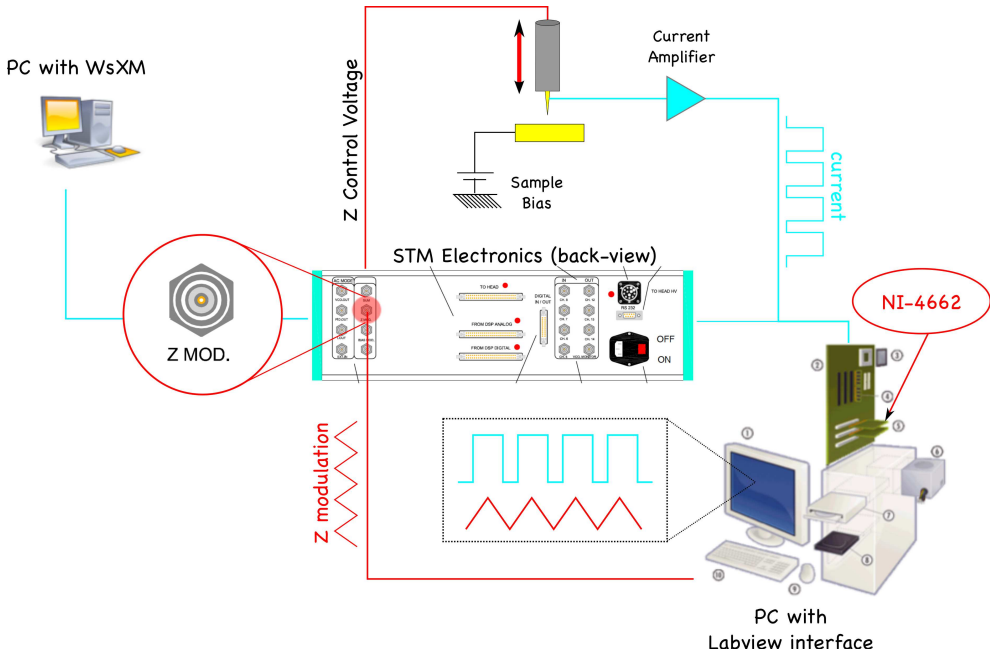

Figure 4.6: Schematic of the set-up for break-junction experiments.

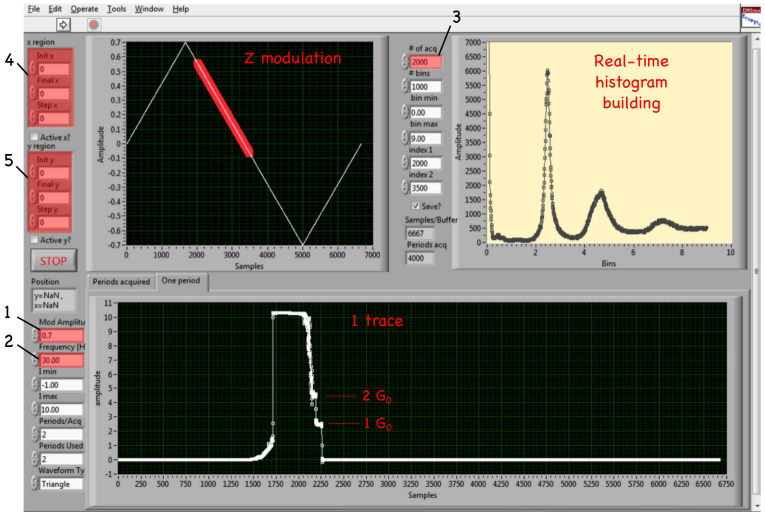

Figure 4.7: Software interface driving the NI-4462 board. The main boxes are highlighted in red and labeled from 1 to 5. The amplitude and frequency of the modulation are specified respectively in box 1 and 2. The number of traces to acquire is specified in box 3. Box 4-5 allow the xy movement.

associated with the "XY movement" is given by driving the WsXM software by remote control.

We perform most of these measurements by setting the current amplifier at gain 6 (10^{-6} A are converted to 1 V) with the sample biased at 30 mV. As the conductance of a gold nano-contact which is one atom thick is 1 G_0=77.5 μS, in these conditions the current measured through such a junction is 2.3 μA, as we can see from the histogram or the single trace reported in the software window (Fig. 4.7). When the current reaches a value of 10 μA (tip crashed into the sample) the current amplifier saturates to a constant value until the tip is kept away from the sample. Since the STM images are recorded with gain 8, during an experiment we can easily switch one configuration to another, in order to check the surface condition before and after a bunch of break-junctions.

4.5 Tetraaza-CuPc on Au(100)

The Tetraaza-Cu-Phthalocyanine (Copper(II) 4, 4', 4", 4"' tetraaza 29H, 31H phthalocyanine) is the azaanalog of the Cu-Phthalocyanine in which the benzene rings are substituted by pyridines (Fig. 4.8).

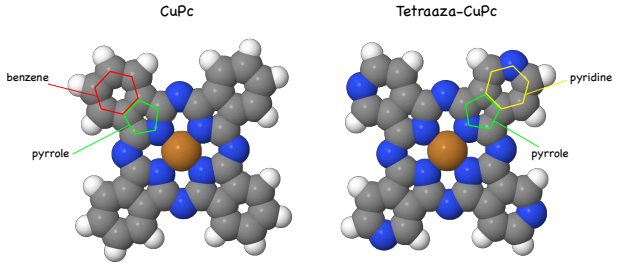

Figure 4.8: (Right) The Cu-Phtahlocyanine and the Tetraaza-Cu-Phtahlocyanine. They differ for an additional N atom in each benzene ring.

The azaPcs are less soluble in common organic solvents compared with the corresponding Pcs and thus it is difficult to purify them by chromatography or recrystalization. Moreover it is reported that azaanalogs cannot be purified by sublimation, even in high vacuum (110). Therefore we carried out a careful study of the evaporation conditions. Our compound is highly impure (∼90% Sigma Aldrich). The evaporation rate is very low and restricted to a small range of temperatures (590-620 K) beyond which the molecule decomposes (it changes from a purple to black powder). Thus it was necessary a considerable degassing and a very short distance between evaporator and sample (1-2 cm, see Fig. 4.9 bottom) and long evaporation times (1hr for ∼ 1 ML). The evidence of a successful evaporation was the appearance of a green/blue spot on a piece of steel (Fig. 4.9 top). Having found the proper evaporation conditions, it was possible to check the molecular integrity by spectroscopic characterization.

For all experiments a Au (100) single crystal has been used as substrate. The Au (100) surface exhibits a well-defined, large scale quasiehexagonal reconstruction. This reconstruction has a c(26×28) unit cell, often inaccurately described in the literature as a (20×5) (111). Fig. 4.10 a) shows a top view of the "(20×5)" reconstructed Au(100) surface in Local-Density-Approximation (LDA) (112). The frame below displays the z coordinate of atomic zig-zag rows in the "5" direction with the largest and smallest corrugation amplitude respectively. The variation shows that very different local

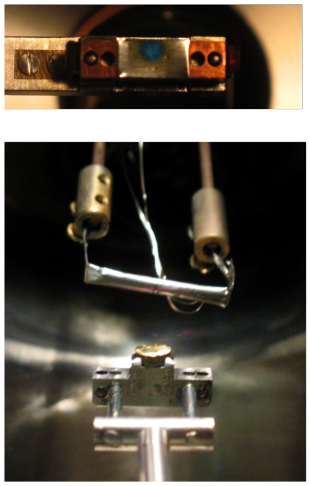

Figure 4.9: (Top) The green/blue spot associated with a thick film of Tetraaza-CuPc. (Bottom) Evaporator-sample configuration.

environments exist on the surface as a result of the two-dimensional reconstruction.

All the spectroscopic measurements presented in this chapter have been performed on the APE beamline (see chapter 2). STM and break-junction measurements have been performed in the same apparatus described in section 4.2.

4.5.1 Spectroscopic charaterization

An exhaustive spectroscopic study of the Tetraaza-CuPc has been performed for two different coverages (multilayer and sub-monolayer). The multilayer data will be presented in comparison with that obtained for a multilayer of CuPc on Ag(111). The expected similarity of their spectroscopic features will help to understand if the Tetraaza-CuPc can be evaporated without fragmentation and free from contaminants. At the same time we will able to see the effect of the additional N atoms on the characteristic spectroscopic features of phthalocyanines.

Fig. 4.11 shows the C1s and N1s XPS spectra for Tetraaza-CuPc (bottom) and CuPc (top) multilayers. In the C 1s spectrum of the azaPc we can still recognize the splitting of the main peak due to the chemical shift between the the benzene and pyrrole carbon atoms. The chemical shift of the carbons linked to the additional N atoms is such that the splitting is less resolved. On the other hand the N 1s spectrum is not so different in the two cases. The main difference with respect to the CuPc spectra

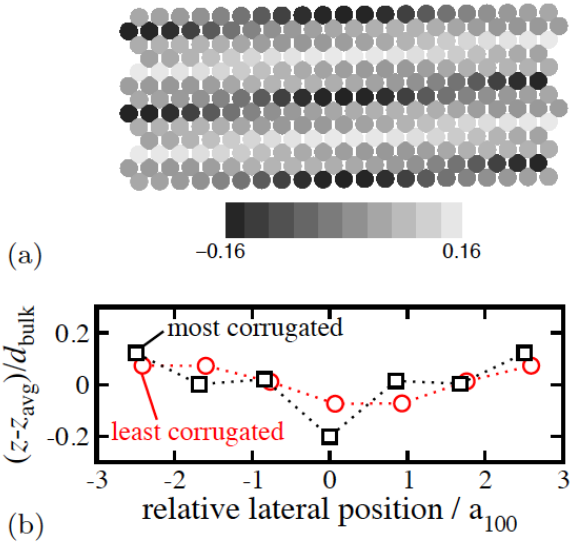

Figure 4.10: (a) Top view of the Au(100) "(20×5)" reconstruction model (LDA) (112). z coordinates of all atoms are color-coded in units of d_{bulk}, relative to the average z position of the plane. (b) Height profiles through the most corrugated and least corrugated surface areas (112).

is the energy shift of both core levels of approximately 0.5 eV towards higher binding energies. This could be due to the electron with-drawing effect of the pyridine nitrogen atoms on the other atoms of the molecule, determining an increase of the BE of the core levels. However, both the different screening effect of the two substrate as well as the different thickness of the films have to be taken into account and prevent from giving a unique explanation of the observed effect in the BEs.

All these findings are indicative of the fact that the Tetraaza-CuPc can be successfully evaporated without fragmentation and almost free from contaminants. However, we have found that the azaanalog of the CuPc is very sensitive to the X-ray beam exposure. In Fig. 4.12 a) a set of consecutive XPS spectra (both C 1s and N 1s level) of the same sample region is reported. Notice that the bottom and top spectrum represent the first and last scan, respectively. In the first scan the fine structure of the core levels is well resolved but further exposure to the X-ray beam results in a general broadening of the peaks with consequent smearing of the characteristic spectral features. Fig. 4.12 b) shows the result of several hours of X-ray beam exposure.

On the other hand, N K-edge NEXAFS seems to be not affected by the X-ray beam,

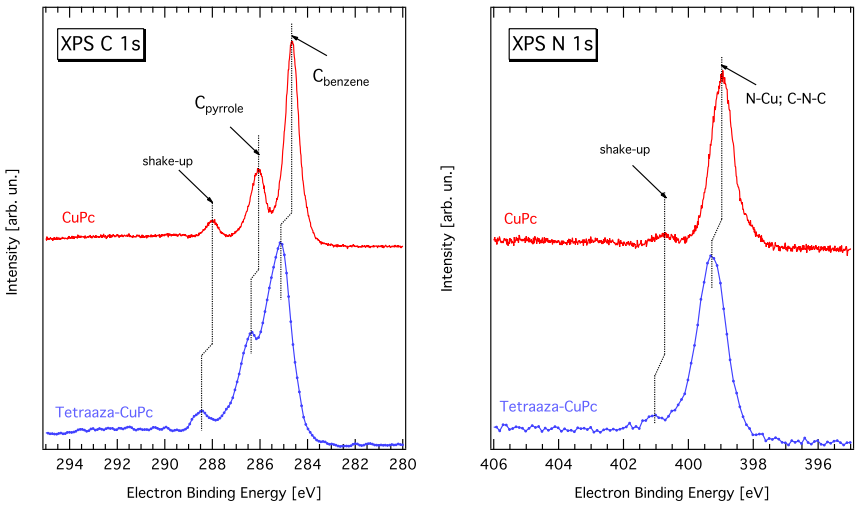

Figure 4.11: C 1s (left) and N 1s (right) XPS spectra for a multialyer of Tetraaza-Pc (bottom) and CuPc (top).

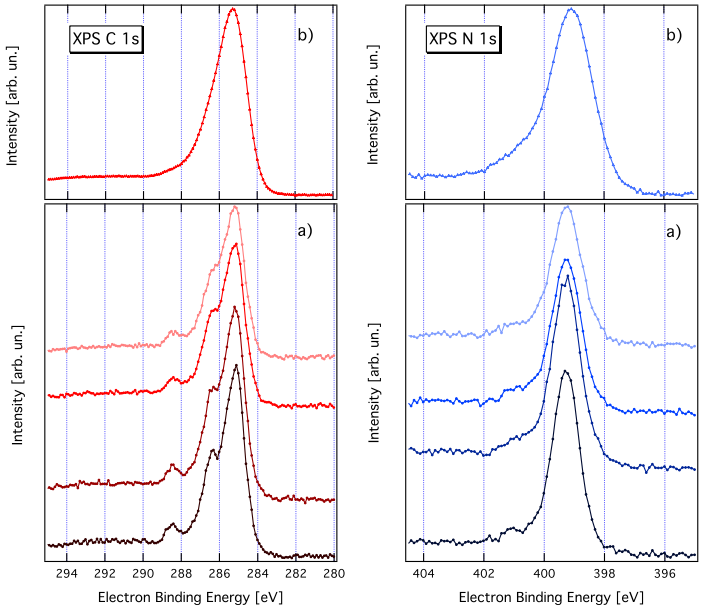

Figure 4.12: a) Consecutive C1s and N1s XPS spectra of the same sample region for a multilayer of Tetraaza-CuPc. b) Final shape of the spectra after several hours of exposure to the X-ray beam.

as we can see by the perfect matching between consecutive spectra of the same sample region (see Fig 4.13, top). The bottom graph of Fig. 4.13 shows the comparison of the N K-edge NEXAFS between a multilayer of azaPc and of CuPc. The two spectra have been simply superimposed since an absolute calibration of the photon energy has not been possibile in the case of the azaPc. Like in XPS, NEXAFS spectra don't show big differences in extra features when moving from one molecule to the other. The main differences are a more evident shoulder close to the first resonance and the relative intensity in the 399-401 eV region. In standard CuPc the first resonance and its associated shoulder is attributed to electron transition from both the nonequivalent N atoms to π^* orbitals mainly located on the pyrrole-rings, see Fig. 4.8. Nevertheless the possibility of contribution of π^* benzene-rings states cannot be neglected (113). Therefore the additional nonequivalent N atoms of the Tetraaza-CuPc can contribute to the first resonance with the occurrence of a more evident shoulder.

A molecular orientation study has also been performed on the N K-edge and Cu L-edge by using the different scattering geometries reported in the insets of Fig. 4.14. The intensity dichroism indicates that the molecules lie in an almost flat geometry as already seen for CuPc/Au(110) (94).

We also focused on the Tetraaza-CuPc sub-monolayer phase by comparing the XPS and NEXAFS spectra with those of the multilayer phase. In Fig. 4.15 the corresponding C1s and N1s spectra (left and right) are reported. The sub-monolayer spectra don't show relevant variations with respect to the multilayer except for a shift of 0.5 eV towards lower binding energies. Since both the C1s and N1s peaks are rigidly shifted by the same amount, we cannot attribute this effect to a specific chemical interaction of the molecule with the surface. It is most likely due to the screening effect, confirming that molecules are weakly bounded to the surface, as also observed for the tetramethyl-benzenediamine on Au(111) (109).

Fig. 4.16 shows the π^* resonances region of the N K-edge NEXAFS for both multilayer and submonoalyer. Also in the submonolayer phase the molecules preserve a lying-down adsorption geometry.

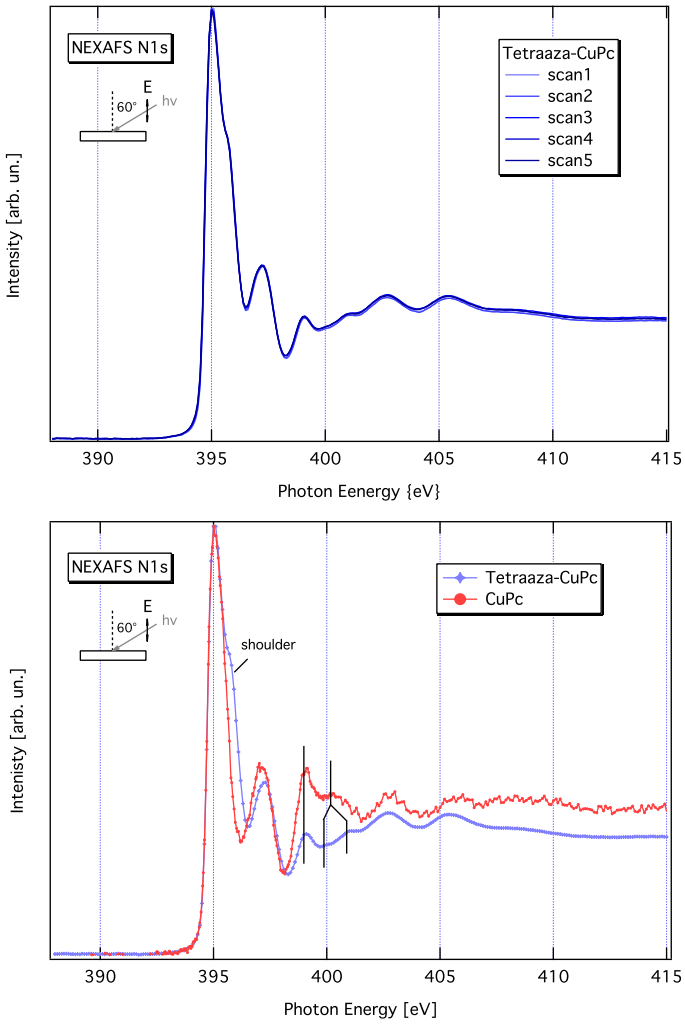

Figure 4.13: (Top) Set of consecutive N K-edge spectra for the same sample region. (Bottom) Comparision between the N K-edge spectrum of theTetraaza-CuPc multilayer and that of the CuPc multilayer. The spectra are recorded in the same scattering geometry indicated in the graph left side.

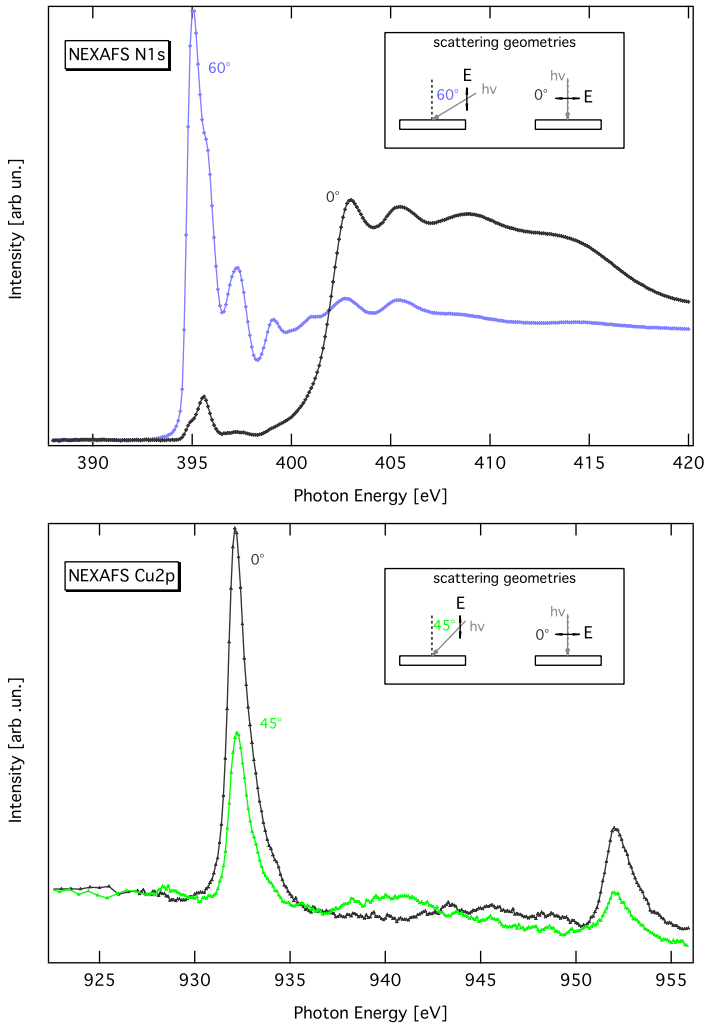

Figure 4.14: Detected dichroism on the N K-edge (top) and Cu L-edge (bottom) for a multialyer of Tetraaza-CuPc. The corresponding scattering geometries are indicated in the inset of each graph.

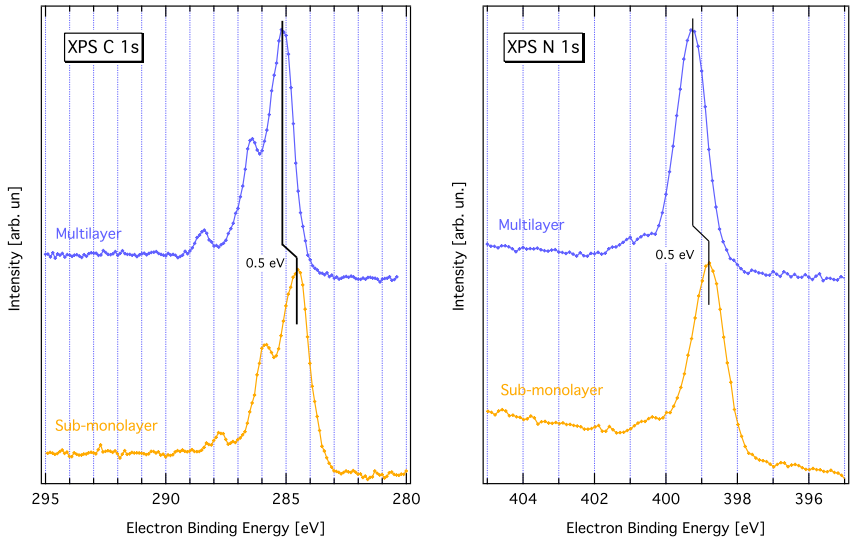

Figure 4.15: High resolution C1s (left) and N1s (right) XPS spectra of Tetraaza-Pc multilayer (top) and a submonolayer (bottom)

4.5.2 STM and Break-Junctions measurements

Thanks to the implementation of the experimental set-up it has been possible to perform STM and Break Junction measurements on the same apparatus. Fig. 4.17 a) shows a typical STM image obtained for 0.8-0.9 ML of Tetraaza-CuPc on the Au(100) surface at RT. The image is characterized by a diffuse blurring due to the high mobility of the molecules at this temperature. Sometimes the aggregation of small molecular islands is observed. A closer inspection of these structures (Fig. 4.17 b)) reveals that each island is composed by rows of molecules running along the $[01\bar{1}]$ direction. In each row we can find a variable number of molecules from a minimum of three to a maximum of nine. In the shown case we found six or seven molecules per row.

Fig. 4.18 shows a set of consecutive images with increasing resolution of the molecular details. In Fig. 4.18 a) we can glimpse the $\times 5$ Au reconstruction which seems to drive the formation of small islands. In fact the good matching between the lateral side of the molecule ($\sim$ 13.8 Å) and the $\times 5$ Au reconstruction (14.4 Å) leads the molecules to adsorb into the troughs. In the other direction, $[01\bar{1}]$, the molecules are able to follow partially the $\times 20$ Au reconstruction. A single molecular row is not perfectly parallel to the the substrate row indicating a different adsorption site for each molecule inside

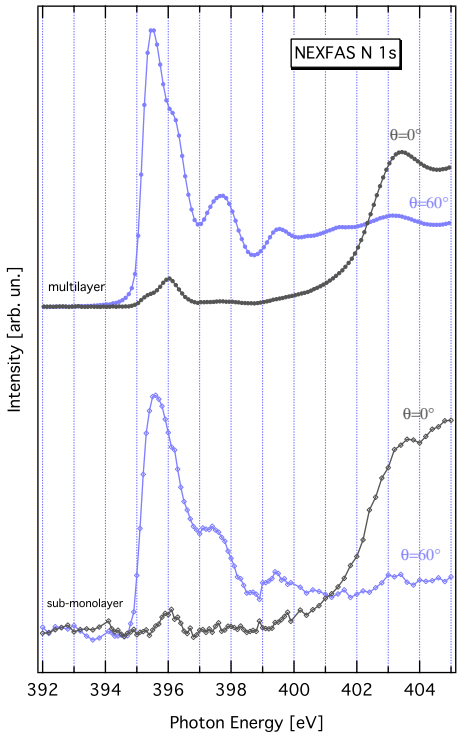

Figure 4.16: N K-NEXAFS data of the π^*-energy regions of Tetraaza-CuPc multilayer and submonolayer, recorded respectively in the same scattering geometries indicated in the inset of the top graph of Fig. 4.14

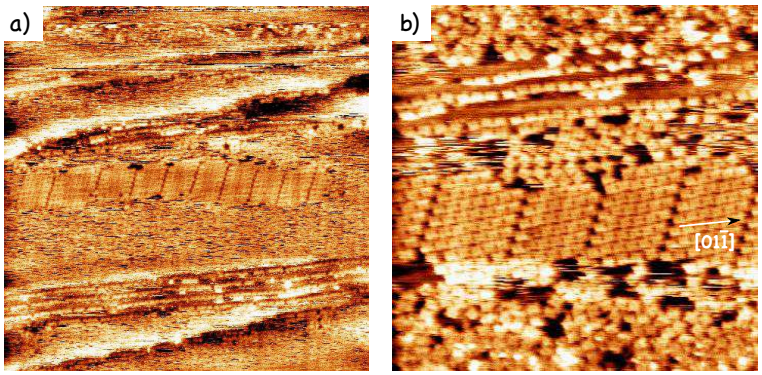

Figure 4.17: STM images of 0.8-0.9 ML of Tetraaza-CuPc on the Au(100) surface at RT. STM parameters: a) 100nm×100nm and b) 40nm×40nm. I=0.09 nA, V=1 V

the trough. Indeed, we can observe that molecules are not bright in the same way: the molecules at the beginning and at the end of a row are brighter than the molecule in the middle. Moreover the terminal molecules don't show an uniform brightness: one half is brighter than the other one. This means that the molecules in the middle adsorb only into the trough while the terminal molecules adsorb half into the same trough and half on the adjacent crest. After a row of 6/7 molecules the subsequent molecules repeat exactly the same adsorption scheme creating a defect (see Fig. 4.18 d) giving the final impression to have small different islands.

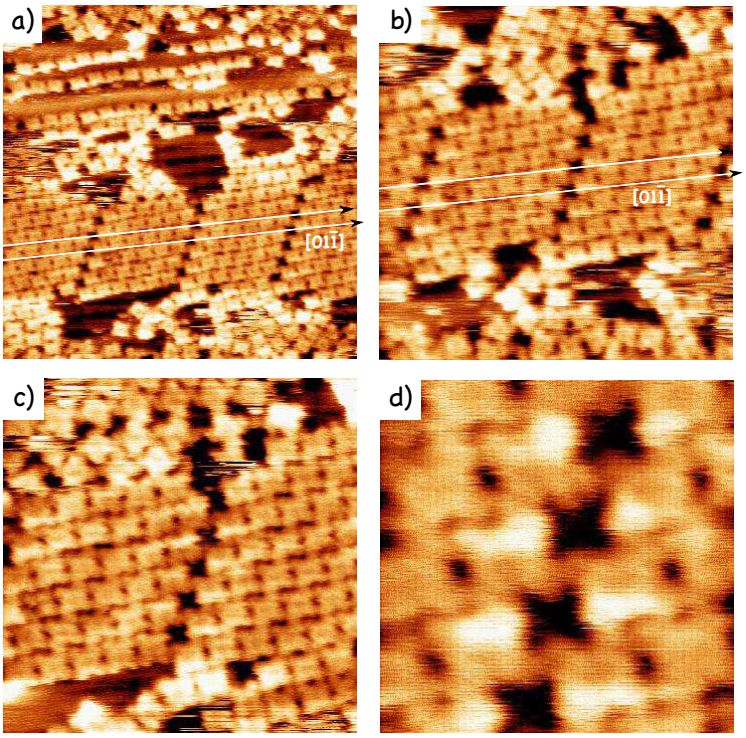

Figure 4.18: Set of consecuitive STM images with increasing resolution of the molecular details. STM parameters: (a) 30nm×30nm, (b) 20nm×20nm, (c) 15nm×15nm, (d) 5nm×5nm. I=0.09 nA, V=1 V

Due to the high mobility of the molecules at RT, we tried to cool the sample down to 55 K and even at 4 K after deposition. In this condition the molecules have been found frozen in small agglomerates or organized in different kind of islands (see Fig. 4.19). Similarly to what seen at RT we can find the formation of small islands but also the occurence of large domains in which the molecules are able to follow the substrate

rows for a length greater then 6/7 molecules. In Fig. 4.19 c) we can see how the molecular rows are slightly misaligned along the $[01\bar{1}]$ direction.

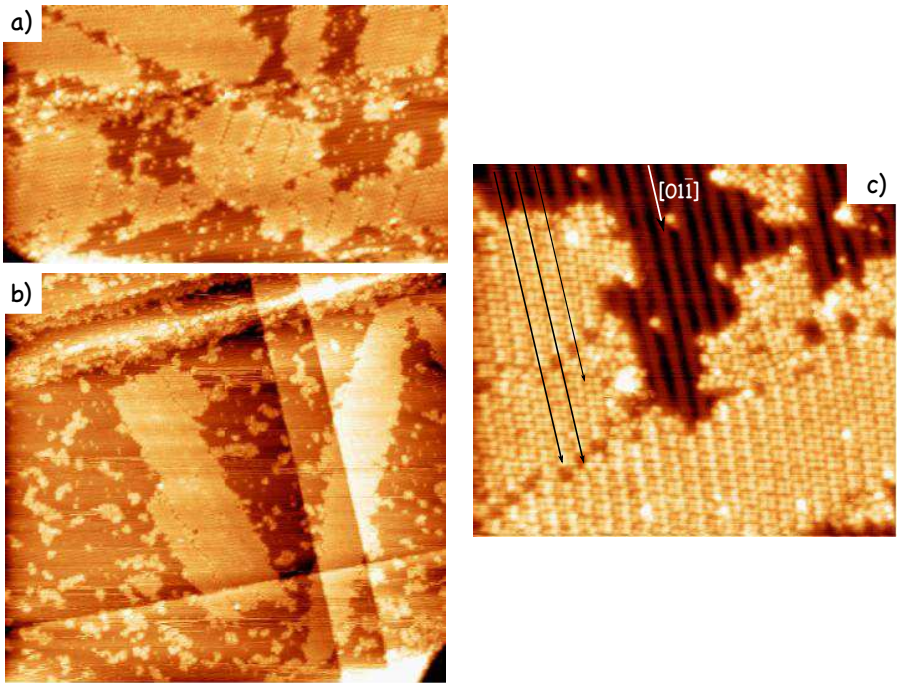

Figure 4.19: STM images for a sub-monolayer of Tetraaza-CuPC on the Au(100) surface at LT. (a) (b) We can observe the formation of large molecular domains as well as small islands and agglomerates. (c) Highly resolved STM image showing the not perfect alignment of the molecular rows along the $[01\bar{1}]$ direction indicated by black lines. Sizes: (a) 113nm×66nm, (b) 181nm×169nm, (c) 33nm×29nm.

By cooling the sample we obtained steady molecular patches on which to perform break-junctions experiments. Fig. 4.20 shows typical conductance curves selected from 200 consecutive traces performed in the same XY point at 55 K. After the breaking of the last metal contact (displacement=0) the conductance drops approximately to 10^{-3} G_0. After this drop very long steps occur before reaching the background noise. These steps are highly irregular with variable length and characterized by repeated jumps.

The overall steps length is found to be ∼0.7 nm (left panel, yellow curves) or ∼1 nm (right panel, red curves). These values are compatible with the molecule binding to the metal electrodes in two different configurations: one through pyridine nitrogen atoms belonging to the same side of the molecule (short side) and the other through

opposite pyridine nitrogen atoms (molecule diagonal or long side), see bottom part of Fig. 4.20.

The jumps occur every ∼0.1-0.2 nm leading to a gradual lowering of the conductance. At the beginning, when the junction is compressed we have higher values of conductance while, when the junction is elongated we have lower values. This molecular conductance behavior has been already observed for the 4,4-bipyridine-gold junction (114). Typical bypiridines conductance traces show a higher conductance step that precedes a lower conductance step, indicating that the molecular junction predominantly samples high and low conductances when successively compressed and elongated. The properties of the pyridine-gold link explain the observed switching behavior.

The N in pyridine is sp2 hybridized. This leaves one electron in an unhybridized p orbital, which contributes to the π-system. The lone pair on the N atom is in an sp2 orbital, which means it is directed away from the ring but in the same plane (Fig. 4.21). Therefore the lone pair is not involved in the π-system (HOMO-LUMO) responsible of the molecular conductance. At the same time it is involved in the bonding with the partially empty s-orbital on a specific undercoordinated gold atom on the electrode.

We can expect that an elongated junction, with the nitrogen-gold bond aligned to the molecule backbone, will have low electronic coupling between the π-system and the s-gold state and hence low conductance. On the other hand, the constraint imposed by the compressed junction (after breaking the last metal-contact) will drive strong tilting of the nitrogen-gold bond, which can result in stronger coupling and higher conductance.

In the amine case, the amine lone pair is naturally coupled into the main orbital responsible for conductance, for example, into the benzene π-system or the alkane σ-system (115). Changes in contact geometry do not, therefore, affect the measured conductance significantly, resulting in a single well-defined peak in the conductance histograms (87). In contrast, for the pyridine case, the nitrogen lone-pair electrons involved in the bond with the metal are actually orthogonal to the π-system, resulting in a junction conductance that can be quite sensitive to the orientation of the nitrogen-gold bond with respect to the mainly conducting orbital, the molecular LUMO or HOMO.

The conductance histogram built as described in section 4.2.1 only select conductance information and discard information about how conductance evolves with pulling.

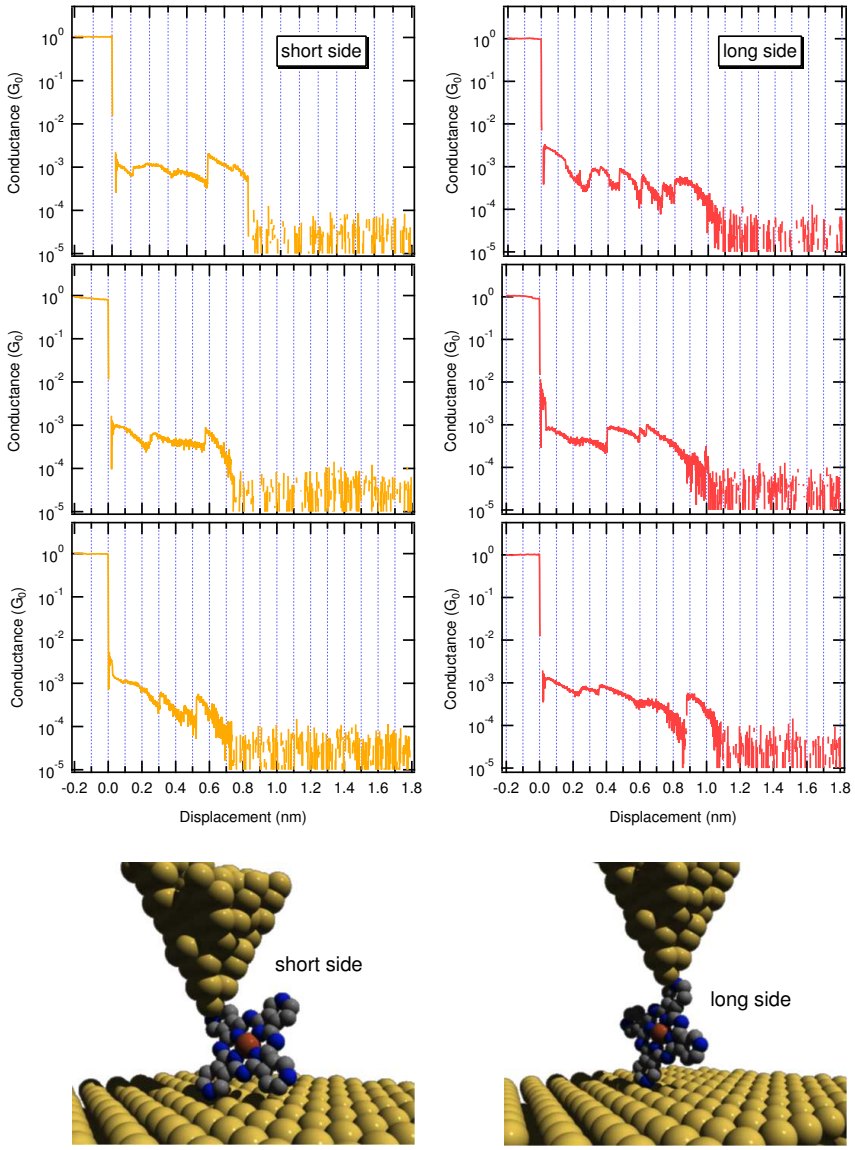

Figure 4.20: Typical conductance traces performed in the presence of tetraaza-CuPc at 55 K. The traces are characterized by very long steps spread around 10^{-3} and 10^{-4} G_0. The overall step length is found to be ~ 0.7 nm (yellow curves) and ~ 1 nm (red curves). They can be associated to different binding geometry, corresponding to the cartoons reported below.

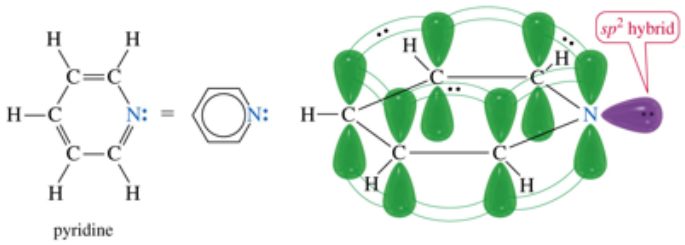

Figure 4.21: Spatial distribution of the N lone pair relative to the π-system in pyridine-like molecules.

In order to analyze the displacement information in a statistical manner, we construct 2-dimensional histograms, binning along both the conductance and elongation axis. We set the 1 G_0 rupture event as the origin of the elongation axis on each trace and then bin each measured trace by assigning every data point to a position on a 2D conductance vs displacement grid. The conductance axis uses logarithmic bins with 60 bins/decade. Fig. 4.22 (top) shows the histograms constructed using this procedure for a clean sample and in the presence of the Tetraaza-CuPc. Both histograms have been constructed by using sets of 200 consecutive traces recorded in different XY sample regions, for a total of 1000 traces. In the histogram corresponding to the clean surface we can recognize as blue spots 3 G_0 2 G_0 and 1 G_0. After 1 G_0 an exponentially decay is observed starting from approximately 10^{-2} G_0. In the case of Tetraaza-CuPc we can observe a diffuse spot between 10^{-3}-10^{-4} G_0 for a lenght of approximately 1nm.

The bottom part of Fig. 4.22 shows the integral of the 2D histograms (clean and molecule) between 0 an 3 nm. In this way we lose information about the displacement but it is clear that the molecular conductance value is centered around 7×10^{-4} G_0.

In order to know which is the principal conducting orbital in the Au-azaPc-Au junction we have also performed scanning tunneling spectroscopy (STS) measurements. Fig. 4.23 shows the normalized first derivative of the tunnelling current with respect to the sample bias (dI/dV)(I/V). This is obtained by averaging over 100 dI/dV spectra taken on single molecules belonging to molecular domains at 55 K. The curve gives an estimation of the local density of states across the Fermi level. Clear peaks at -1.1 V and 0.9 V indicates respectively the HOMO and LUMO position. Although the molecular orbitals are almost symmetrically distributed around E_F, the LUMO level is more broadened and closer to E_F by 0.2 eV in comparison with the HOMO level.

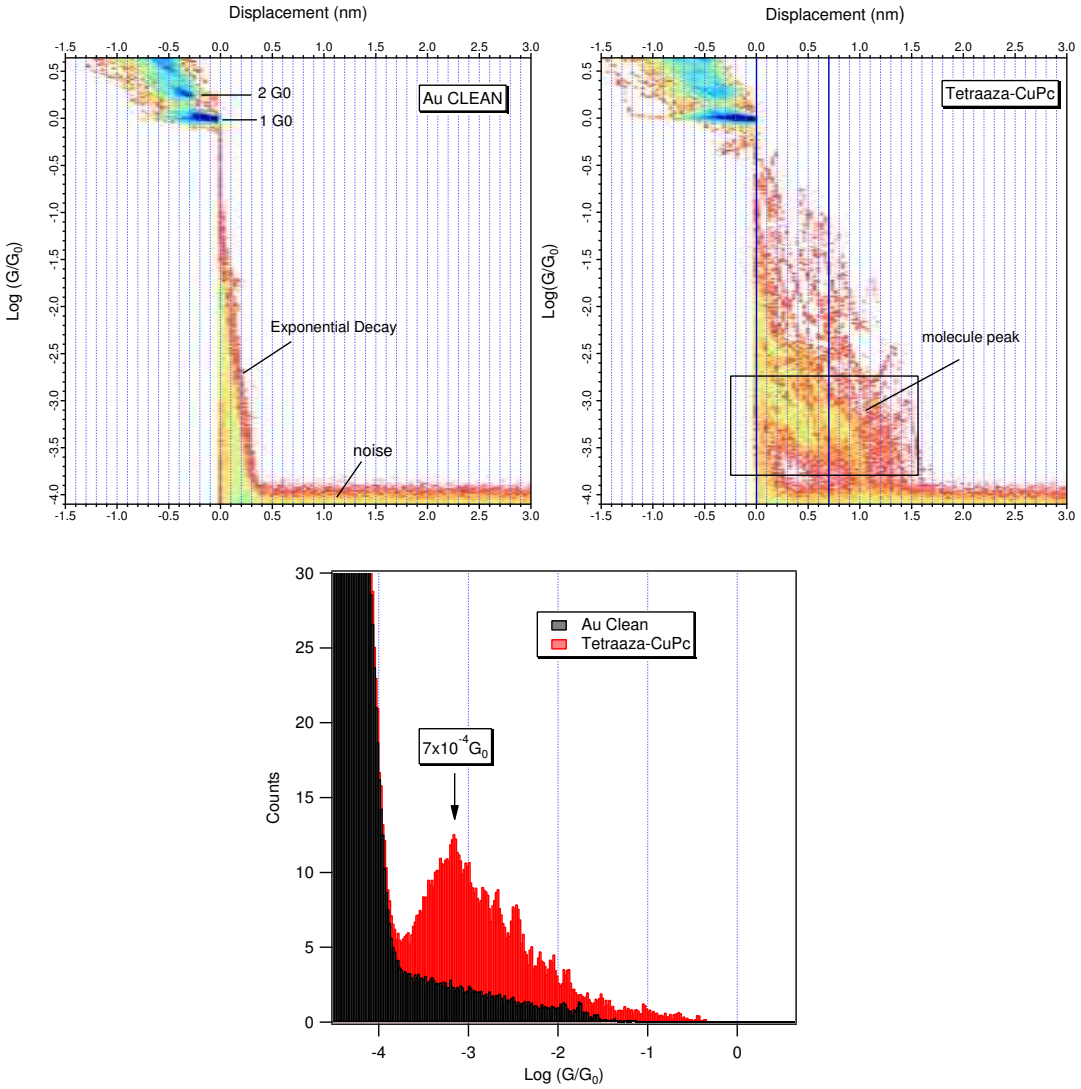

Figure 4.22: 2D conductance histograms which preserve displacement information constructed with 1000 traces (200 per point) collected on a clean gold sample (left top) and in presence of Tetraaza-CuPc (top right) at 55 K. (Bottom) 1D conductance histograms obtained from the corresponding 2D histograms by integrating between 0 and 3 nm.

This indicates the LUMO as the dominant conductance channel in the charge transfer throughout the molecular junction.

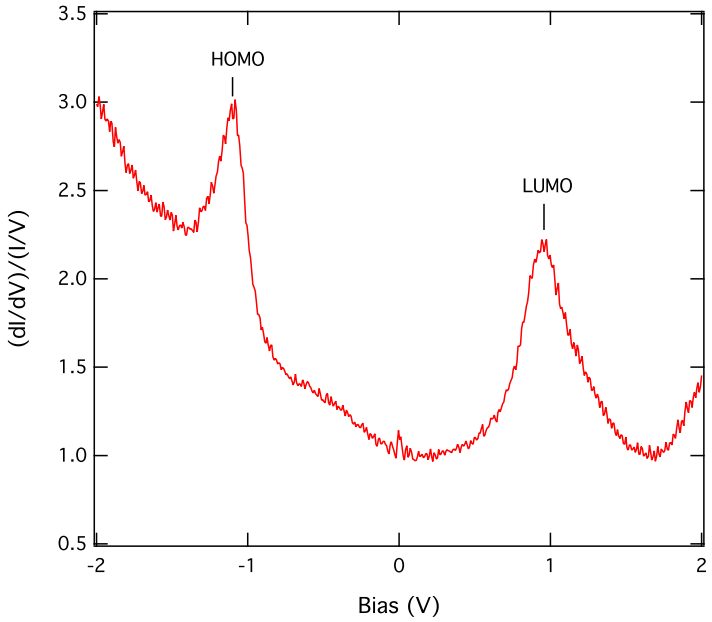

Figure 4.23: STS spectrum obtained by averaging over 100 dI/dV spectra taken on single moelcules belonging to molecular domains at 55 K. The curve gives an estimation of the HOMO-LUMO alignment of the Tetraaza-CuPc to the Au Fermi level.

It has been demonstrated that the low bias conductance through N-terminated molecules (di-amines or bipyridines) attached to gold electrodes can be described as a non resonant tunneling process or superexchange (115) (85). Two different models are frequently used to describe this process when the voltage applied across the junction is much smaller than the HOMO-LUMO gap of the bridging molecule. The molecule can be thought of as a tunnel barrier, and the transport details can be understood in terms of Simmons' model (9). Equivalently, conductance can be related to the electron transfer rate between a donor electrode and an acceptor electrode through a molecular bridge (a model introduced by McConnell(116)). As long as the metal Fermi level or, equivalently, the donor and acceptor levels are far enough from the molecular levels (HOMO and LUMO), the electron-tunneling rates decrease exponentially with increasing molecule length (L) with the measured low bias conductance G scaling as $e^{-\beta L}$. Here, the decay constant β depends on the tunneling barrier which amounts to

the energy separation between the metal Fermi level and the closest molecular level.

In order to evaluate the different weight of L and β in the conductance value obtained for the Tetraaza-CuPc, we try to compare it with the results obtained for different families of N-terminated moelcules (115). Fig. 4.24 shows the most probable conductance as a function of the N-N separation for a series of 1-N diamino alkanes (N=2-12), diamino polyphenyls (N=1-3) and diamino polyacenes (N=1-3). For comparison, the calculated tunnel probability is plotted for the same three families, but with polyacenes extended to N= 5. The right-hand scale is chosen so the theory and experiment coincide for 1,4 diaminobenzene.

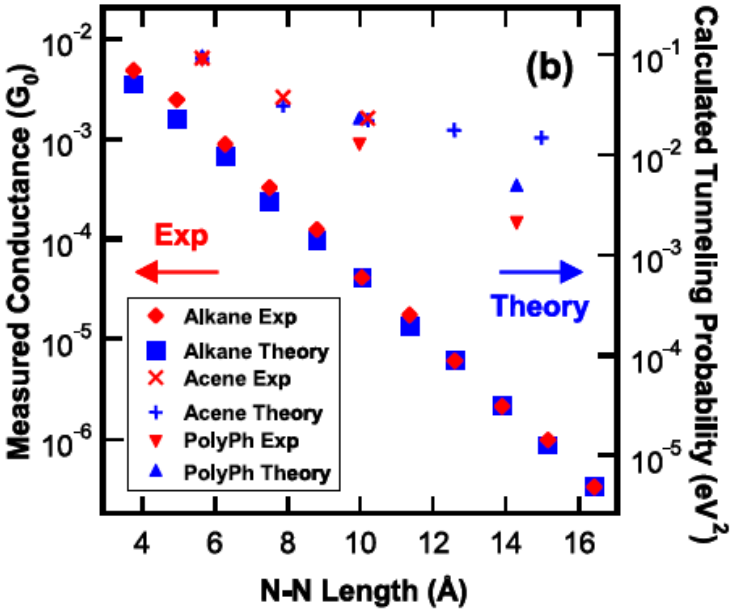

Figure 4.24: Most probable conductance for the alkane series plotted as a function of the N-N separation. Also shown are the same data for diamino polyphenyls (N = 1-3) and diamino polyacenes (N = 1-3). For comparison, the calculated tunnel probability is plotted for the same three families, but with polyacenes extended to N = 5. The right-hand scale is chosen so the theory and experiment coincide for 1,4 diaminobenzene (115).

For diaminoalkanes the conductance decreases exponentially with increasing length, with a decay constant 0.76±0.01Å^{-1}. Also the conductance of polyphenyls versus moelcule length fits an exponential form with a decay constant of 0.43±0.02 Å^{-1}. On the contrary, the conductance of diamino polyacenes shows a deviation from an exponential decay that can be due to a significant change in the HOMO-LUMO gap

with increasing length in the acenes (85). Comparing the magnitude of conductance for molecules with the same N-N length, we can see that 2,6 diaminoanthracene conductcs better than 4,4' diamino biphenyl which conducts better than 1,7 heptane diamine. This trend agrees with general expectations that conjugation along the backbone increases conductance. Also the conductance of bipyridines, not shown in this graph, can be explained by a non resonant tunneling. In particular the conductance of the 4, 4'-bipyridine is found to be 1.6×10^{-4} G_0 for a N-N distance of 7.2 Å. This value is much lower than the one measured for diamines with the same length. As mentioned before this is due to the different nature of the pyridine-gold bond with respect to that of the amine. If we try to place the conductance value of the Tetraaza-CuPc (7×10^{-4} G_0) vs the N-N distance (diagonal ∼20 Å or short side ∼14 Å) in this graph we found that it is in between that one of polyphenyls and polyacenes. This finding can be rationalized by considering both the conjugation extension in the macrocycle of Tetraaza-CuPc and the nature of the pyridine-gold. However not many studies have been performed on molecular junctions containing metal atoms (79, 80), therefore we are not able to say how the molecular conductance can be affected by the presence of the metal atom.

4.5.3 Conclusions

We have reliably and reproducibly measured the conductance of the Tetraaza-Cu-Phtahlocyanine by exploiting the pyridine-link chemistry which allows the molecule to bridge two gold electrodes. The molecule was deposited on the Au(100) surface and the molecular self-assembling properties was probed by STM. At RT the Tetraaza-CuPc is very mobile on this substrate and the few observed molecular patches are unstable. These patches are characterized by rows of few molecules adsorbed into the substrate troughs and slightly misaligned with the $[01\bar{1}]$ direction. At LT (55 K) the molecules are found frozen in small agglomerates or small islands but also in very large domains. In the presence of these stable domains we performed the break-junction measurements by using the developed experimental set-up. After breaking the last metal contact, the conductance traces show repeated jumps with a overall length of approximately 0.7 nm or 1 nm. These values are compatible with the molecule binding to the metal electrodes in two different configurations: one through pyridine nitrogen atoms belonging to the same side of the molecule (short side) and the other through opposite pyridine nitrogen atoms (long side or diagonal). The jumps occurring every 0.1-0.2 nm can be related to

a different coupling between the nitrogen-gold bond and the π system responsible of the conductance (LUMO). The histogram built from these traces returns a conductance value of 7×10^{-4} G_0, which is reasonable by considering the length and the conjugation degree of the macrocycle as well the nature of the pyridine-gold bond. However we are not able to say how the conductance is affected by the presence of the metal atom. In order to address this point we should perform systematic studies within a series of different metal-phthalocyanines (Metal=Mn, Fe, Co, Ni) as well as metal-free phtahlocyanines. At last we have also performed a spectroscopic study in order to address the electronic features of the systems. In particular we have found that in the monolayer phase the C 1s and N 1s XPS peaks are shifted towards lower BE with respect to the multilayer ones. The observed energy shift (0.5 eV) is most likely due to electrostatic effects rather than chemical interaction, confirming that molecules are weakly bounded to the surface.

5

Conclusions

In the present work two different issues of an organic-inorganic hybrid device have been addressed:

- the influence of the dieletric TiO_2(110) substrate on the self-assembly of several organic semiconductor molecules;
- the electron transport properties of a complex nitrogen-terminated molecule bridging two gold electrodes;

Both systems have been characterized from a structural and electronic point of view by making use of several complementary experimental techniques ranging from synchrotron to tunneling microscopy based methods. The structural order of the overlayers was mainly probed by Helium Atom Scattering (HAS) and Scanning Tunneling Microscopy (STM). The strength of the interaction with the substrate has been traced by spectroscopic techniques such as X-ray Absorption (XAS) and X-ray and Ultraviolet Photoemission Spectroscopy (XPS and UPS). Depending on the system under consideration two different methods have been used to characterize and understand the charge transfer properties: Resonant Photoemission Spectroscopy (RPES) for the organic/TiO_2(110) interface and STM-based break junction technique for the molecular junctions (STM-BJ). The main results can be summarized as follows:

Charge transfer at the interface: organic semiconductor molecules on the TiO_2(110)–1×1 surface.
Four different molecular species have been deposited on the TiO_2(110)-1×1 surface:

C60, pentacene, perylene-tetracarboxilic-aciid diimide (PTCDI) and perylene. Apart from the highly symmetric C60 molecule the choice of anisotropic planar molecules has been envisaged in order to improve the coherence of the growing films thanks to the better matching between the molecular size and the substrate lattice. Furthermore, as organic semiconductors, the molecules can be regarded as electron donors (pentacene and perylene) or electron acceptors (C60 and PTCDI). This aspect assumes particular relevance in relation to the possibility of changing the conduction properties of the TiO_2(110) surface by controlling the defects concentration.

C_{60} is found to interact very weakly with the TiO_2(110)-1×1 surface. Nevertheless the formation of stable molecular islands is observed. They are characterized by a p(5×2) reconstruction where C_{60} molecules are adsorbed on top the 5f-Ti rows. The organic layer floats at about 3.2 Å from the 5f-Ti rows keeping intact its molecular electronic structure. At last we found that the molecules in the islands spin around the surface normal, giving rise to correlated rotations where the total angular momentum of two neighboring molecules is conserved.

The interaction of pentacene with this dielectric substrate is also relatively weak. We have found that the substrate corrugation due to the oxygen rows drives the azimuthal orientation of the molecules which are aligned with their long axis parallel to the [001] substrate direction. The film growth proceeds via an interplay of two main interactions: the intermolecular side-by-side attraction that drives the formation of irregular stripes running along the $[1\bar{1}0]$ substrate direction and the intermolecular head-to-head repulsion that tends to maximize the stripe separation. The completion of the first layer leads to an incommensurate periodicity along the [001] substrate direction. In the other direction pentacene molecules preserve the substrate periodicity since they are slightly tilted along the molecular axis ($\sim 25°$). The structure of the monolayer phase mimics well that one of the pentacene *a-c* crystal planes, thus allowing the growth of a few additional lying-down layers.

The interaction of PTCDI with the TiO_2(110)-1×1 surface is found to be quite strong. As a result of this interaction a new electronic state is observed just in between the highest occupied molecular orbital (HOMO) and the Ti defect peak (the electronic state associated with oxygen vacancies). Both the molecular nature of this new state and the intensity decrease of the lower unoccupied molecular orbital (LUMO) indicate

that this new feature is derived from the partial filling of the LUMO level by the electrons of the substrate. The electrons involved in the charge transfer are those of the Ti defect state, as confirmed by its strong intensity decrease after molecule deposition. As in the pentacene case, the substrate corrugation drives the adsorption geometry of PTCDI moelcules which are aligned with their long axis parallel to the [001] substrate direction. Due to the strong interaction, the periodicity of the molecular layer along the [001] direction is commensurate with respect to the substrate($\times 5$). The molecule are also tilted along their molecular axis ($\sim 35°$) matching the substrate periodicity along the $[1\bar{1}0]$ direction.
The capability of PTCDI to act as an acceptor of electrons is due to the fact that its perylene core is electronically depleted by the electron-withdrawing action of the imide groups. This is confirmed by the results obtained on the perylene/TiO_2(110) system. After deposition, the VB region close to the Fermi level clearly show the HOMO and Ti defect state, without the appearance of a new electronic state. Moreover the intensity of the LUMO level is practically unperturbed as well the intensity of the Ti defect state. Also in this case the substrate corrugation is able to drive the azimuthal orientation of perylene which is aligned with its long axis parallel to the [001] substrate direction and slightly tilted in order to match the substrate periodicity.

All these findings demonstrate that the strong anisotropy of the TiO_2(110)-1×1 surface can be used as a template for the ordered growth of a molecular overlayer (in some cases even more than one). Moreover by controlling the electronic properties of the substrate it has been possible to observe a net charge transfer form the Ti defect state to the PTCDI molecule. This last point will be the object of future studies possibly exploring more extensively the charge transfer in the opposite direction, i.e. from the molecule to the substrate, as for example in the case of alkali metal adsorption.

Charge transport through single moelcule: Nitrogen-terminated molecules on gold.
The conductance of the Tetraaza-Cu-Phthalocyanine has been measured by means of of the STM-based break-junction method exploiting the versatile Nitrogen-link chemistry that makes the molecule able to act as a bridge between two gold electrodes. In particular by using the Tetraaza-Cu-Pthalocyanine we exploited the binding properties of the pyridine nitrogen. The molecule was deposited on the Au(100) surface and

the molecular self-assembly properties was probed by STM. At RT the Tetraaza-CuPc is very mobile on this substrate and the formation of molecular patches is rare and unstable. These patches are characterized by rows of few (5-6) molecules adsorbed into the substrate troughs and slightly misaligned with the $[01\bar{1}]$ substrate direction. At LT (55 K) the molecules are found frozen in small agglomerates or small islands but also in very large domains. In the presence of these stable domains we performed the break-junction measurements by using the developed experimental set-up. After breaking the last metal contact, the conductance traces show repeated jumps spread around 10^{-3} and 10^{-4} G_0. The overall length of these jumps is compatible with the molecule binding to the metal electrodes in two different configurations: one through pyridine nitrogen atoms belonging to the same side of the molecule (short side) and the other through opposite pyridine nitrogen atoms (long side or diagonal). The jumps occurring every 0.1-0.2 nm lead to a gradual lowering of the conductance value. This conductance behavior can be related to a different coupling between the nitrogen-gold bond and the π system responsible for the conductance during the stretching of the junction. The histogram built from these traces gives a conductance value of roughly 7×10^{-4} G_0. Considering the length and the conjugation degree of the macrocycle, this conductance value compares well with previous results obtained on systems like bipyridines. The system has been also characterized by a spectrocopic point of view. In particular we have found that in the monolayer phase the C 1s and N 1s XPS peaks are shifted towards lower BE with respect to the multilayer ones. The observed energy shift (0.5 eV) is most likely due to electrostatic effects rather than chemical interaction confirming that molecules are weakly bounded to the surface.

In conclusion we have reliably and repeatedly measured the conductance of the Tetraaza-CuPc. In the interpretation of these measurements the role of the functional groups has been highlighted. In order to understand how the conductance is affected by the central metal atom, further measurements on different metal-phthalocyanines and metal-free phtalocyanines are needed.

The list of related publications

V. Lanzilotto, C. Sanchez-Sanchez, G. Bavdek, D. Cvetko, M. F. Lopez, J. A. Martin-Gago, and L. Floreano *'Planar Growth of Pentacene on the Dielectric TiO_2(110) surface'*, J. Phys. Chem. C. 115 (2011) 4664

C. Sanchez-Sanchez, V. Lanzilotto, C. Gonzalez, A. Verdini, P. de Andrs, L. Floreano, Maria F. Lpez and J. A. Martn-Gago *'Floating molecular layer of spinning C60 molecules on TiO_2(110) surfaces'*, Chemistry-A European Journal, in press

C. Sanchez-Sanchez, V. Lanzilotto, G. Bidau, B. Gomez-Lor, R. Perez, L. Florenao, M. F. Lopez, J. A. Martin-Gago *'On-surface Dehydrogenation reactions of polycyclic aromatic hydrocarbons on TiO_2(110)'*, in preparation

References

[1] **IdTechEx study, www.idtechex.com**. 1

[2] J. R. Heath and M. A. Ratner. **Molecular Electronics**. *Physics Today*, **56**(5):43–49, 2003. 1

[3] H. Ishii, K. Sugiyama, and E. Ito. **Energy level alignment and interfacial electronic structures at organic/metal and organic/organic interfaces**. *Advanced materials*, **11**(8):605–625, 1999. 2

[4] N Karl. **Charge carrier transport in organic semiconductors**. *Synthetic Metals*, **133-134**:649–657, March 2003. 2

[5] G. Binnig and H. Rohrer. **Scanning tunneling microscopy**. *Surface Science*, **126**(1-3):236–244, March 1983. 4

[6] G. Binnig, H. Rohrer, C. Gerber, and E. Weibel. **Surface Studies by Scanning Tunneling Microscopy**. *Physical Review Letters*, **49**(1):57–61, July 1982. 4

[7] R. Wiesendanger and H.J. Güntherodt. *Scanning Tunneling Microscopy II*, **28** of *Springer Series in Surface Sciences*, chapter Magnetic F. Springer-Verlag Berlin Heidelberg, 1992. 4

[8] E. Müller. **Field Desorption**. *Physical Review*, **102**(3):618–624, May 1956. 5

[9] J.G. Simmons. **Generalized formula for the electric tunnel effect between similar electrodes separated by a thin insulating film**. *Journal of Applied Physics*, **34**(6):1793–1803, 1963. 5, 122

[10] J. Bardeen. **Tunnelling from a many-particle point of view**. *Physical Review Letters*, **6**(2):57–59, 1961. 5

[11] J. Tersoff and D.R. Hamann. **Theory of the scanning tunneling microscope**. *Physical Review B*, **31**(2):805–813, January 1985. 5

[12] D. Farias and K.H. Rieder. **Atomic beam diffraction from solid surfaces**. *Reports on Progress in Physics*, **61**:1575, 1998. 9

[13] T. Engel and K.H. Rieder. **Structural studies of surfaces with atomic and molecular beam diffraction**. In K. Heinz, K. Müller, T. Engel, and K.H. Rieder, editors, *Structural Studies of Surfaces*, **91** of *Springer Tracts in Modern Physics*, pages 55–180. Springer, 1982. 9

[14] N. Esbjerg and J.K. Nø rskov. **Dependence of the He-Scattering Potential at Surfaces on the Surface-Electron-Density Profile**. *Physical Review Letters*, **45**(10):807–810, September 1980. 9

[15] S. Hüfner. *Photoelectron Spectroscopy, Principles and Applications*. Springer, 2003. 13

[16] J. Stöhr. *NEXAFS spectroscopy*. Springer-Verlag, Berlin, 1992. 13, 68

[17] Paolo Vilmercati, Dean Cvetko, Albano Cossaro, and Alberto Morgante. **Heterostructured organic interfaces probed by resonant photoemission**. *Surface Science*, **603**(10-12):1542–1556, June 2009. 13

[18] D Woodruff. **Adsorbate structure determination using photoelectron diffraction: Methods and applications**. *Surface Science Reports*, **62**(1):1–38, January 2007. 13

[19] Dietrich Menzel. **Ultrafast charge transfer at surfaces accessed by core electron spectroscopies.** *Chemical Society reviews*, **37**(10):2212–23, October 2008. 16

[20] P A Bruhwiler, O Karis, and N Martensson. **Charge-transfer dynamics studied using resonant core spectroscopies**. *Review of Modern Physics*, **74**(3):703–740, 2002. 16

[21] E Busetto, A Lausi, and S. Bernstorff. **The high-energy monochromator for the ALOISA beamline at Elettra**. *Review of scientific instruments*, **66**(2):2078–2081, 1995. 23

[22] L Floreano, G. Naletto, D. Cvetko, R. Gotter, M. Malvezzi, L. Marassi, A. Morgante, A. Santaniello, A. Verdini, F. Tommasini, and Others. **Performance of the grating-crystal monochromator of the ALOISA beamline at the Elettra Synchrotron**. *Review of scientific instruments*, **70**(10):3855, 1999. 23, 63

[23] Brian O'Regan and Michael Grätzel. **A low-cost, high-efficiency solar cell based on dye-sensitized colloidal TiO2 films**. *Nature*, **353**(6346):737–740, October 1991. 34

[24] M K Nazeeruddin, A Kay, I. Rodicio, R. Humphry-Baker, E. Mueller, P Liska, N Vlachopoulos, and M. Graetzel. **Conversion of light to electricity by cis-X2bis(2,2'-bipyridyl-4,4'-dicarboxylate)ruthenium(II) charge-transfer sensitizers (X = Cl-, Br-, I-, CN-, and SCN-) on nanocrystalline titanium dioxide electrodes**. *Journal of the American Chemical Society*, **115**(14):6382–6390, July 1993. 34

[25] M Lahav, a B Kharitonov, and I Willner. **Imprinting of chiral molecular recognition sites in thin TiO2 films associated with field-effect transistors: novel functionalized devices for chiroselective and chirospecific analyses.** *Chemistry - A European Journal*, **7**(18):3992–7, September 2001. 34

[26] C Kleverlaan, M Alebbi, R Argazzi, C a Bignozzi, G M Hasselmann, and G J Meyer. **Molecular rectification by a bimetallic Ru-Os compound anchored to nanocrystalline TiO2.** *Inorganic chemistry*, **39**(7):1342–3, April 2000. 34

[27] Yongfeng Wang, Yingchun Ye, and Kai Wu. **Adsorption and assembly of copper phthalocyanine on cross-linked TiO2(110)-(1 x 2) and TiO2(210).** *The journal of physical chemistry. B*, **110**(36):17960–5, September 2006. 34

[28] Anna Rienzo, Louise C Mayor, Graziano Magnano, Christopher J Satterley, Evren Ataman, Joachim Schnadt, Karina Schulte, and James N O'Shea. **X-ray absorption and photoemission spectroscopy of zinc protoporphyrin adsorbed on rutile TiO2(110) prepared by in situ electrospray deposition.** *The Journal of chemical physics*, **132**(8):084703, February 2010. 34

[29] Jens Bæ k Simonsen, Bartosz Handke, Zheshen Li, and Preben Juul Mø ller. **A study of the interaction between perylene and the TiO2(110)-(11) surface-based on XPS, UPS and NEXAFS measurements**. *Surface Science*, **603**(9):1270–1275, May 2009. 34

[30] Britt-Elfriede Schuster, M Benedetta Casu, Indro Biswas, Alexander Hinderhofer, Alexander Gerlach, Frank Schreiber, and Thomas Chasse. **Role of the substrate in electronic structure, molecular orientation, and morphology of organic thin films: diindenoperylene on rutile TiO2(110)**. *Phys. Chem. Chem. Phys.*, **11**(40):9000–9004, 2009. 34

[31] P. Krüger, S. Bourgeois, B. Domenichini, H. Magnan, D. Chandesris, P. Le Fèvre, a. Flank, J. Jupille, L. Floreano, a. Cossaro, a. Verdini, and a. Morgante. **Defect States at the TiO2(110) Surface Probed by Resonant Photoelectron Diffraction**. *Physical Review Letters*, **100**(5):2–5, February 2008. 34, 43

[32] S. Reiss, H. Krumm, A. Niklewski, V. Staemmler, and Ch. Woll. **The adsorption of acenes on rutile TiO2(110): A multi-technique investigation**. *The Journal of Chemical Physics*, **116**(17):7704, 2002. 35

[33] J. Ivanco, T. Haber, J.R. Krenn, F.P. Netzer, R. Resel, and M.G. Ramsey. **Sexithiophene films on ordered and disordered TiO2(110) surfaces: Electronic, structural and morphological properties**. *Surface Science*, **601**(1):178–187, January 2007. 35

[34] R. Resel, M. Oehzelt, O. Lengyel, T. Haber, T.U. Schülli, a. Thierry, G. Hlawacek, C. Teichert, S. Berkebile, G. Koller, and M.G. Ramsey. **The epitaxial sexiphenyl (001) monolayer on TiO2(110): A grazing incidence X-ray diffraction study**. *Surface Science*, **600**(19):4645–4649, October 2006. 35

[35] S Munnix and M Schmeits. **Electronic densities of states of defect-free TiO2(110) and TiO2(001) surfaces**. *Physical Review B*, **28**(12):7342–7345, December 1983. 38

[36] S. Munnix and M. Schmeits. **Electronic structure of ideal TiO2(110), TiO2(001), and TiO2(100) surfaces**. *Physical Review B*, **30**(4):2202–2211, August 1984. 38

[37] K. Tsutsumi, O. Aita, and K. Ichikawa. **X-ray Ti K spectra and band structures of oxides of titanium**. *Physical Review B*, **15**(10):4638, 1977. 38

[38] U Diebold, Jf Anderson, Ko Ng, and D Vanderbilt. **Evidence for the Tunneling Site on Transition-Metal Oxides: TiO2(110).** *Physical review letters*, **77**(7):1322–1325, August 1996. 42

[39] Kwok-on Ng and David Vanderbilt. **Structure and apparent topography of TiO_{2}(110) surfaces**. *Physical Review B*, **56**(16):10544–10548, October 1997. 42

[40] R. Schaub, P. Thostrup, N. Lopez, E. Læ gsgaard, I. Stensgaard, J. Nø rskov, and F. Besenbacher. **Oxygen Vacancies as Active Sites for Water Dissociation on Rutile TiO2(110)**. *Physical Review Letters*, **87**(26):24–27, December 2001. 43

[41] T Kanbara, K Shibata, S Fujiki, Y Kubozono, S Kashino, T Urisu, M Sakai, A Fujiwara, R Kumashiro, and K Tanigaki. **N-channel field effect transistors with fullerene thin films and their application to a logic gate circuit**. *Chemical Physics Letters*, **379**(3-4):223–229, September 2003. 45

[42] D. Chirvase, Z. Chiguvare, M. Knipper, J. Parisi, V. Dyakonov, and J. C. Hummelen. **Temperature dependent characteristics of poly(3 hexylthiophene)-fullerene based heterojunction organic solar cells**. *Journal of Applied Physics*, **93**(6):3376, 2003. 45

[43] Tatiana Da Ros, Giampiero Spalluto, and Maurizio Prato. **Biological Applications of Fullerene Derivatives : A Brief Overview**. *Croatica Chemica Acta*, **74**(4):743–755, 2001. 45

[44] Aurelio Mateo-Alonso, Christian Ehli, G M Aminur Rahman, Dirk M Guldi, Giulia Fioravanti, Massimo Marcaccio, Francesco Paolucci, and Maurizio Prato. **Tuning Electron Transfer through Translational Motion in Molecular Shuttles**. *Angewandte Chemie International Edition*, **46**(19):3521–3525, 2007. 45

[45] T. Hashizume. **Intramolecular structures of C60 adsorbed on the Cu(111)11 surface studied by the field ion-scanning tunneling microscopy**. *Journal of Vacuum Science & Technology A: Vacuum, Surfaces, and Films*, **12**(4):2097, July 1994. 45

[46] E I Altman and R J Colton. **Nucleation, growth, and structure of fullerene films on Au (111)**. *Surface Science*, **279**(1-2):49–67, 1992. 45

[47] L J Terminello and D K Shuh. **Unfilled orbitals of C60 and C70 from carbon K-shell X-ray absorption**. *Chemical Physics Letters*, **182**(5):491–496, 1991. 46, 50

[48] Felix Loske, Ralf Bechstein, Jens Schütte, Frank Ostendorf, Michael Reichling, and Angelika Kühnle. **Growth of ordered C60 islands on TiO2(110).** *Nanotechnology*, **20**(6):065606, February 2009. 46

[49] J G Hou, Y Jinlong, W Haiqian, L Qunxiang, Z Changgan, Y Lanfeng, W Bing, D M Chen, and Z Qingshi. **Topology of two-dimensional C60 domains.** *Nature*, **409**(6818):304–5, January 2001. 50

[50] R Fasel, P Aebi, Rg Agostino, D Naumovic, J Osterwalder, a Santaniello, and L Schlapbach. **Orientation of adsorbed C60 molecules determined via x-ray photoelectron diffraction.** *Physical review letters*, **76**(25):4733–4736, June 1996. 51, 52

[51] Yufeng Chen and Michel A. Van Hove. **Private Communication**. 52

[52] Maria L Sushko, Andrey Yu Gal, and Alexander L Shluger. **Interaction of organic molecules with the TiO2 (110) surface: ab inito calculations and classical force fields.** *The journal of physical chemistry. B*, **110**(10):4853–62, March 2006. 56

[53] H Sun. **COMPASS: An ab Initio Force-Field Optimized for Condensed-Phase Applications-Overview with Details on Alkane and Benzene Compounds**. *The Journal of Physical Chemistry B*, **102**(38):7338–7364, September 1998. 56

[54] C.D. Dimitrakopoulos and P.R.L. Malenfant. **Organic Thin Film Transistors for Large Area Electronics**. *Advanced Materials*, **14**(2):99–117, January 2002. 57

[55] Masatoshi Kitamura and Yasuhiko Arakawa. **Pentacene-based organic field-effect transistors**. *Journal of Physics: Condensed Matter*, **20**(18):184011, May 2008. 57

[56] S. Yoo, B. Domercq, and B. Kippelen. **Efficient thin-film organic solar cells based on pentacene/C60 heterojunctions**. *Applied Physics Letters*, **85**(22):5427, 2004. 57

[57] Alex C. Mayer, Matthew T. Lloyd, David J. Herman, Todd G. Kasen, and George G. Malliaras. **Postfabrication annealing of pentacene-based photovoltaic cells**. *Applied Physics Letters*, **85**(25):6272, 2004. 57

[58] Christine C Mattheus, Anne B Dros, Jacob Baas, Auke Meetsma, Jan L. de Boer, and Thomas T. M. Palstra. **Polymorphism in pentacene**. *Acta Crystallographica Section C Crystal Structure Communications*, **57**(8):939–941, August 2001. 57, 68, 69

[59] Ricardo Ruiz, Devashish Choudhary, Bert Nickel, Tullio Toccoli, Kee-Chul Chang, Alex C. Mayer, Paulette Clancy, Jack M. Blakely, Randall L. Headrick, Salvatore Iannotta, and George G. Malliaras. **Pentacene Thin Film Growth**. *Chemistry of Materials*, **16**(23):4497–4508, November 2004. 57

[60] Gregor Bavdek, Albano Cossaro, Dean Cvetko, Cristina Africh, Cecilia Blasetti, Friedrich Esch, Alberto Morgante, and Luca Floreano. **Pentacene nanorails on Au(110).** *Langmuir : the ACS journal of surfaces and colloids*, **24**(3):767–72, February 2008. 57

[61] Luca Floreano, Albano Cossaro, Dean Cvetko, Gregor Bavdek, and Alberto Morgante. **Phase diagram of pentacene growth on Au(110).** *The journal of physical chemistry. B*, **110**(10):4908–13, March 2006. 58

[62] S Sohnchen, S Lukas, and G Witte. **Epitaxial growth of pentacene films on Cu(110)**. *The Journal of Chemical Physics*, **121**(1):525–534, 2004. 61

[63] Michele Alagia, Chiara Baldacchini, Maria Grazia Betti, Fabio Bussolotti, Vincenzo Carravetta, Ulf Ekström, Carlo Mariani, and Stefano Stranges. **Core-shell photoabsorption and photoelectron spectra of gas-phase pentacene: experiment and theory.** *The Journal of chemical physics*, **122**(12):124305, March 2005. 64, 65

[64] Mirco Chiodi, Luca Gavioli, Marco Beccari, Valeria Di Castro, Albano Cossaro, Luca Floreano, Alberto Morgante, Aloke Kanjilal, Carlo Mariani, and Maria Betti. **Interaction strength and molecular orientation of a single layer of pentacene in organic-metal interface and organic-organic heterostructure**. *Physical Review B*, **77**(11):1–7, March 2008. 68

[65] Zhang Jia, Vincent Lee, Ioannis Kymissis, Luca Floreano, Alberto Verdini, Albano Cossaro, and Alberto Morgante. **In situ study of pentacene interaction with archetypal hybrid contacts: Fluorinated versus alkane thiols on gold**. *Physical Review B*, **82**(12):1–6, September 2010. 68

[66] Ajay K. Pandey, Sylvie Dabos-Seignon, and Jean-Michel Nunzi. **Pentacene: PTCDI-C13H27 molecular blends efficiently harvest light for solar cell applications**. *Applied Physics Letters*, **89**(11):113506, 2006. 71

[67] J Kim. **Organic donor/acceptor heterojunction photovoltaic devices based on zinc phthalocyanine and a liquid crystalline perylene diimide**. *Chemical Physics Letters*, **383**(1-2):11–15, January 2004. 71

[68] S. Karak, V.S. Reddy, S.K. Ray, and A. Dhar. **Organic photovoltaic devices based on pentacene/N,N-dioctyl-3,4,9,10-perylenedicarboximide heterojunctions**. *Organic Electronics*, **10**(5):1006–1010, August 2009. 71

[69] J. Puigdollers, M. Della Pirriera, A. Marsal, A. Orpella, S. Cheylan, C. Voz, and R. Alcubilla. **N-type PTCDIC13H27 thin-film transistors deposited at different substrate temperature**. *Thin Solid Films*, **517**(23):6271–6274, October 2009. 71

[70] James N. OShea, Alex Saywell, Graziano Magnano, Luís M.A. Perdigão, Christopher J. Satterley, Peter H. Beton, and Vinod R. Dhanak. **Adsorption of PTCDI on Au(111): Photoemission and scanning tunnelling microscopy**. *Surface Science*, **603**(20):3094–3098, October 2009. 71

[71] J Taborski, P Vaterlein, H Dietz, U Zimmermann, and E Umbach. **NEXAFS investigations on ordered adsorbate layers of large aromatic molecules**. *Journal of electron spectroscopy and related phenomena*, **75**:129–147, 1995. 71, 82

[72] Y Zou, L Kilian, a Scholl, T Schmidt, R Fink, and E Umbach. **Chemical bonding of PTCDA on Ag surfaces and the formation of interface states**. *Surface Science*, **600**(6):1240–1251, March 2006. 73

[73] a Schöll, Y Zou, M Jung, Th Schmidt, R Fink, and E Umbach. **Line shapes and satellites in high-resolution x-ray photoelectron spectra of large pi-conjugated organic molecules.** *The Journal of chemical physics*, **121**(20):10260–7, November 2004. 75

[74] A Schoell, Y Zou, D Huebner, S G Urquhart, Th Schmidt, R Fink, and E Umbach. **A comparison of fine structures in high-resolution x-ray-absorption spectra of various condensed organic molecules.** *The Journal of chemical physics*, **123**(4):044509, July 2005. 82

[75] Mark a Iron, Revital Cohen, and Boris Rybtchinski. **On the unexpected stability of the dianion of perylene diimide in water. A computational study**. *The journal of physical chemistry. A*, **115**(10):2047–56, March 2011. 84, 85

[76] S. Wendt, R. Schaub, J. Matthiesen, E.K. Vestergaard, E. Wahlström, M.D. Rasmussen, P. Thostrup, L.M. Molina, E. Læ gsgaard, I. Stensgaard, B. Hammer, and F. Besenbacher. **Oxygen vacancies on TiO2(110) and their interaction with H2O and O2: A combined high-resolution STM and DFT study**. *Surface Science*, **598**(1-3):226–245, December 2005. 85

[77] Miguel Ruiz-Osés, Thorsten Kampen, Nora González-Lakunza, Iñaki Silanes, Philipp M Schmidt-Weber, André Gourdon, Andrés Arnau, Karsten Horn, and J Enrique Ortega. **Spectroscopic fingerprints of amine and imide functional groups in self-assembled monolayers.** *Chemphyschem: a European journal of chemical physics and physical chemistry*, **8**(11):1722–6, August 2007. 85

[78] M. a. Reed. **Conductance of a Molecular Junction**. *Science*, **278**(5336):252–254, October 1997. 94

[79] Jiwoong Park, A.N. Pasupathy, J.I. Goldsmith, C. Chang, Y. Yaish, J.R. Petta, M. Rinkoski, J.P. Sethna, H.D. Abruña, P.L. McEuen, and Others. **Coulomb blockade and the Kondo effect in single-atom transistors**. *Nature*, **417**(6890):722–725, 2002. 94, 124

[80] W. Liang, M.P. Shores, M. Bockrath, J.R. Long, and H. Park. **Kondo resonance in a single-molecule transistor**. *Nature*, **417**(6890):725–729, 2002. 94, 124

[81] Z. Ji-Ming, R. Zhao-Yu, G. Ping, T. Jin-Shou, and B. Jin-Tao. **Effects of Contact Geometry on Electron Transport of 1, 4-Diaminobenzene**. *Chinese Physics Letters*, **25**:1423, 2008. 94

[82] Young S Park, Adam C Whalley, Maria Kamenetska, Michael L Steigerwald, Mark S Hybertsen, Colin Nuckolls, and Latha Venkataraman. **Contact chemistry and single-molecule conductance: a comparison of phosphines, methyl sulfides, and amines.** *Journal of the American Chemical Society*, **129**(51):15768–9, December 2007. 94

[83] Frank Schreiber. **Structure and growth of self-assembling monolayers**. *Progress in Surface Science*, **65**(5-8):151–257, November 2000. 94

[84] Latha Venkataraman, Jennifer E Klare, Colin Nuckolls, Mark S Hybertsen, and Michael L Steigerwald. **Dependence of single-molecule junction conductance on molecular conformation.** *Nature*, **442**(7105):904–7, August 2006. 94, 95

[85] M Kamenetska, Su Ying Quek, a C Whalley, M L Steigerwald, H J Choi, Steven G Louie, C Nuckolls, M S Hybertsen, J B Neaton, and L Venkataraman. **Conductance and geometry of pyridine-linked single-molecule junctions.** *Journal of the American Chemical Society*, **132**(19):6817–21, May 2010. 94, 95, 122, 124

[86] Jochen Ulrich, Donna Esrail, William Pontius, Latha Venkataraman, David Millar, and Linda H Doerrer. **Variability of conductance in molecular junctions.** *The journal of physical chemistry. B*, **110**(6):2462–6, February 2006. 95

[87] Latha Venkataraman, Jennifer E Klare, Iris W Tam, Colin Nuckolls, Mark S Hybertsen, and Michael L Steigerwald. **Single-molecule circuits with well-defined molecular conductance.** *Nano letters*, **6**(3):458–62, March 2006. 95, 101, 118

[88] A Cossaro, R Mazzarello, R Rousseau, L Casalis, A Verdini, A Kohlmeyer, L Floreano, S Scandolo, A Morgante, M L Klein, and G Scoles. **X-ray diffraction and computation yield the structure of alkanethiols on gold(111).** *Science*, **321**(5891):943–6, August 2008. 95

[89] Michael G. Walter, Alexander B. Rudine, and Carl C. Wamser. **Porphyrins and phthalocyanines in solar photovoltaic cells**. *Journal of Porphyrins and Phthalocyanines*, **14**(09):759, 2010. 95

[90] Christian G Claessens, Uwe Hahn, and Tomás Torres. **Phthalocyanines: from outstanding electronic properties to emerging applications.** *Chemical record*, **8**(2):75–97, January 2008. 95

[91] B. Simic-Glavaski. **Phthalocyanines in molecular electronic devices**. In *Engineering in Medicine and Biology Society, 1989. Images of the Twenty-First Century., Proceedings of the Annual International Conference of the IEEE Engineering in*, pages 1325–1326. IEEE, 1989. 95

[92] Afaf El-Sayed, Duncan J. Mowbray, Juan M. García-Lastra, Celia Rogero, Elizabeth Goiri, Patrizia Borghetti, Ayse Turak, Bryan P. Doyle, Martina DellAngela, Luca Floreano, Yutaka Wakayama, Angel Rubio, J. Enrique Ortega, and Dimas G. de Oteyza. **Supramolecular Environment-Dependent Electronic Properties of MetalOrganic Interfaces.** *The Journal of Physical Chemistry C*, **116**(7):4780–4785, February 2012. 95

[93] Maria Grazia Betti, Pierluigi Gargiani, Riccardo Frisenda, Roberto Biagi, Albano Cossaro, Alberto Verdini, Luca Floreano, and Carlo Mariani. **Localized and Dispersive Electronic States at Ordered FePc and CoPc Chains on Au(110)**. *The Journal of Physical Chemistry C*, **114**(49):21638–21644, December 2010. 95

[94] Luca Floreano, Albano Cossaro, Roberto Gotter, Alberto Verdini, Gregor Bavdek, Fabrizio Evangelista, Alessandro Ruocco, Alberto Morgante, and Dean Cvetko. **Periodic Arrays of Cu-Phthalocyanine Chains on Au(110)**. *Journal of Physical Chemistry C*, **112**(29):10794–10802, July 2008. 95, 111

[95] R. Landauer. **Electrical resistance of disordered one-dimensional lattices**. *Philosophical Magazine*, **21**:863–867, 1970. 96, 97

[96] Supriyo Datta. *Electronic Transport in Mesoscopic Systems*. Cambridge University Press, 1997. 96

[97] Rolf Landauer. **Conductance from transmission: common sense points**. *Physica Scripta*, **1992**:110, 1992. 97

[98] J. M. van Ruitenbeek, A. Alvarez, I. Pineyro, C. Grahmann, P. Joyez, M. H. Devoret, D. Esteve, and C. Urbina. **Adjustable nanofabricated atomic size contacts**. *Review of Scientific Instruments*, **67**(1):108, 1996. 98

[99] C. J. Muller, J. M. van Ruitenbeek, and L. J. de Jongh. **Experimental observation of the transition from weak link to tunnel junction**. *Physica C*, **191**:485–504, 1992. 98

[100] J. I. Pascual, J. Mendez, J. Gomez-Herreo, A. M. Baro, and Garcia N. **Quantum Contact in Gold Nanostructures by Scanning Tunneling Microscopy**. *Physical Review Letters*, **71**(12):1852–1857, 1993. 98

[101] L. Olesen, E. Laegsgaard, I. Stensgaard, F. Besenbacher, J. Schio/tz, P. Stoltze, K.W. Jacobsen, and J. No/rskov. **Quantized conductance in an atom-sized point contact**. *Physical Review Letters*, **72**(14):2251–2254, April 1994. 98

[102] Hideaki Ohnishi, Yukihito Kondo, and Kunio Takayanagi. **Quantized conductance through individual rows of suspended gold atoms**. *Letters to Nature*, **395**:780–783, 1998. 99

[103] Christian Joachim, JK Gimzewski, RR Schlittler, and C. Chavy. **Electronic Transparence of a Single C60 Molecule**. *Physical review letters*, **74**(11):2102–2105, 1995. 99

[104] M Dorogi, J Gomez, R Osifchin, RP Andres, and R. Reifenberger. **Room-temperature Coulomb blockade from a self-assembled molecular nanostructure**. *Physical Review B*, **52**(12):9071, 1995. 99

[105] Magnus Paulsson, Zahid Ferdows, and Datta Supriyo. **Resistance of a Molecule**. In *Nanoscience, Engineering and Technology Handbook*. 2003. 101

[106] Ferdows Zahid, Magnus Paulsson, and Supriyo Datta. **Electrical Conduction through Molecules**. In *Advanced Semiconductor and Organic Nano-Techniques*. 2003. 101

[107] Latha Venkataraman, Young S Park, Adam C Whalley, Colin Nuckolls, Mark S Hybertsen, and Michael L Steigerwald. **Electronics and chemistry: varying single-molecule junction conductance using chemical substituents.** *Nano letters*, **7**(2):502–6, February 2007. 101

[108] M. Dell'Angela, G Kladnik, A Cossaro, A Verdini, M Kamenetska, I Tamblyn, S Y Quek, J B Neaton, D Cvetko, A Morgante, and L Venkataraman. **Relating energy level alignment and amine-linked single molecule junction conductance.** *Nano letters*, **10**(7):2470–4, July 2010. 103

[109] M Kamenetska, M. DellAngela, J.R. Widawsky, G Kladnik, A Verdini, A Cossaro, D Cvetko, A Morgante, and L Venkataraman. **Structure and Energy Level Alignment of Tetramethyl Benzenediamine on Au(111)**. *The Journal of Physical Chemistry C*, **115**(25):12625–12630, June 2011. 103, 111

[110] Svetlana V. Kudrevich and Johan E. van Lier. **Aza-analogs of phthalocyanine: syntheses and properties**. *Coordination Chemistry Reviews*, **156**:163–182, 1996. 107

[111] M A Van Hove, R J Koestner, P C Stair, J P Bibérian, L L Kesmodel, I Bartoš, and G A Somorjai. **The surface reconstructions of the (100) crystal faces of iridium, platinum and gold: I. Experimental observations and possible structural models**. *Surface Science*, **103**(1):189–217, February 1981. 107

[112] Paula Havu, Volker Blum, Ville Havu, Patrick Rinke, and Matthias Scheffler. **Large-scale surface reconstruction energetics of Pt(100) and Au(100) by all-electron density functional theory**. *Physical Review B*, **82**(16):161418, October 2010. 107, 109

[113] V Aristov, O Molodtsova, V Maslyuk, D Vyalikh, V Zhilin, Y Ossipyan, T Bredow, I Mertig, and M Knupfer. **Electronic structure of pristine CuPc: Experiment and calculations**. *Applied Surface Science*, **254**(1):20–25, October 2007. 111

[114] S.Y. Quek, Maria Kamenetska, M.L. Steigerwald, H.J. Choi, S.G. Louie, M.S. Hybertsen, JB Neaton, and Latha Venkataraman. **Mechanically controlled binary conductance switching of a single-molecule junction**. *Nature nanotechnology*, **4**(4):230–234, 2009. 118

[115] Mark S Hybertsen, Latha Venkataraman, Jennifer E Klare, Adam C Whalley, Michael L Steigerwald, and Colin Nuckolls. **Amine-linked single-molecule circuits: systematic trends across molecular families.** *Journal of physics. Condensed matter: an Institute of Physics journal*, **20**(37):374115, September 2008. 118, 122, 123

[116] Harden M. McConnell. **Intramolecular Charge Transfer in Aromatic Free Radicals**. *The Journal of Chemical Physics*, **35**(2):508, 1961. 122

Acknowledgements

I would like to thank all those who gave me the possibility to complete this thesis. I'm especially grateful to Dr. Luca Floreano for supporting me during all the experiments done on the ALOISA/HASPES beamline. I also want to thank the other colleagues from the ALOISA team, Dr. Albano Cossaro, Dr. Alberto Verdini and Prof. Dean Cvetko, for many useful scientific discussions. I would like to express my gratitude to Dr. José Angel Martín Gago and Dr. Carlos Sánchez Sánchez for hosting me in their labs and introducing me to the STM world. A special thanks to the Slovenian guys: Dr. Gregor Bavdek for helping me during the HASPES experiments and Gregor Kladnik for the great support in Igor programming. Many thanks to Dr. Emilia Annese for assisting me during the APE beamtimes and Dr. Damjan Krizmancic for helping me in Labview programming. I also want to thank my colleague and friend Giorgia Olivieri for her constant support in everything. Last but not least, I would like to express my gratitude to my supervisor Prof. Alberto Morgante for giving me the possibility to work in such a interesting and challenging scientific environment.